STRUCTURAL EVOLUTION IN SURFACTANT ASSEMBLIES AND THEIR APPLICATION IN NANOMATERIALS SYNTHESIS FOR BIOMEDICAL APPLICATION

By

PRASUNA KOSHY

BHABHA ATOMIC RESEARCH CENTRE

A thesis submitted to the

Board of Studies in Chemical Sciences

in partial fulfillment of requirements

for the degree of

DOCTOR OF PHILOSPHY

of

HOMI BHABHA NATIONAL INSTITUTE

September 2011

Homi Bhabha National Institute

Recommendations of the Viva Voce Board

As members of the Viva Voce board, we certify that we have read the dissertation prepared by **Ms. PRASUNA KOSHY** entitled **"Structural evolution in surfactant assemblies and their application in nanomaterials synthesis for biomedical application"** and recommend that it may be accepted as fulfilling the dissertation requirement for the Degree of Doctor of Philosophy.

Chairman – Prof. V. Venugopal   Date:

Guide – Dr. P. A. Hassan   Date:

Member 1 – Dr. S. Chattopadhyay   Date:

Member 2 – Dr. Grace Samuel   Date:

     Final approval and acceptance of this dissertation is contingent upon the candidate's submission of the final copies of the dissertation to HBNI.

     I hereby certify that I have read this dissertation prepared under my direction and recommend that it may be accepted as fulfilling the dissertation requirement.

Date: Dr. P. A. Hassan

Place:

STATEMENT BY AUTHOR

This dissertation has been submitted in partial fulfillment of requirements for an advanced degree at Homi Bhabha National Institute (HBNI) and is deposited in the Library to be made available to borrowers under rules of the HBNI.

Brief quotations from this dissertation are allowable without special permission, provided that accurate acknowledgement of source is made. Requests for permission for extended quotation from or reproduction of this manuscript in whole or in part may be granted by the Competent Authority of HBNI when in his or her judgement the proposed use of the material is in the interests of scholarship. In all other instances, however, permission must be obtained from the author.

Prasuna Koshy

DECLARATION

I, hereby declare that the investigation presented in the thesis has been carried out by me. The work is original and has not been submitted earlier as a whole or in part for a degree / diploma at this or any other Institution / University.

Prasuna Koshy

Dedicated to ……

……My Beloved Family

ACKNOWLEDGEMENTS

Finally, I convey my heartfelt gratitude to my parents, sister and brothers for their constant encouragement, love, support and blessings.

Prasuna Koshy

CONTENTS

Structural evolution in surfactant assemblies and their application in nanomaterials synthesis for biomedical application

Synopsis

Surfactants are class of compounds possessing groups of opposing solubility characteristics, i.e. one water soluble group (hydrophilic group) and other oil soluble group (hydrophobic group). In order that the hydrophobic parts avoid contact with water as much as possible and the hydrophilic part of the surfactant moieties are exposed to water, above a critical concentration known as the 'critical micelle concentration', these amphiphilic surfactant molecules associate themselves into various structures such as spherical micelles, vesicles, thread-like micelles, bilayers etc. Nature and the concentration of the surfactants control the formation of various structures that are mentioned above. These self organizing structures find extensive applications in industries dealing with detergency, pharmaceutical and pesticide formulations etc. [1].

Mixtures of cationic and anionic surfactants often display a rich variety of microstructures in aqueous solutions, governed by the molar ratio of the two components. Catanionic mixed surfactants exhibit synergistic interactions generated between oppositely charged surfactant pairs. This has stimulated extensive research interest among experimentalists as well as theoreticians [1-3]. Complex structures such as, elongated micelles, vesicles, liquid-crystalline phases, nanodisks, etc., can be formed by changing the composition of catanionic mixtures. The addition of anionic surfactant to cationic micelles facilitates the transition from spherical to rod-like or worm-like micelles. When the number density of the micelles is sufficiently large, entanglement of the rod-like or worm-like micelles occurs and this leads to viscoelastic nature to the fluid [1]. Such viscoelastic fluids

are important in a wide variety of applications such as fracturing fluids in oil fields, thickening of personal care products and drag reducing agents [1]. The main objective of the present thesis is

(1) To study the control of aggregate geometry by proper blending of cationic and anionic surfactant mixtures and to understand the role of steric and electrostatic contribution to the head group area of surfactants in the mixed surfactant micelles.

(2) Physiochemical characterization of the various types of aggregates and phases by techniques like light scattering, small angle neutron scattering, rheology etc.

(3) To study the application of surfactant mixtures in the preparation of nanoparticles for biodiagnostic purposes.

The thesis consists of seven chapters

General and basic aspects of surfactants are discussed in **chapter 1**. It contains brief introduction about surfactants, their classifications and various applications. An introduction to surfactant properties has been given in details. Kinetic and thermodynamic factors responsible for the CMC of surfactants have been derived and explained. An introduction has been given to various kinds of mixed surfactant systems and a brief introduction to surfactant assisted nanoparticle synthesis and its application in biodiagnostic purposes have also been explained.

Chapter 2 deals with the experimental methods and characterization techniques employed in the present study. Chemicals used for various experiments have been discussed. A brief description regarding various instrumental methods, such as dynamic light scattering (DLS), Small angle neutron scattering (SANS), Rheology, Cryo-transmission electron microscopy (Cryo-TEM), UV-visible spectroscopy, and amperometry that are used for the

characterization has been given. The results of the present investigation are given and described in chapters 3-6.

Chapter 3 is divided into two parts. First part describes the formation of mixed catanionic micelles originated from enhanced solubility of sodium laurate (SL) in cetyltrimethylammonium bromide micelles (CTAB)/tetradecyltrimetylammonium bromide (TTAB) through cooperative self-assembly. Natural sodium soaps such as sodium laurate have limited solubility in water due to the high Kraft point. Organic salts of the type tetralkylammonium bromides show an excellent ability to depress the Kraft points of sodium soaps such as sodium laurate, sodium myristate, sodium palmitate and sodium stearate due to the "salting in" effect of the electrolyte [4]. Hence addition of sodium laurate to cationic CTAB/TTAB micelles forms various structures, depending on the ratio of cationic to anionic surfactant. A detailed structural analysis using characterization techniques like dynamic light scattering (DLS), small angle neutron scattering (SANS) and rheology has been done on the mixed micellar fluids. A comparison of the data obtained for CTAB-SL mixed micelles and TTAB-SL mixed micelles using the above mentioned techniques, has been used to study the effect of asymmetry in the chain length of the surfactants on the axial and equatorial growth of the mixed micellar system. Second part of the chapter describes the effect of electrolyte NaCl on the growth behavior of the mixed micellar system. The structural transition has been studied using DLS, SANS, and rheology. Assuming that all the added sodium laurate participates in the formation of mixed micelles, using rod-like micellar structure, modelling has been done to calculate the steric contribution and the electrostatic contribution of the surfactant head groups to the total head group area of CTAB/TTAB in CTAB/TTAB-SL mixed micelles and compared the values with that reported by Nagarajan [5].

Chapter 4 deals with the microstructural evolution in mixtures of cationic surfactant CTAB and an unsaturated anionic surfactant sodium oleate (NaOL), discussed in two sections. First part describes the scaling behavior of the rheological parameters of the mixed micelles comprising CTAB and NaOL. The presence of a long hydrocarbon chain with an unsaturation makes NaOL conducive for the formation of complex catanionic aggregates without phase separation [6]. The chapter includes a detailed rheological investigation on the mixed micellar system of CTAB-NaOL at various molar ratios of the surfactants. Rheological investigations have been done at a fixed relative ratio of surfactants but varying the volume fraction of micelles. The data are analysed in terms of the theory of Cates which takes into account the effect of breaking and recombination of micelles on the reptation theory of polymer dynamics. The Cates theory appears to offer a promising framework for understanding the linear viscoelastic properties of entangled worm-like micellar solutions formed at different volume fractions of micelles. Analysis is also done to study the concentration dependence of the terminal relaxation time, zero shear viscosity and the entanglement length of the micelles. The detailed study has been done on the dependence of the scaling exponents on the structural transition in the micelles from linear to branched worm-like micelles. Second part of the chapter deals with the phase behavior of catanionic CTAB-NaOL mixed micellar system by varying relative ratio of the surfactants. A detailed structural study of the different phases such as positively charged vesicles (cationic rich), negatively charged vesicles (anionic rich) and the birefrigent phases in the CTAB-NaOL mixtures at varying ratio of the two surfactants has been done using DLS, SANS, zeta potential, microscopy etc.

Chapter 5 describes the study of the dilution induced structural transition in the mixed micellar system comprising cationic entity decyltrimethylammonium bromide (DTAB) and the hydrotrope sodium 3-hydroxynaphthalene 2-carboxylate (SHNC), in the cationic rich side of the surfactant mixture. Such studies find important applications in personal care products or drug delivery system. The characterization of the mixed system has been done using DLS, SANS, and Cryo-TEM. This unusual behavior of micellar structural transition has been explained in terms of desorption of DTAB surfactant from mixed micelles with dilution.

Chapter 6 describes the preparation of nanoparticles of polyaniline using mixed micelles of sodium dodecylsulphate (SDS) and anilinium hydrochloride (AHC) as the template. The preliminary study on the interaction of prepared polyaniline nanoparticles with a model protein BSA using UV-Visible spectroscopy has been done. The interaction of proteins like progesterone antibody and antigens with polyaniline has been done using interdigitated array (IDA) silver microelectrodes and pulsed amperometric measurements.

Chapter 7, the concluding chapter, brings about the important conclusions of this study which can be summarized as follows.

(1) Long chain alkyl trimethylammonium surfactants CTAB/TTAB show an excellent ability to depress the Kraft point of natural sodium soap of lauric acid i.e. sodium laurate that has limited solubility in water due to its high Kraft point of 38 ^{0}C. Structural transition from spherical to rod-like to worm-like micelles occurs with varying relative ratio of surfactants.

(2) With the help of different scattering techniques, the axial and equatorial growth of CTAB/TTAB micelles induced by the addition of SL has been studied. Both CTAB and TTAB micelles undergo elongation to form rod-like assemblies by the addition of

SL. The axial growth is more pronounced in CTAB micelles. However, TTAB micelles undergo equatorial swelling and elongation by the addition of SL. Difference in the growth behavior of TTAB and CTAB micelles can be attributed to the asymmetry in the chain lengths of cationic-anionic pairs.

(3) It is possible to estimate the effective interfacial area occupied by the cationic-anionic pair in a mixture of CTAB/TTAB and SL using the model derived in this thesis. The effective head group area per molecule of ion-pair is sensitive to the ion-pair fraction in the aggregate, reflecting enhanced steric repulsion between ion-pairs. On the other hand, the equilibrium area per molecule of unimer is sensitive to the electrolyte concentration. From the ionic strength dependence of the equilibrium area per monomer, the contributions from steric and electrostatic effects can be separated. The variation in the equilibrium area of surfactant molecule with electrolyte concentration is consistent with the model predicted by Nagarajan.

(4) Rheological studies have indicated that the scaling exponents for branched micelles of the catanionic surfactant system of CTAB-NaOL agrees well with the values predicted by theoretical models, while for linear micelles an increase in the exponent is observed. Also slope of the plot of entanglement length vs volume fraction of the micelles show an abrupt change in the linear to branched micelle regime. This rheological behavior of the mixed micelles is analogous to the polymer melts, as previous studies report that a comparison of the rheological behavior of linear and branched polymers suggests that the hyperbranched polymers show a lower plateau modulus as compared to linear polymers.

(5) Birefringent phase, positively charged vesicles and negatively charged vesicles can be formed by properly blending oppositely charged surfactants. This offers a novel method of obtaining various aggregate geometries of controlled surface charge and structure rather than synthesizing one unique surfactant with desired properties.

(6) The structural characterization studies in the mixed micellar system comprising DTAB and SHNC indicates a change in the structure of the mixed micelles from spherical to rod-like micelles with dilution. This unusual behavior of micellar structural transition has been explained in terms of desorption of DTAB surfactant from mixed micelles with dilution.

(7) Polyaniline nanoparticles can be prepared using mixed micellar system of SDS and AHC as the template for chemical polymerization. Interaction of polyaniline with proteins like BSA and progesterone antibody has been done using spectroscopy and electrochemical techniques.

REFERENCES

1. S. Ezrahi, E. Tuval, A. Aserin, *Advances in colloid and interface science*, 2006, **77**, 128.
2. R. Zana, E. W. Kaler, *Giant micelles: Properties and applications*; 140, CRC press: New York, 2007**.**
3. D. Carriere, L. Belloni, B. Deme, M. Dubois, C. Vautrin, A. Meister and T. Zemb, *Soft Matter*, 2009, **5**, 4983.
4. B. Lin, A. V. McCormick, H. T. Davis, R. Strey, *Journal of colloid and Interface Sci.* 2005, **291**, 543.
5. R. Nagarajan, *Langmuir,* 2002, **18**, 31.
6. N. El-Kadi, F. Martins, D. Clausse, P. C. Schulz, *Colloid Polym. Sci.*, 2003, **281**, 353.

LIST OF FIGURES

LIST OF TABLES

CHAPTER 1

Introduction

Chapter 1: Introduction

1.1 Surfactants

Surfactants are class of compounds that have a special property to locate at interfaces or to form colloidal aggregates in solution at appropriate concentrations. Surfactants possess two groups of opposing solubility tendencies, (i) lyophobic group, also known as 'tail group'- one having little attraction for solvent and (ii) lyophilic group, also known as 'head group'- one having a strong attraction for the solvent [1]. When water is acting as the solvent, the groups are known as the hydrophobic and the hydrophilic groups, as 'hydro' stands for water. The hydrophilic group consists of a single ionic or multiple ionic groups which has strong affinity for water due to the ion-dipole and the dipole-dipole interactions. The hydrophobic group consists of a hydrocarbon, fluorocarbon or siloxane chain of sufficient length to produce the desired solubility characteristics when bound to a suitable hydrophilic group. Due to the presence of the groups having affinity for both, polar as well as nonpolar compounds, in these molecules, they are often referred to as amphiphilic molecules [1-6]. General chemical classification of surfactants is based on the nature of the hydrophilic group, with subgroup being defined by the nature of the hydrophobic group [7]. The groups are as follows

(i) Anionic surfactant: Anionic surfactants carry a negative charge on the hydrophilic head group and this includes the traditional long chain carboxylate soaps and the early synthetic detergents, the sulphonates, and the sulphates, e.g. sodium laurate.

(ii) Cationic surfactant: Cationic surfactants carry a positive charge on their hydrophilic head group and they are usually quaternary ammonium, imidazonium or alkylpyridinium compounds, e.g. cetyltrimethylammonium bromide.

(iii) Non-ionic surfactant: Non-ionic surfactants do not carry any charge on their head group and the water solubility is derived from the highly polar groups like polyethylene oxide

groups. This class of surfactants includes compounds such as amine oxides, sulphoxides, phosphine oxides, pyrrolidones, alkanolamides, etc., e.g. Triton X-100.

(iv) Zwitterionic surfactant: Zwitterionic surfactants also known as amphoteric surfactants possess both cationic as well as anionic groups in their hydrophilic moiety and hence can act either as a cationic surfactant or an anionic surfactant depending on the pH of the solution. This class of surfactants includes betaines, sulphobetaines, naturally occurring surfactants of the class lecithin and phosphatidyl cholines, etc. E.g. 3-dimethyl dodecyl amine propane sulphonate.

1.2 Surfactant aggregation

Above a narrow range of concentration, amphiphilic molecules often tend to aggregate in water or in selective solvents to form micelles and this concentration above which appreciable amounts of micelles are formed is termed as 'critical micelle concentration' (CMC). Some of the physico-chemical properties of aqueous surfactant solutions change dramatically above CMC. Some of the important physical properties which have been found to exhibit this behavior are the interfacial tension, osmotic pressure, equivalent conductivity, turbidity, diffusion coefficient, viscosity, and solubilization. Variation in a wide range of physico-chemical quantities of aqueous surfactant solutions around the critical micelle concentration are depicted in Figure 1.1. It can be observed that over a narrow range of concentration the physical properties of the solutions suffer a discontinuity in their variation with concentration. This sudden change in the measured property is interpreted as indicating a significant change in the nature of the solute species affecting the measured quantity [4, 5].
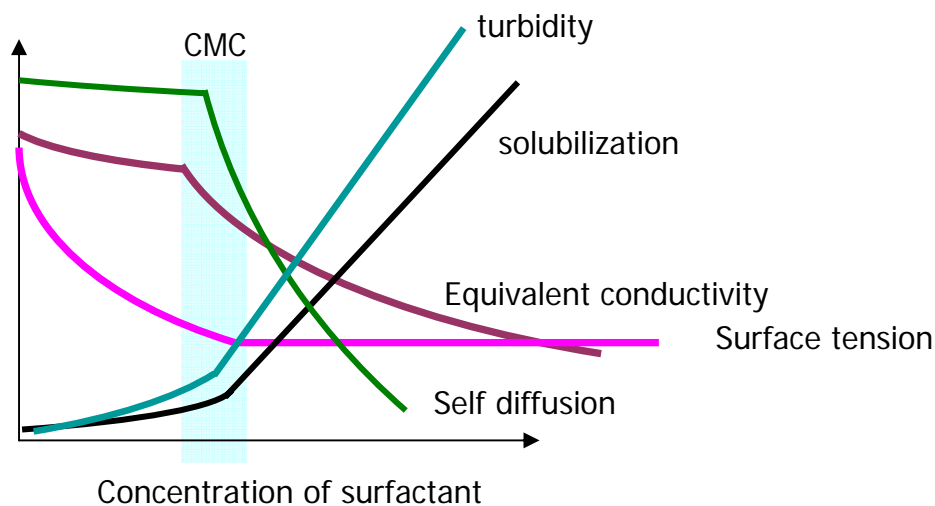
Figure 1.1 Variation of some of the physico-chemical properties of a solution with concentration of surfactant.

This sudden change corresponds to the formation of micellar aggregates and hence is used to determine the CMC of surfactant solutions. Also, the magnitude of the CMC obtained depends on the property being measured. In principle any of the physical properties illustrated in Figure 1.1 could be used to determine the CMC by plotting the physical property as a function of concentration and extrapolating the results at high and low concentration to an intersection point.

1.3 Surface activity and the '*hydrophobic effect*'

In an aqueous solution of surfactant, an individual amphiphilic molecule gets an opportunity to pass in to the air-water interface during its random diffusion process or the Brownian motion. Since the polar head group has a strong affinity for water molecules and its hydrobhobic tail group favors to avoid water, hence the preferred configuration is that in

which the surfactant molecules sits at the interface with its hydrophobic tail protruding out of the water surface. If such a configuration has lower energy than that of a free molecule in the bulk of the solution, the Maxwell-Boltzmann distribution law would predict a higher concentration of surfactant molecules at the interface. This is the origin of the surface activity in surfactant solutions.

The unifying principle that lies at the heart of aggregation phenomenon or the micelle formation is the so called *hydrophobic effect*. It is well known that the standard free energy of transfer of a single hydrocarbon molecule from aqueous phase into an oil is large and negative, reflecting the fact that the non-polar oils have poor solubility in water. A similar behavior would be expected for the hydrophobic tails of surfactant molecules. The thermodynamics of micelle formation shows that the enthalpy of micellization in aqueous solution is mostly positive, i.e. they are endothermic. But as the micelles do form above the CMC indicates that their free energy of formation ΔG must be negative. Since $\Delta G = \Delta H - T\Delta S$ and the enthalpy of formation ΔH is positive indicates that the entropy change ΔS should be positive. The positive entropy change associated with micellization even though the surfactant molecules are coming closer and forming clusters indicates a contribution to the entropy from the solvent molecules. It has been explained as below the CMC value, the entropy of the system is comparatively less since water molecules form a clathrate cage around free surfactant molecules but once the surfactant molecules have been herded into small clusters, individual molecules no longer have to be held in solvent cages and hence they are less constrained. This phenomenon is often referred to as the *hydrophobic effect* or the *hydrophobic interactions* in surfactant chemistry and is an example of an *entropy-driven* interaction.

Chapter 1: Introduction

1.4 Thermodynamics of micelle formation

A knowledge of the changes in thermodynamic quantities upon micellization is important not only for understanding the forces at play during micellization but also for predicting the behavior of micellar solutions upon changes in thermodynamic parameters like temperature, pressure, concentration, etc. Several models exist in the literature for describing the micellization phenomenon but the most useful model for the description of micelle formation is the mass action model [6]. In this model the micelles are treated as dynamic species which are in equilibrium with its monomers. In the case of an ionic surfactant, the molecules are considered to undergo complete dissociation as a 1:1 electrolyte whereas dissociation in micelles is not complete. Hence for a cationic surfactant AB, with A^+ as the hydrophobic part and B^- as the counter-ion, the micelle formation is assumed to take place via a single step reaction represented as

$$nA^+ + (n-m)B^- \leftrightarrow \left[A_nB_{(n-m)}\right]^{m+} \tag{1.1}$$
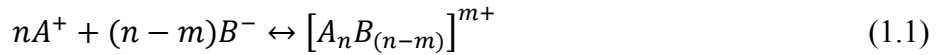
where n is the aggregation number and $\alpha = m/n$ is the ionization degree of the micelle. Applying the law of mass action, we get the equilibrium constant, K, for the above equilibrium as

$$K = [(A_nB_{n-m})^{m+}]/[A]^n[B]^{n-m} \tag{1.2}$$

The standard free energy of micellization per monomer (ΔG_m) is given as

$$\Delta G_m = -RTlnK/n \tag{1.3}$$

$$= RT\left\{\ln[A] + \left(1 - \frac{m}{n}\right)lm[B] - \ln[A_nB_{n-m}]/_n\right\} \tag{1.4}$$

where R is the gas constant and T is the temperature.

At CMC, $[A] \approx [B]$ It is found in practice that for surfactants with alkyl chain of C_8 or longer, n becomes sufficiently large that the third term in the equation can be neglected. Hence equation 1.4 approximates to

$$\Delta G_m \sim RT \left(2 - \frac{m}{n}\right) lnCMC \tag{1.5}$$

In the case of non-ionic micelles the mass law treatment has been applied more successfully and the equation 1.5 is simplified to

$$\Delta G_m \sim RTlnCMC \tag{1.6}$$

The enthalpy change accompanying micellization can be calculated using Gibbs-Helmholtz equation which is given as

$$\left(\frac{\partial \Delta G_T}{\partial T}\right)_p = -\frac{\Delta H}{T^2} \tag{1.7}$$

Combining equations 1.6 and 1.7, the enthalpy of micellization can be obtained as

$$\Delta H_m = -RT^2 \left(\frac{\partial lnCMC}{\partial T}\right)_P \tag{1.8}$$

In general, but not always, micelle formation is found to be an exothermic process, favored by a decrease in temperature, giving a positive value of enthalpy of micellization. The process, however, always has a substantial positive entropic contribution to overcome any positive enthalpy term, concluding that the micelle formation is primarily an entropy-driven process.

1.5 Dynamics of micelle formation

Micelles are known to be dynamic species in which the monomer rapidly joins and leaves the micelle in the bulk solution. Different methods are used to study the kinetics of such dynamic processes and they usually involve relaxation techniques. Most commonly used techniques are stopped-flow, pressure jump, temperature jump, ultrasonic relaxation, nuclear magnetic resonance (NMR), electron paramagnetic resonance (EPR), etc. All these studies

have revealed that there exists two major relaxation processes in micellar kinetics, one occurring in the fast microsecond range and the other in the slower millisecond range. It is now well established that the faster relaxation process which is in the microsecond time scale is due to the release of a single surfactant molecule from the micelle and its subsequent incorporation into the micelle and the slow relaxation process occurring in the millisecond range represents the total dissolution of the micelle into its monomers and its subsequent reassociation.

1.6 Interactions in micellar solution

Micellar solutions are thermodynamically stable colloidal dispersions. The main types of interactions acting between the micelles are:

(i)   An effective hard-core repulsion

(ii)   van der Waals attraction

(iii)   An electric double-layer repulsion

(iv)   Repulsive solvation forces

1.6.1 Hard-core repulsion

It is a strong repulsive force determining how close two micelles can ultimately approach each other. The hard-core repulsion (U_{hs}) is infinite for $r < \sigma$ and is effectively zero for $r > \sigma$, where σ is the hard core diameter of the micelles.

1.6.2 van der Waals interaction

The attractive van der Waals interaction potential (U_{vw}) between two identical micelles of diameter σ at the centre-to-centre distance r is given by:

$$U_{vw} = -\frac{A}{12}\left[\frac{1}{x^2-1} + \frac{1}{x^2} + \frac{2\ln(x^2-1)}{x^2}\right] \qquad (1.9)$$

7

Where x=r/σ and A is the Hamaker constant [8]. The effective range of van der Waals interaction is about 3σ, beyond which they are too weak to be of any significance.

1.6.3 Repulsive electrostatic double-layer interaction

In the case of ionic surfactants, the micellar surface is charged. Hence the counterions condense on the micellar surface in the form of an electrical double layer of opposite charge, depending on the ionic strength of the medium. Such an interaction is known as the electrostatic double-layer interaction [9], and between two spherical micelles it is given by

$$U_{dl} = \frac{\pi\epsilon_0\epsilon\sigma^2\psi_0^2 exp[-\kappa(r-\sigma)]}{r} \qquad r>\sigma \qquad (1.10)$$

where r is interionic centre-to-centre distance, ϵ is the dielectric constant of the solvent medium, ϵ_0 is the permittivity of the free space, ψ_0 is the surface potential which is related to the electronic charge Z_m on the particle by

$$\psi_0 = \frac{Z_m}{\pi\epsilon_0\epsilon\sigma(2+\kappa\sigma)} \qquad (1.11)$$

κ is the inverse Debye screening length, given by

$$\kappa = \left[\frac{8\pi N_A e^2 I}{10^3\epsilon k_B T}\right]^{1/2} \qquad (1.12)$$

defined by the ionic strength of the solution, I

$$I = \frac{1}{2}\sum z_i^2 M_i \qquad (1.13)$$

where M_i is the molar concentration of i-type ions in the solution medium and z_i is the valency of the ions.

The double-layer interaction depends on the electrolyte concentration, the pH value of the solution and the surface charge density. When the electrolyte concentration is increased, the

repulsive forces are effectively screened out and the interaction is mainly dominated by van der Waals attraction.

1.6.4 Repulsive solvation forces

When water molecules strongly bind to a hydrated or a hydrophilic surface group (e.g. $-PO_4^-$, -OH, etc.), there will be an additional short range repulsion arising from the energy needed to dehydrate these groups as two surfaces approach each other. Such repulsive forces are known as solvation or hydration forces. The range of these solvation forces is generally about 20 – 30 Å. They rise steeply and exponentially with a decay length of 2-3 Å, dominating the interaction at small surface separations. These forces play an important role for preventing the coalescence of the neutral non-ionic micelles [10].

1.7 Phase behavior of surfactants

The phase behavior of surfactant solutions can be well described by temperature-composition relationship as shown in Figure 1.2 [11]. This phase diagram has been chosen because it covers most of the major lyotropic mesophases commonly encountered in surfactant-water systems. The phase behavior of surfactants and its variation with temperature depends largely on the nature of the hydrophilic group of surfactant molecules. In case of ionic surfactants, initially the solubility increases slowly with increase in temperature until a value is reached at which the solubility increases rapidly and the material becomes very highly soluble. This temperature is often referred as the Kraft temperature or simply the Kraft point. If both solubility and the CMC are plotted as a function of temperature, one finds an intersection between the solubility and the CMC curves at the Kraft point or Kraft temperature. Thus the Kraft point is the temperature at which the value of the solubility and

the CMC becomes equal. One can think that at the Kraft point, micelles, monomers, and solid surfactant are in equilibrium with each other.
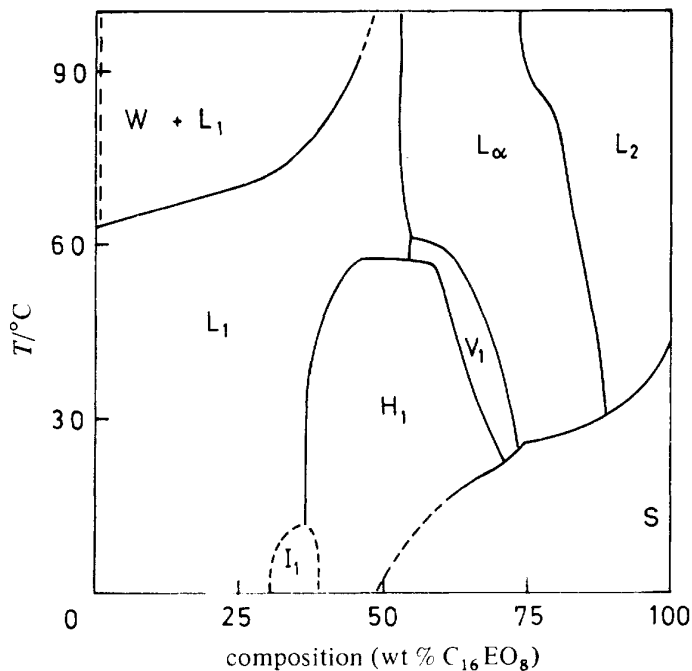
Figure 1.2 Phase behavior of alkyl poly (ethylene) nonionic surfactant $C_{16}E_8$-H_2O system (From Ref 11).

Non-ionic surfactants, unlike ionic surfactants, are very sensitive to temperature variations. If a dilute solution of non-ionic surfactant is heated above a certain temperature strong light scattering is observed and the solution becomes cloudy. The temperature at which cloudiness occurs is designated as the cloud point of the surfactant solution at that concentration. The cloud point of a surfactant solution also depends on its concentration.

Below the cloud point curve many different phases may be distinguished depending on the surfactant concentration. In dilute solutions, when concentration is not too far from the CMC, the micelles remain more or less spherical in shape and the solution is isotropic (Figure

1.3a). As the surfactant concentration is increased, the micelles are forced to come closer thereby increasing the extent of intermicellar interaction. The formation of a series of regular geometries, as volume fraction is increased, is a way in which the surfaces can be allowed to maximize their separation and hence decrease the intermicellar interactions. Initially as the surfactant concentration increases, there is a transition from more or less spherical to cylindrical or rod-like micelles. At surfactant concentration of perhaps 20-30% by weight, a new phase appears which is birefringent and is quite viscous. XRD experiments demonstrate that this phase consists of long parallel rod-like micelles arranged in a hexagonal array. The interior of micelles is apparently fluid resembling a liquid hydrocarbon in many respects as they are non-polar in nature. This phase is a liquid crystalline phase called the normal hexagonal phase (Figure 1.3b). The degree of ordering of the molecules is intermediate between that of a liquid and of a crystalline solid and the flow properties are intermediate between that of a viscous liquid and of a crystalline elastic solid. Therefore this phase is also known as the middle phase.

At even higher concentration of surfactants, the arrangement of surfactant molecules into bilayers becomes favorable and another liquid crystalline phase known as lamellar (L_α) phase appears. This phase is built up from flexible bilayer sheets of indefinite area, arranged parallel to each other. Low angle X-ray diffraction (XRD) data shows spacing corresponding to a repeat unit which is the back to back bilayer of surfactant molecules with the alkyl groups in contact with each other as shown in Figure 1.3c. Lamellar phases are less viscous than hexagonal phase though they contain less amount of water. This is because of the ease with which the parallel layers can slide over each other when shear is applied.

Chapter 1: Introduction

The next most abundant mesomorphic phases after hexagonal and lamellar are cubic phases. They occur in many different parts of the phase diagram and it is most likely that they have different structures. Cubic phases (denoted by I_1) observed between hexagonal (H_1) and isotropic liquid (L_1) phase are optically isotropic. Early proposal for their structure was that they consisted of closed spherical aggregates array, originally thought to be forming face centered cube but more likely body centered cube. More recent suggestion is that the building blocks are not spherical aggregates but are short rods or ellipsoids [12]. Between H_1 and L_α phases, cubic phases denoted by V_1 are seen. It has been proposed that they can be formed from bilayer elements arranged in an open bicontinuous network. As a result such aggregates are called bicontinuous or sponge phases.

Another important category of supramolecular aggregates which are often encountered in phospholipids are the mesophases of closed bilayers capable of entrapping ions in their aqueous interiors. They are known as vesicles or liposomes (Figure 1.3d) and have attained considerable attention as membrane models. In the recent few years there have been reports of spontaneous vesicle formation in certain aqueous mixtures of commercially available single tailed surfactants with oppositely charged head groups [13]. This way of vesicle preparation offered a remarkably simple way of tailoring vesicle properties and their surface charges, allowing efficient encapsulation to take place without mechanical or chemical perturbation of the final vesicle composition or structure. Figure 1.3 depicts, pictorially, some of the major structures often encountered in surfactant-water system that are discussed above.
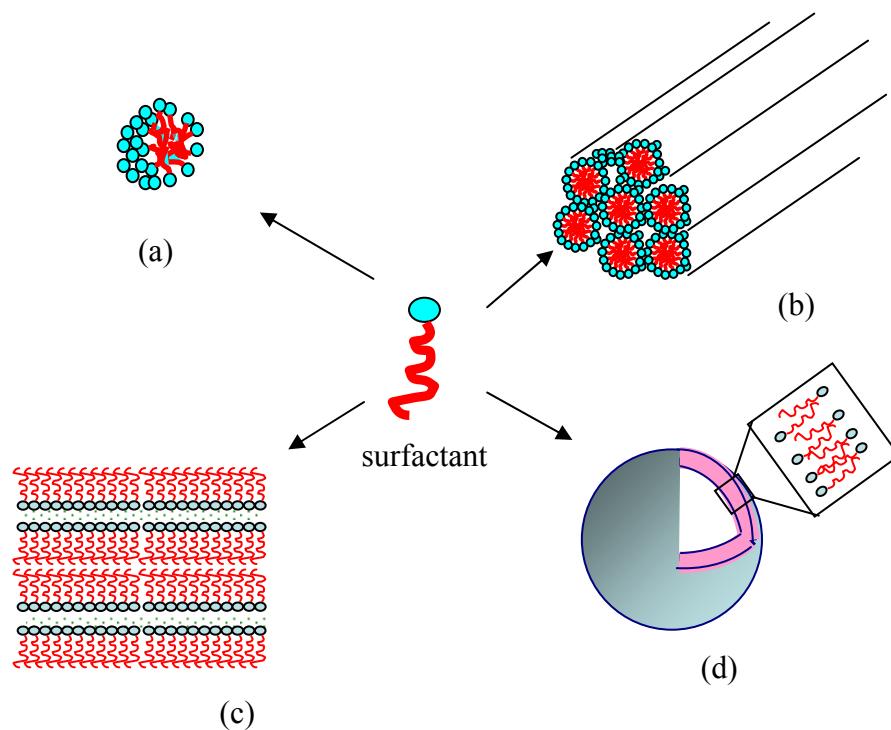
Figure 1.3 Schematic representation of some of the microstructures of surfactant-water phases. spherical micelle (a), normal hexagonal (b), lamellar or bilayer (c), and vesicle (d).

1.8 Packing parameter and bending rigidity

As mentioned in the previous section, there are different types of aggregate structures possible in a system of surfactant-water. It is found that these aggregate geometries depend broadly on various factors like nature of the surfactant molecule, surfactant concentration, nature of the counter-ion, ionic strength of the solution, etc. The question of what will be the preferred geometry of the aggregates formed in a surfactant-water system was a subject of major interest during the last few decades. As a result some models have emerged that are helpful in organizing the results and predicting the structure of supramolecular assemblies that are formed in surfactant solutions. The first satisfactory explanation comes from the geometric packing models suggested by Tanford and Israelachvili and co-workers [14, 15].

Chapter 1: Introduction

The aggregation of amphiphiles into various structures such as micelles, bilayers, vesicles, etc. arise mainly from an interplay of two opposing forces, one the so called 'hydrophobic effect' of the hydrocarbon tail which tends to bring the molecules close together and the other is the 'solvation' of the head groups which tends to keep the hydrophilic part away from each other, as already discussed in the previous section. In the case of ionic surfactants, there is an additional contribution from the electrostatic repulsion of the head groups, further increasing the effective head group area per molecule. The essence of the theory of Israelachvili *et al.* is that the shape of the aggregates that best satisfies the above two demands depends primarily on three factors, namely, the volume v of the hydrophobic part, length l of the hydrophobic chain and the effective head group area a of the hydrophilic part of the surfactant molecule. The length l and the volume v can be given by Tanford formulae

as,
$$v = 27.4 + 26.9n \ (\text{Å})^3 \tag{1.14}$$

$$l = 1.5 + 1.265n \ (\text{Å}) \tag{1.15}$$

where n is the number of carbon atoms in the linear alkyl chain of surfactant molecule.

Israelachvli and co-workers have shown, from packing considerations, that the allowed packing of surfactant molecules into aggregates can be conveniently described by dimensionless parameter which they called as the 'critical packing parameter', given by v/al. The value of this packing parameter will dictate the geometries for the association structures that will be formed in solution. Different values of packing parameter are compatible with different geometrical shapes of the surfactant aggregates. For a spherical micelle of radius, R and aggregation number, N the total volume of the micelle can be written as

$$(4/3)\pi R^3 = Nv \tag{1.16}$$

and the total surface area of the micelle can be written as

$$4\pi R^2 = Na \tag{1.17}$$

The packing criteria impose the restriction that the radius of the micelle cannot be more than the length of the hydrocarbon tail of the surfactant, l.

i.e., $$R = 3v/a \leq 1 \tag{1.18}$$

In terms of the packing parameter, $v/al \leq 1/3$

That means, when the packing parameter is less than 1/3, spherical micelles are the preferred form of aggregate structure. By a similar argument, it can be easily shown that the cylindrical micelles form when the packing parameter is between 1/3 and 1/2 and when it is >1/2 highly curved bilayer vesicles are preferred and then flat bilayers are formed as it approaches 1.

The second parameter which is equally important in dictating the structure of the supramolecular assembly is the curvature energy associated with the supramolecular aggregates and the contribution from the curvature energy is significant in the case of vesicles, bilayers, etc. In the classical curvature model introduced by Helfrich [16], the free energy per unit area of a bilayer associated with bilayer curvature is given by

$$\frac{F}{A} = \frac{1}{2}\kappa_b(c_1 + c_2 - c_s)^2 \tag{1.19}$$

where c_1 and c_2 denotes the two principal curvatures and c_s denotes the spontaneous curvature of the bilayer. Here κ_b is a measure of the rigidity of the bilayer, known as the bending modulus which is of the order of kT, where k is the boltzmann's constant and T, the temperature. It is worth mentioning that the spontaneous curvature arises from the packing considerations of the surfactant molecule. If the interaction between the polar heads is favoring a smaller packing area than that dictated by the tail-tail interactions, the surfactant monolayer will tend to curve so that the polar regions are on the inner side of the interface. On the contrary, if the head group packing prefers a larger area than that dictated by chain

interactions, the curvature will be such that the polar regions are on the outer side of the interface. According to the equation suggested by Helfrich, it can be seen that any deviation of the curvature from the mean curvature raises the free energy by an amount proportional to the square of the difference in mean curvature from the spontaneous curvature. Thus, the probability of formation of a structure by deviating from the spontaneous curvature will depend on the magnitude of κ_b. The molecular organization within each bilayer at normal temperature is 'liquid' like and the bending modulus, κ_b is expected to be relatively small and hence little energy is associated with deforming a fluid layer. However, intermolecular interaction between surfactant molecules can lead to a 'solid' like association within monolayer and hence an increase in the magnitude of κ_b would be expected. In such a system where κ_b is much higher than kT, the curvature energy makes a significant contribution to the free energy of aggregates and hence κ_b will have a strong influence in dictating the structure of supramolecular assemblies. Helfrich and others have suggested that the effective bending constant κ_b depends on the length scale defined by the 'persistence area' in anology with the persistence length of a polymeric chain [17]. For areas larger than the persistence area, the shape change do not cost appreciable energy whereas for smaller areas κ_b would have a finite value. This means that the effective bending modulus of a surfactant film in a vesicle of 60 nm diameter might be appreciably larger than that of the same film making up a vesicle of 10 μm diameter. Though, at this instant, it is very difficult to predict theoretically the magnitude of κ_b, one can expect that κ_b is mostly dependent on the surfactant chain length and the surfactant head group area.

1.9 Mixed surfactant systems

Chapter 1: Introduction

Mixed surfactant systems exhibit many novel features which have importance in theoretical as well as applied science. It is observed that mixtures of surfactants are used in almost all practical applications involving surfactants. This is not only due to the inherent difficulty in preparing isomerically pure surfactants but also due to the better performance output (synergism) reflected in surfactant mixtures. Another interesting feature of the mixed surfactant system is that one can easily manipulate the aggregate microstructure from micelles to cylindrical micelles to vesicles to liquid crystals by proper blending of suitable single chain surfactants. In the previous section a brief discussion was given about the different parameters which dictate the microstructure of aggregates in surfactant-water system. With this knowledge, one can easily show that it is possible to control these parameters by proper choice of surfactant mixtures. Spontaneous, single-walled, equilibrium vesicles of controlled size and surface charge can be prepared from mixtures of simple, commercially available, single-tailed cationic and anionic surfactants [13]. Formation of viscoelastic surfactant solutions have been found in mixtures of cationic surfactant C_nTAB and anionic surfactant sodium oleate [18]. Also such viscoelastic fluids are formed when cationic surfactants like cetyltrimethylammonium bromide (CTAB) is mixed with organic additives like sodium salicylate (SS) or sodium 3-hydroxy naphthalene 2-carboxylate (SHNC) [19]. Such an additive need not itself be micelle forming but will have profound influence in transforming the structure from spherical micelles to rod-like micelles to vesicles. An example of a general class of non-micelle forming additives is the 'hydrotropes'. The term 'hydrotropy' was coined by Neuberg for certain freely soluble organic salts which above a critical concentration, enhances the solubility of organic substances practically insoluble under normal conditions. For example, in contrast to the normal CMC for cetylpyridinium chloride which is reported to

17

be 9 x 10^{-4} M, Hoffmann *et al.* have shown that by changing the anion from chloride to salicylate a transition from spherical to cylindrical micelles occurs at lower concentration of 4.4 x 10^{-4} M [20]. Hence cationic-anionic surfactant mixtures and surfactant-hydrotrope mixtures are important class of compounds for a wide variety of applications, especially in the preparation of nanoparticles as discussed in the later section of the chapter.

1.10 Applications of surfactants

A brief account of the various applications of surfactant solutions in variety of industries such as soaps and detergents, pesticide formulations, petroleum mining, foods and pharmaceuticals, etc. is given below. One important property of surfactants which makes it an inevitable component in the day-to-day life is its detergency property. Detergency involves the removal of greasy or oily material or any unwanted particulate matter from solid surfaces such as fibers, fabrics, etc. In a surfactant solution the surfactant can be adsorbed at the air-water or solid-water interface thereby reducing the interfacial tension and this reduced interfacial tension changes the contact angle between oil and solid in such a way that easy detachment of the oil drop from the solid is possible. Secondly, this detached oil drop can be easily solubilized in the hydrocarbon interior of the micellar aggregates. For the removal of particulate matter, adsorption of the surfactant on to the solid surface is necessary in order to stabilize the particulate matters as dispersions in water.

One general class of formulations in which organic pesticides have been widely marketed is in the form of emulsifiable concentrate (EC). EC comprises the active ingredient that is the pesticide in use, along with a suitable emulsifier which is solubilized in hydrocarbon oil. When EC is diluted with water, it gives stable oil in water emulsion which

can be applied easily to the destination. The main role of the surfactant here is as an emulsifier to give a stable emulsion in the form of oil in water.

In pharmaceutical industries, the formulation of liposomes or vesicles is found to be promising as a carrier for water soluble or water insoluble drugs. When dispersions of liposomes are injected intravenously, they travel along the circulatory system and is shown to be taken up preferentially by certain organs in the body. Hence the controlled release of drugs from the liposomes and targeting to specific organs or specific conditions is the added advantage of liposomes as a drug carrier.

In petroleum mining, the prospect of increasing the yield of oil reservoirs by adding speciality chemicals containing surfactants to the injection water prompted much research in the subject of enhanced oil recovery, sometimes known as the tertiary oil recovery. Even after flooding with water, oil droplets remain trapped in the narrow pores by capillary forces due to the high interfacial tension between oil and water. By adding surfactants to the injection water, the interfacial tension can be reduced to sufficiently low values so that the trapped oil droplets can be released. This offers a novel way of increasing the yield of petroleum oil recovery in oil reservoirs.

Besides the above mentioned applications in industry, their potential uses in nanomaterial synthesis, biotechnology, reaction catalysis, etc. are numerous. They can improve the rate of reactions involving two immiscible liquids by orders of magnitude by increasing the solubilization of the reactants. They can be used to prepare very small solid particles like magnetic colloids, metallic catalysts, micro lattices, etc. Due to the large scale use in various fields, surfactant science has been a very active subject for both theoretical as well as applied research.

Chapter 1: Introduction

1.11 Moulding advanced materials through self-assembly

One immediate consequence of self-assembly is the ability to create hydrophobic and hydrophilic compartments in fluids [21]. These compartments can be used as solubilization sites for various reactants and hence as a microreactor for different classes of materials such as metals, semiconductors, ceramics, and polymers. Technological developments in various fields, such as adsorption, catalysis, separation, drug delivery, sensors, and photonic crystals require the development of ordered porous materials with controllable pore dimensions. Mesoporous materials with pore dimensions at the scale of a few nanometers can meet the demands of the growing applications emerging in different fields involving large molecules such as proteins and petroleum products. Microporous materials or zeolites, whose pore sizes are at the scale of a few angstroms, cannot meet these demands. Thus development of mesoporous materials gained importance. Quaternary ammonium cationic surfactants such as cetyltrimethylammonium bromide (CTAB) were used as templates to prepare highly ordered mesoporous silicate molecular sieves under hydrothermal conditions where pore size of the materials can be tuned in the range of a few tens of nanometers. Several good reviews have summarized the synthesis, characterization, and applications of mesoporous silicates [22]. The organic-inorganic self-assembly in the precursors of such material is driven by weak noncovalent bonds such as hydrogen bonds, van der Waals forces, and electrostatic interactions between the surfactants and inorganic moiety. It is reported that a synergetic self-assembly between organic surfactants and inorganic precursors is generally involved in the preparation of inorganic/organic mesostructured composites. Removal of surfactants from the composite material by heat treatment leads to the formation of desired highly ordered mesoporous materials. Thus, with the advances in the knowledge of the surfactant cooperative

self-assembly, the highly ordered mesoporous materials can be rationally designed and the synthesis can be controlled. The cooperative assembly of organic-inorganic composites also opens avenue for the generation of a variety of technologically important materials with highly ordered nanochannels, large surface area catalysts, and attractive liquid-crystal structures. Surfactants have also been employed as structure directing agents for the synthesis of various inorganic and polymeric materials in nanoscale dimensions. Of particular interest is the preparation of silver nanorods by controlling the reaction conditions. Surfactant assisted growth of silver nanorods with aspect ratio 5 to 20 have been investigated by Ni *et al.* [23]. The role of crystal defects (twinning) and preferential adsorption of surfactants in inducing the nanorod formation has been studied. The ability to manipulate the shapes of inorganic nanoparticles remains an important goal of modern materials science due to its various important applications.

1.12 Interfacial engineering for diagnostics and therapy

Colloidal particles with well defined particle size, morphology, microstructure, and surface characteristics are currently offering great promise as support in a large number of biotechnological, pharmaceutical, and medical applications such as diagnostics (assays), NMR imaging, bioseparation, cosmetics, and drug delivery systems [24]. For this reason, a large amount of work has been done for the design and preparation of colloidal materials with appropriate properties for interacting with biologically active macromolecules. Some of the commonly used strategies for the development of such materials include polymerization in microheterogeneous media to produce colloidal dispersions, self-assembled structures of surfactants and block copolymers, polyelectrolyte-surfactant complexes and engineered multifunctional dendrimer particles. The production of surface-functionalized materials has

long been motivated as a result of their application in biotechnologies that require the interaction of biomolecules with a given substrate either as film or as colloidal support, mainly for immobilizing biomolecules on a suitable substrate temporarily or permanently. Surface functionalization of materials is of importance in bio-diagnostics whether it is used as colloidal particles as in latex agglutination assays or as solid-phase supports as in immunoassays. Bio-diagnostics involves the detection of biological macromolecules such as proteins, bacteria, viruses, toxins, etc through a bio-recognition process. The property of specific interaction between an antigen and antibody (biological macromolecules) has been made use of in the selective estimation of various proteins. Polystyrene is a commonly used solid support for immobilization of antibodies in immunoassays [25]. There are different approaches for immobilizing biomolecules on polystyrene surfaces such as passive adsorption and covalent coupling. Passive adsorption makes use of the hydrophobic interaction between the solid phase and the biomolecules. There are many different covalent immobilization procedures reported in literature. An amino group can be introduced to polystyrene by nitration of the aromatic ring followed by reduction. The amino polystyrene was further activated by chemical reactions such as diazotization and the resulting surface was used for efficient antibody immobilization. Covalent binding using bifunctional cross-linking agents such as glutaraldehyde and activation of the surface using isocyanate or carbodiimide have also been employed. Also surface modification through self-assembled monolayers, adsorption of polymers or nanoparticles with specific functionalities and grafting of functional materials, etc. are also used for efficient binding of biomolecules on the surfaces.

CHAPTER 2

Experimental methods

Chapter 2: Experimental methods

This chapter deals with the key experimental techniques used for the structural studies of supramolecular aggregates and nanomaterials. The basic principles and the experimental details of these techniques are explained in brief.

2.1 Light Scattering

Application of light scattering technique as a probe of macromolecular properties like size, shape, molecular weight, etc. has attracted considerable interest in colloid and material chemistry. The angular distribution of the scattered light intensity from a colloidal solution depends on various factors like size and shape of the colloidal particle, optical properties of the scatterer such as its polarizability, refractive index, etc., and the wavelength of the incident light. In a basic light scattering experiment, one measures the average scattered intensity I_s (that is the average rate of flow of energy per unit area of cross section) or the energy spectrum of intensity $S(\omega)$ where ω is the angular frequency of the scattered light. Both I_s and $S(\omega)$ are measured at various angles as they are angle dependent. The I_s bears information about the static properties of the scatterer whereas $S(\omega)$ bears information regarding the dynamics of the scatterer. Hence, the light scattering experiments can be classified under two broad categories, namely the static light scattering in which one measures the average scattering intensity at various angles and the dynamic light scattering in which the energy spectrum of intensity or the time dependence of the intensity is measured. Dynamic light scattering has been used in the present study.

2.1.1 Dynamic Light Scattering (DLS)

In a classical light scattering experiment one assumes that the particles are at fixed positions in space, but in reality the suspended particles are not stationary; rather they diffuse

in a random walk fashion known as the Brownian motion. Since the net intensity seen by the detector is a result of the superposition of all the waves scattered from the scattering volume, the intensity fluctuate randomly in time as the phases of the scattered waves fluctuate randomly due to the random fluctuations in the relative positions of the particles which scatter light. This time dependence or the fluctuations in the net scattered intensity forms the basis of the Dynamic Light Scattering (DLS) experiment [26].

The key concept underlying in a DLS experiment is the fact that time scale of these fluctuations depends on the size of the diffusing particles. Small particles diffuse in the solution relatively rapidly resulting in a rapidly fluctuating intensity signal as compared to the larger particles which diffuse more slowly. Figure 2.1 shows representative intensity-time profiles for small and large size particles as observed on the same time scales for both the particles, as a result of variations in the position of an essentially fixed number of particles in the scattering volume. A mathematical procedure known as the autocorrelation is used to
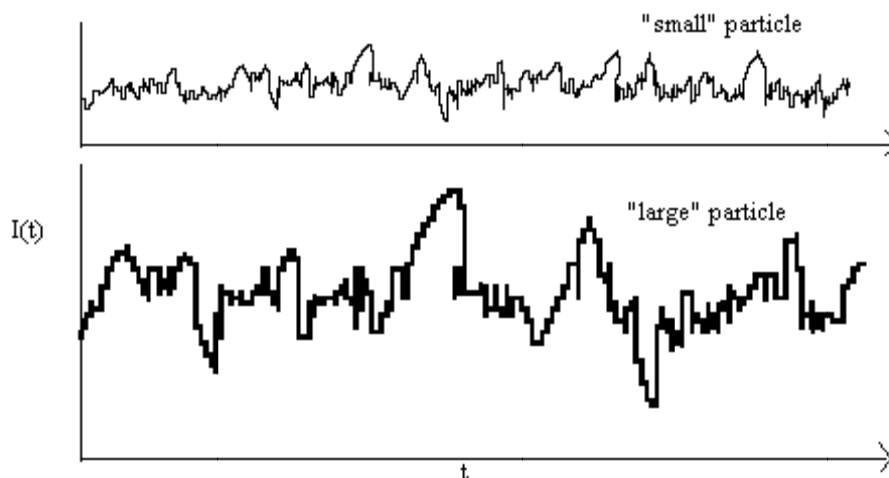
Figure 2.1 Typical fluctuations in scattered intensity for 'large' and 'small' particles when observed in the same time scale.

obtain quantitative information from these kinds of fluctuations in the scattered intensity. Hence this technique is also known under the name photon correlation spectroscopy.

The autocorrelation function, denoted by $C(\tau)$, represents the correlation between the values of the scattered intensity at a given time t and at a later time $(t+\tau)$. By representing intensity at an arbitrary time as $I(o)$ and those at a later time τ as $I(\tau)$, the autocorrelation function can be written as

$$C(\tau) = <I(o).I(\tau)> \qquad (2.1)$$

When the sampling interval τ becomes very large, there should not be any correlation between the pairs of sampled intensities and hence the above equation reduces to

$$C(\infty) = <I(o)>^2 \qquad (2.2)$$

An autocorrelator accepts the digital photo counts from the detector which represents the light scattering intensity $I(t)$ and computes the second order correlation function, normalized with the long time correlation data $<I>^2$. The normalized time correlation function $g^{(2)}(t)$ of the scattered intensity is given by

$$g^{(2)}(\tau) = \frac{<I(o)I(\tau)>}{<I>^2} \qquad (2.3)$$

For photo counts obeying Gaussian statistics, the relationship between $g^{(2)}(\tau)$ and the first order correlation function of the electric field $g^{(1)}(\tau)$ is given by the Siegert relationship

$$g^{(2)}(\tau) = \beta + A\left|g^{(1)}(\tau)\right|^2 \qquad (2.4)$$

where β is the baseline and A is an adjustable parameter which is dependent on the scattering geometry and independent of τ.

Chapter 2: Experimental methods

For a suspension of monodisperse, rigid, spherical particles undergoing Brownian diffusion, the correlation function decays exponentially as

$$g^{(1)}(\tau) = \exp(-Dq^2\tau) \qquad (2.5)$$

where D is the translational diffusion coefficient and q is the wave vector transfer, q

——, where 2   is the scattering angle and   is the wavelength). For small, dilute, non-interacting spheres the hydrodynamic radius R_h can be obtained from the translational diffusion coefficient using the Stokes-Einstein relationship given by

$$D = kT / (6\pi\eta R_h) \qquad (2.6)$$

where k is the Boltzmann's constant, η is the solvent viscosity, and T is the absolute temperature. If the particle is nonspherical then R_h is taken as the apparent hydrodynamic radius. A lay out of the experimental setup of DLS is shown in Figure 2.2.
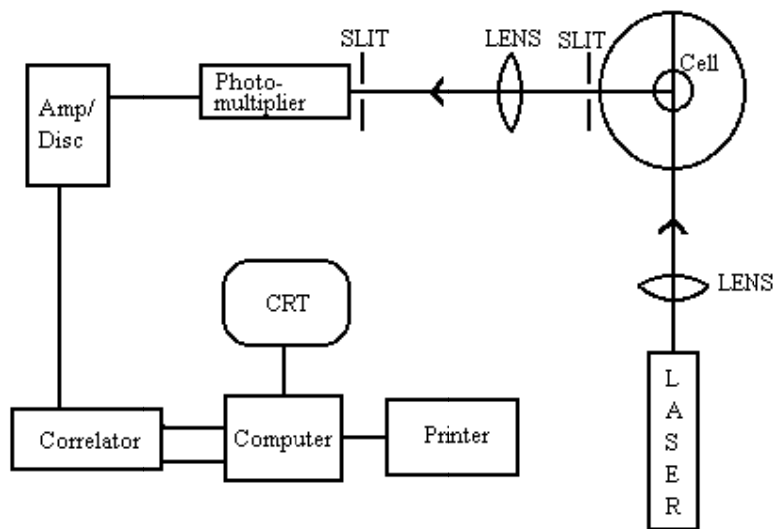
Figure 2.2 Block diagram of a typical DLS instrument.

2.1.1a Effect of polydispersity

Chapter 2: Experimental methods

In most of the practical systems, it is almost impossible to have all the particles having the same size. It is thus important to consider the effect of polydispersity in such systems. When a broad distribution of diffusion coefficient is present in the system, each D contributes its own exponential and the mathematical equation 2.5 will be modified as

$$g^{(1)}(\tau) = \int_0^\infty G(\Gamma) \exp(-\Gamma\tau) \, d\Gamma \qquad (2.7)$$

where $\Gamma = Dq^2$ is the decay constant for a given particle size. The distribution $G(\Gamma)$ represents the relative intensity of light being scattered with decay constant Γ and will be a function of the number and size of scatterers. Equation 2.7 can be recognized as the Laplace transform of $G(\Gamma)$ with respect to Γ. Hence an inverse Laplace transform on the above equation can be used to obtain $G(\Gamma)$ but a much simpler method, known as the method of cumulants [27], has been used traditionally to analyze the polydispersity in DLS experiments. Expanding the term $\exp(-\Gamma\tau)$, in the above equation, about a mean value $\bar{\Gamma}$ such that

$$\exp(-\Gamma\tau) = \exp(-\bar{\Gamma}\tau).\exp(-[\Gamma-\bar{\Gamma}]\tau) \qquad (2.8)$$

$$= \exp(-\bar{\Gamma}\tau).[1-(\Gamma-\bar{\Gamma})\tau + (\Gamma-\bar{\Gamma})^2\tau^2/2! + ...] \qquad (2.9)$$

When $G(\Gamma)$ is relatively narrow, terms with order 3 and above can be neglected, as the relative magnitude of contributions of the terms in the bracket falls of rapidly with increasing order and substituting it in equation 2.7, we get

$$g^{(1)}(\tau) = e^{(-\bar{\Gamma}\tau)} \left[\int_0^\infty G(\Gamma)d\Gamma - \tau\int_0^\infty G(\Gamma)\Gamma d\Gamma + \bar{\Gamma}\tau\int_0^\infty G(\Gamma)d\Gamma + \frac{\tau^2}{2}\int_0^\infty (\Gamma-\bar{\Gamma})^2 G(\Gamma)d\Gamma \right] (2.10)$$

$$= e^{(-\bar{\Gamma}\tau)} \left[1 - \bar{\Gamma}\tau + \bar{\Gamma}\tau + \frac{\mu_2\tau^2}{2} \right] \qquad (2.11)$$

where the first cumulant $\bar{\Gamma}$ and the second cumulant μ_2 are defined as

$$\bar{\Gamma} = \int\limits_{0}^{\infty} G(\Gamma)\Gamma d\Gamma \tag{2.12}$$

$$\mu_2 = \int\limits_{0}^{\infty} G(\Gamma)\left(\Gamma - \bar{\Gamma}\right)^2 d\Gamma \tag{2.13}$$

Thus, we get

$$g^{(1)}(\tau) = e^{(-\bar{\Gamma}\tau)}\left[1 + \frac{\mu_2\tau^2}{2}\right] \tag{2.14}$$

The first and second cumulant respectively give the mean and variance of the distribution $G(\Gamma)$ and by fitting the experimentally observed $g^{(1)}(\tau)$ to a quadratic in τ we can get the mean, $\bar{\Gamma}$ and the variance, μ_2. The ratio of variance to the square of the mean is a measure of the polydispersity of the diffusion coefficient and this is represented as the polydispersity index in DLS experiments.

In the present work Dynamic light scattering measurements were performed using a Malvern 4800 Autosizer employing a 7132 digital correlator. The light sources used were either an Ar-ion laser operated at 514.5 nm with maximum power output of 2 W or a 5 mW helium-neon laser at a wavelength of 633 nm. All measurements were carried out at 25.0 ± 0.1 ^{o}C using a circulating water bath. Cylindrical quartz cells of 10 mm diameter were used in all of the light scattering experiments. Measurements were made at an angle of 130°.

2.2 Small angle neutron scattering (SANS)

Thermal neutrons have found out to be an ideal probe for investigating the structure and dynamics of materials at microscopic level [28-30]. Neutron scattering consists of a whole family of techniques and small angle neutron scattering (SANS) is one of these techniques [31-33]. Different neutron scattering techniques give complementary information

about any material. For example, coherent elastic scattering (diffraction) of neutrons gives the crystallographic or the magnetic structure of the material substance, coherent inelastic scattering experiments determine phonon dispersion curves, and incoherent inelastic and quasielastic measurements on hydrogenous samples give the nature of random molecular motions (translational and/or rotational) in solids and liquids.

The technique of SANS is used for studying the structure of a material in the length scale of 10-1000 Å. SANS is a neutron diffraction technique which involves scattering of a beam of neutrons from the sample and measuring the scattered neutron intensity as a function of the scattering angle. The wave vector transfer q ($= \frac{4\pi \sin \theta}{\lambda}$, where 2θ is the scattering angle and λ is the neutron wavelength) in these experiments is small, typically in the range of 0.001 to 1.0 Å^{-1} and the wavelength of neutron used for these experiments is usually 4-10 Å. Since the small q values occur at small scattering angles, therefore this is known as the small angle neutron scattering. The SANS experiment determines the differential cross-section ($\frac{d\Sigma}{d\Omega}$) since it is this which contains all the information on the shape, size, and interactions of the scattering bodies (assemblies of scattering centres) in the sample. It is seen that the scattering cross-section from a collection of particles consists of two terms, the first of which depends on the intraparticle scattering and the second on interparticle scattering.
The differential cross-section is given by

$$\frac{d\Sigma}{d\Omega}(q) = n(\rho_p - \rho_m)^2 V^2 P(q) S(q) \qquad (2.15)$$

where n is the number of particles per unit volume of the sample, V is the volume of one scattering body, $(\rho_m - \rho_s)^2$ is known as contrast factor, P(q) is a function known as the form or

shape factor, S(q) is the interparticle structure factor and q is the scattering vector. The differential scattering cross-section has dimensions of $(length)^{-1}$.

2.2.1 Contrast factor

The square of the difference between the average scattering length density of the particle and the average scattering length density of the solvent $(\rho_m-\rho_s)^2$ is known as the contrast factor. As mentioned above, the scattered neutron intensity in a SANS experiment depends on $(\rho_m-\rho_s)^2$. The contrast factor in SANS experiments is equivalent to the contrast term in optics, where it is decided by the difference in the refractive indices of the particle and the solvent. The scattering length of hydrogen is negative (= -0.3723 x 10^{-12} cm) and for deuterium, it is positive (= 0.6674 x 10^{-12} cm). Hence it is possible to have a good contrast between the hydrogenous particle and the solvent by deuterating either the particle or the solvent.

2.2.2 Determination of Intraparticle Structure

In the previous section we have seen that the differential scattering cross-section is related to the intraparticle structure factor P(q) and the interparticle structure factor S(q). The intraparticle structure factor is the square of the particle form factor. It depends on the shape and size of the particles and can be denoted for any geometry.

$$P(q) = \left(\left\langle |F(q)|^2 \right\rangle\right)$$
(2.16)

Dilute systems are ideally suited for studying the shapes and sizes of the particles as the concentration of particles is very low. The interparticle distances are much larger than the particle size in these systems, the interparticle interference is negligible and S(q)~1. Thus the

scattering distribution depends on the functionality of P(q) and the equation for dilute systems becomes

$$\frac{d\Sigma}{d\Omega} = n(\rho_p - \rho_m)^2 V^2 P(q) \tag{2.17}$$

The expressions for P(q) for different structures of the particles are available [34, 35]. The expressions for some of the shapes are given below.

(i) Sphere of radius R

$$P(q) = \left[\frac{3(\sin qR - qR\cos qR)}{(qR)^3}\right]^2 \tag{2.18}$$

(ii) Ellipsoid of major axis 2a and minor axis 2b = 2c

$$P(q) = \int_0^1 [F(q,\mu)]^2 d\mu \tag{2.19}$$

where $F(q,\mu) = 3(sinx\text{-}xcosx)/x^3$ and $x = q[a^2\mu^2 + b^2(1-\mu^2)]^{1/2}$, μ is the cosine of the angle between the directions of major axis and the wave vector transfer q.

(iii) Cylinder of radius R and length L = 2l

$$P(q) = \int_0^{\pi/2} \frac{\sin^2(ql\cos\beta)}{q^2l^2\cos^2\beta} \frac{4J_1^2(qR\sin\beta)}{q^2R^2\sin^2\beta} \sin\beta d\beta \tag{2.20}$$

where β is the angle between the axis of the cylinder and bisectrix. J_1 is the Bessel function of order unity. The disk being special case of cylinder when L<<R. It can be shown that for

cylindrical particle P(q) varies as 1/q in the q range of 1/L < q < 1/R and as $1/q^2$ for disk-like particle in the q range of 1/R < q < 1/L.

It has been observed that P(q) has a slope of -1 for cylindrical particles and -2 for disk-like particles in the intermediate q range. Irrespective of the shape of the particles, P(q) can be written in simple forms for limited q ranges. The most important of these simple forms are the Guinier approximation and the Porod law.

2.2.3 Polydisperse particles

In practice, colloidal systems typically contain a distribution of particle sizes. Hence in the case of polydisperse systems (particles having different sizes), the scattering cross-section is given by

$$\frac{d\Sigma}{d\Omega}(q) = n(\rho_p - \rho_m)^2 \int V^2(R)P(q,R)f(R)dR \tag{2.21}$$

where f(R) is the particle size distribution. Usually, log normal or Schultz distribution is assumed for the polydispersity.

2.2.4 Guinier Approximation

When there are no interparticle interactions (i.e. in the dilute limit) it is possible to obtain important structural information from the scattering spectra. In the small q region (qRg < 1), P(q) decreases in an exponential manner and is known as Guinier approximation [34]

$$P(q) = \exp\left(-\frac{q^2 Rg^2}{3}\right) \tag{2.22}$$

where Rg is the radius of gyration of the particle and is defined as

$$Rg^2 = \frac{\int vr^2 dv}{V} \qquad (2.23)$$

Thus a plot of logarithm of the scattering intensity versus q^2 will be a straight line in the small q region and the slope can give the radius of gyration of the particle.

2.2.5 Porod law

As already discussed, Guinier limit mainly focuses on the scattering observed at low or intermediate values of q. Structural information can also be obtained from the higher q-region without the need of any assumptions. At large q values, for homogenous particles with sharp boundaries, P(q) varies as 1/q4 and is known as the Porod law [36]. For a spherical particle at large q, P(q) can be defined as

$$P(q) = \frac{2\pi S}{V} \frac{1}{q^4} \qquad (2.24)$$

where S is the surface area and V is the volume of the scattering particle.

2.2.6 Determination of Interparticle structure factor

The structure factor S(q) can have a pronounced effect on the appearance of the SANS experimental data, particularly at the scattering intensity in the low q-region. The contribution from S(q) cannot be neglected when the concentration of particles is large and they start interacting with each other. Especially in the case of charged systems the accounting of this contribution is very much necessary for the proper analysis of the data. For concentrated systems, we can say that S(q) $\neq$ 1. It is not always possible to dilute the system as the particle structure could change on dilution as in the case of micellar solutions. Thus the consideration of S(q) in the analysis of the scattering data is very important. The nature of S(q) depends on

the structure and organization of the particles and the type of interactions existing between the particles. In general, S(q) shows several maxima and minima of decreasing amplitude and the first peak in S(q) occurs at $q_{max} \sim 2\pi/d$, where d is the average distance between the particles. The expression for S(q) depends on the relative positions of the particles. In the case of isotropic system, S(q) can be written as

$$S(q) = 1 + 4\pi n \int (g(r) - 1) \frac{\sin qr}{qr} r^2 dr \qquad (2.25)$$

Where g(r) is the radial distribution function i.e. the probability of finding another particle at a distance r from a reference particle centered at the origin. The details of g(r) depend on the interaction potential U(r) between the particles [37]. Thus one has to have the knowledge of U(r) for calculating S(q) parameter. This in turn implies that the measured S(q) can be used to obtain information about the interaction potential U(r). U(r) could consists of several terms such as (i) hard sphere term Uhs(r), (ii) van der Waals attractive term Uvw(r), (iii) solvent mediated term Us(r) and (iv) Coulomb repulsion term Uc(r). Uc(r) is important in ionic micelles, as they are charged. Similarly, it may be noted that Us(r) is important in nonionic micelles. Colloidal micellar solution is essentially a macrofluid on the length scales probed in SANS. It is thus possible to calculate g(r) or S(q) for these solutions using the methods which have been developed for liquids. It can be noted that g(r) is related to the total correlation h(r) between the two particles separated by distance r as

$$g(r) = 1 + h(r) \qquad (2.26)$$

Further, we note that h(r) consists of two contributions and is given by Ornstein-Zernike equation (OZE) [38]

$$h(r) = n \int C(r')h(|r - r'|)d^3r' \tag{2.27}$$

where C(r) is the direct correlation function. To solve OZE, one needs an additional relation (referred as closure relation) between h(r) and C(r). Depending on the approximations involved, various closure relations have been proposed in the literature. Some of these are given below.

(a) Mean spherical approximation (MSA) gives

$$C(r) = -\beta U(r), r > \sigma \tag{2.28}$$

$$h(r) = -1, r \leq \sigma \tag{2.29}$$

where $\beta = 1/kT$ and σ is the particle diameter.

(b) Percus-Yevick approximation (PYA) gives

$$C(r) = 1 - \exp[\beta U(r)] \tag{2.30}$$

(c) Hypernetted chain approximation (HNCA) gives

$$C(r) = -\beta U(r) + h(r) - \ln[h(r) + 1] \tag{2.31}$$

Small angle neutron scattering experiments were carried out using SANS diffractometer at the Dhruva reactor, Bhabha Atomic Research Centre, Trombay. The diffractometer makes use of a beryllium oxide filtered beam with a mean wavelength (λ) of 5.2 Å. The angular distribution of the scattered neutrons is recorded using a one-dimensional position-sensitive detector (PSD). The accessible wave vector transfer (q) range of the diffractometer is 0.017-0.35 Å^{-1}. The PSD allows simultaneous recording of data over the full

q. The samples were held in a quartz sample holder of 0.5 cm thickness. In all the measurements the temperature was kept fixed at 30 ^{o}C. The measured SANS data have been corrected and normalized to absolute unit (as cross-section per unit volume), using standard procedures.

2.3 Rheology

Surfactant phases have been identified that impart controllable and useful viscous and elastic rheological properties to a wide variety of aqueous liquids. Rheological properties are crucial in food processing, cosmetic formulations, paint formulations, pharmaceutical formulations, etc. Rheological measurements are also essential from a fundamental point of view because they are used to characterize a system. Rheology is the science of deformation and flow of matter. It essentially deals with the response of the materials when it is subjected to some external forces. The behavior can be best illustrated by a simple shear experiment as shown in Figure 2.3.

F ⟶

V= v

V = 0

x

y
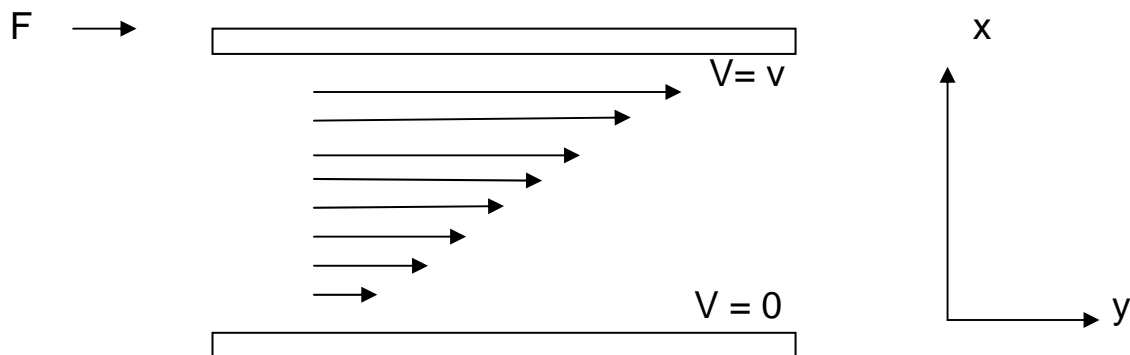
Figure 2.3 Geometry for a simple shear along y – direction with a velocity gradient along x-direction.

Consider a fluid contained between two parallel plates, each of area A. If a force F is applied to the upper plate such that it moves with a velocity v relative to the lower plate of the

parallel plates. If the displacement of a given element located at dx is dy, then the shear strain (γ) and the shear rate ($\dot{\gamma}$) are defined as

$$\gamma = dy/dx \text{ and } \dot{\gamma} = d\gamma/dt = dv/dx \qquad (2.32)$$

Also, the force F acting at the upper plate produces a shear stress given by

$$\sigma_s = F/A \qquad (2.33)$$

In the case of a liquid, shear rate is proportional to the shear stress σ_s as shown by the Newton's equation,

$$\sigma_s = \eta_0 \dot{\gamma} \qquad (2.34)$$

The proportionality constant η_0 is known as the viscosity of the liquid. But in the case of an elastic solid, the shear stress σ_s is proportional to the strain γ as given by the Hooke's law,

$$\sigma_s = G_0 \gamma \qquad (2.35)$$

Here the proportionality constant G_0 is called the rigidity modulus or the shear modulus. The Newton's law and the Hooke's law are two limiting cases of the response of a material under shear. The behavior of many materials cannot be described by either Newton's law or Hooke's law but they exhibit both viscous and elastic responses and hence, they are designated as viscoelastic materials and for such a fluid the stress-strain relationship can be described by a linear differential equation

$$\left(1 + \alpha_1 \frac{\partial}{\partial t} + \alpha_2 \frac{\partial^2}{\partial t^2} + ..\right)\sigma_s = \left(\beta_0 + \beta_1 \frac{\partial}{\partial t} + \beta_2 \frac{\partial^2}{\partial t^2} + ..\right)\gamma \qquad (2.36)$$

where the coefficients α_i and β_i are material parameters.

In the literature, several mechanical models have been suggested to describe the behavior of linear viscoelastic materials [39, 40]. Majority of the models are approximated by different combinations of one or more viscous elements (i.e., a dashpot) and one or more

elastic elements (i.e., a spring). Whether a viscoelastic material behaves like an elastic solid or viscous liquid depends on a characteristic time known as the relaxation time (τ_R) of the material and is equal to the ratio η_0/G_0. For time scales smaller than τ_R, the material behaves like an elastic solid while for time scales greater than τ_R, it behaves like a viscous fluid. Because of this time dependent nature, the dynamic response of these materials becomes important to characterize their rheological behavior.

G
(elasticity)

η
(viscosity)
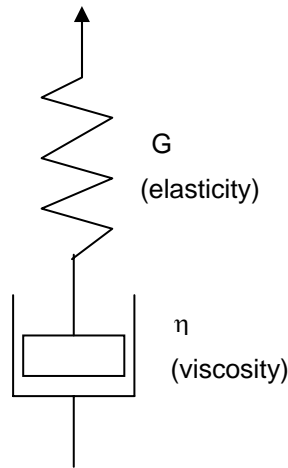
Figure 2.4 A Maxwell model for viscoelastic fluid.

Dynamic methods of measurements involve looking the response of the material subjected to periodic stress or strain. When a linear viscoelastic material is subjected to a sinusoidal deformation at an angular frequency, ω, the response of the liquid consists of a sinusoidal stress which is out of phase with the strain, the phase angle being given as δ. The shear strain exhibited by the liquid can be expressed as

$$\gamma(t) = \gamma_0 \exp{(i\omega t)} \tag{2.37}$$

where γ_0 is the strain amplitude. The corresponding shear rate is given by

$$\dot{\gamma}(t) = i\omega\gamma_0 \exp(i\omega t) = i\omega\gamma(t) \tag{2.38}$$

Shear stress developed will always be sinusoidal with the phase angle δ, thus

$$\sigma_s(t) = \sigma_0 \exp(i\omega t + \delta) \tag{2.39}$$

For an oscillatory shear, we can define a complex shear modulus G^* as

$$G^* = \frac{\sigma_s(t)}{\gamma(t)} = \frac{\sigma_0}{\gamma_0}(\cos\delta + i\sin\delta) = G' + iG'' \tag{2.40}$$

where G' and G'' are referred as the storage modulus and the loss modulus respectively. Thus, from the phase angle δ and the amplitudes of the shear stress and shear strain, it is possible to calculate the storage modulus and loss modulus, using equations

$$G' = G_0\cos\delta \text{ and } G'' = G_0\sin\delta \tag{2.41}$$

Similarly we can define the complex viscosity η^* as

$$\eta^* = \frac{\sigma_s(t)}{\dot{\gamma}(t)} = \frac{G^*}{i\omega} = \eta' - i\eta'' \tag{2.42}$$

Thus, $\qquad \eta'(\omega) = G''/\omega \text{ and } \eta''(\omega) = G'/\omega \tag{2.43}$

As mentioned earlier, the rheological properties of viscoelastic materials can be represented by simple mechanical models. One such model is the Maxwell element in which a spring and a dashpot are connected in series as shown in Figure 2.4.

With this combination, the stress is same on both the elements connected in series and strain is the sum of the strain from each elements. i.e.,

$$\gamma = \gamma_1 + \gamma_2 \text{ and } \dot{\gamma} = \dot{\gamma}_1 + \dot{\gamma}_2 \tag{2.44}$$

For the viscous element

$$\dot{\gamma}_1 = \frac{\sigma_s}{\eta_0} \tag{2.45}$$

And for the elastic component

$$\gamma_2 = \sigma_s/G_0 \text{ and } \dot{\gamma}_2 = \dot{\sigma}_s/G_0 \tag{2.46}$$

Hence for the Maxwell model, the differential equation becomes

$$\dot{\gamma} = \frac{\sigma_s}{\eta} + \frac{\dot{\sigma}_s}{G_0} \tag{2.47}$$

In terms of the relaxation time, the above equation can be written as

$$\sigma_s + \tau_R \dot{\sigma}_s = \eta_0 \gamma \tag{2.48}$$

where $\tau_R = \eta_0/G_0$ is the relaxation time

By substituting $\dot{\gamma} = i\omega\gamma$ and $\dot{\sigma}_s = i\omega\sigma_s$ in the above equations, we get the complex shear modulus as

$$G^* = \frac{\sigma_s}{\gamma} = \frac{G_0 i\omega\tau_R}{(1+i\omega\tau_R)} \tag{2.49}$$

Thus, we have

$$G' = \frac{G_0(\omega\tau_R)^2}{1+(\omega\tau_R)^2} \tag{2.50}$$

$$G'' = \frac{G_0\omega\tau_R}{1+(\omega\tau_R)^2} \tag{2.51}$$

According to the Maxwell model the real part of the dynamic modulus $G'(\omega)$ increases with frequency ω at low frequencies and it reaches a plateau value equal to the plateau modulus G_0 at high frequencies. The imaginary part of the modulus $G''(\omega)$, increases first and passes through a maximum at $\omega\tau_R = 1$. A convenient way of representing the storage and the loss moduli of a viscoelastic fluid is the so-called Cole-Cole plots in which the loss modulus $G''(\omega)$ is plotted against the storage modulus $G'(\omega)$. A Maxwell material can be characterized by a semicircular Cole-Cole plot centered on the $G'(\omega)$ axis. Thus, with the help of the above mentioned expressions, the Maxwell model can be used to describe the viscoelastic properties of materials.

2.3.1 Methods of measurement

Chapter 2: Experimental methods

There are basically three classes of viscometers that are employed depending on the choice of the particular requirement and on the range of viscosities to be measured. They are known as capillary viscometers, rotational viscometers, and moving body viscometers. Here emphasis is given only to rotational viscometers as they can be used at various shear rates and hence the best suited ones for non-Newtonian fluids.

Rotational viscometer consists of two basic parts separated by the fluid being tested. The parts could be a concentric cylinder, a parallel plate or a cone and plate. In all these cases one of the parts rotates relative to other and this produces a shearing action in the fluid. The resulting couple on the stationary part is measured from which the stress and hence the viscosity can be obtained.

(i) Concentric cylinder viscometer

If the gap between the two concentric cylinders is small enough and the cylinders are in relative motion, the test liquid experiences an almost constant shear rate. If the radii of the outer and the inner cylinders are R_0 and R_i respectively and the angular frequency of rotation of outer cylinder is Ω, then the shear rate is given by,

$$\dot{\gamma} = \frac{2\Omega R_0^2}{(R_0 - R_i)} \tag{2.52}$$

For the gap to be classed as narrow gap and the above approximation to be valid to within a few percent, the ratio of R_i to R_0 must be greater than 0.97. If the couple on the inner cylinder is C, then the shear stress in the liquid is defined as

$$\sigma_S = \frac{C}{2\pi R_0^2 L} \tag{2.53}$$

where L is the effective immersed length of the liquid that is being sheared.

(ii) Parallel-plate viscometer

For torsional flow between parallel plates the shear rate at the rim is given by

$$\dot{\gamma} = \frac{R\Omega}{h} \tag{2.54}$$

where R is the radius of the plate, h is the gap thickness between the plates and Ω is the angular velocity of rotation. If C is the couple on one of the plates, then the shear stress is given by

$$\sigma_s = \frac{2C}{\pi R^3} \tag{2.55}$$

(iii) Cone-and-plate viscometer

In the cone-and-plate geometry, the shear rate is very nearly the same everywhere in the liquid, provided the cone angle, θ is small. The shear rate in the liquid is given by

$$\dot{\gamma} = \Omega/\theta \tag{2.56}$$

If C is the couple on the cone, then the shear stress is given by

$$\sigma_s = \frac{3C}{2\pi R^3} \tag{2.57}$$

Rheological measurements were conducted at 25 $^{\circ}$C using an Anton Parr Physica MCR 101 rheometer in a double gap concentric cylinder geometry (DG 26.7) with a Peltier temperature control. Frequency-sweep measurements were done at a constant stress (chosen in a linear viscoelastic range) over a frequency range of 0.01 to 100 rad/s.

2.4 Cryo-TEM

Cryogenic transmission electron microscopy (Cryo-TEM) is a form of electron microscopy where the sample is studied at cryogenic temperatures (usually liquid nitrogen temperatures). Cryo-TEM has become a powerful complementary tool to small-angle X-ray

and neutron scattering, light scattering, nuclear magnetic resonance, and rheological measurements in the study of soft matters. In cryo-TEM, the sample is frozen and the frozen sample grid is then kept at liquid nitrogen temperature in the electron microscope and digital micrographs are collected with a camera.

Cryo-TEM is of great importance to soft matter science due to the fact that direct imaging of liquids is not possible in a high-vacuum TEM chamber because of the vapor pressure of solvents and molecular diffusion. However, most self-assembled structures, with an extensive variety of shapes, such as spherical, worm-like micelles, vesicles, lamellar sheets, sponge-phases, nanotubes, networks, disks, as well as many intermediate and mutative phases are stable only in their native solution conditions including concentration, temperature, pH, and the presence of other molecules such as salts. However, cryo-TEM provides in situ imaging of various delicate structures of soft matter, including liquid systems. In cryo-TEM, a wide range of length scales can be directly imaged, ranging from a few nanometres to several micrometres. Moreover, if several distinctively different aggregate shapes exist in solution, the analysis of scattering spectra is a tedious process. On the other hand, cryo-TEM can easily differentiate between the topologies that are difficult to resolve by scattering such as between small disk objects and spherical micelles, or between narrow ribbon elements and cylindrical micelles.

Cryo-TEM studies were performed using Technai G2 12 BioTWIN at Indian Institute of Technology Bombay, Mumbai. A drop of sample was put on holey carbon grids and then the excess sample was removed by blotting with filter paper. Thereafter, the grids were plunged into liquid ethane using an automated plunger and transferred into a grid holder

kept in liquid nitrogen. The samples were mounted in a cryo specimen holder and observed in the cryo-TEM instrument.

2.5 UV-vis spectroscopy

Electromagnetic radiation is absorbed or emitted only in discrete packets known as the photons. The energy E of the photon is defined as

$$E = h\nu \tag{2.58}$$

where h is the planck's constant and ν is the frequency of the electromagnetic radiation. Absorption of radiation occurs when a quantum of radiant energy coincides with an allowed transition to a higher energy level or state of the atom or molecule under study [41, 42]. Transmittance (T) is defined as the ratio of the radiant power transmitted by the sample to the radiant power incident on the sample. Thus

$$T = I/I_0 \tag{2.59}$$

The absorbance A is defined as the negative logarithm of transmittance. The fundamental law underlying the practice of ultraviolent - visible spectroscopy is the Beer-Lambert's law which relates the absorbance of the sample with the concentration of the absorbing species as follows

$$A = -logT = \varepsilon bc \tag{2.60}$$

where c is the concentration in moles per litre, b is the length of the path of the light beam in the sample, and ε is the molar absorptivity, which depends on the wavelength and the nature of the absorbing species [43].

Spectrophotometer is the instrument which furnishes the ratio of the incident to the transmitted radiant power as a function of spectral wavelength. The basic components of the spectrophotometer are (i) source (ii) monochromator (iii) sample compartment (iv) detector

and (v) recorder. The double beam recording spectrophotometer features a continuous change in the wavelength and an automatic comparison of the light intensities of sample and the reference material. The instrument either plots the transmittance or the absorbance as a function of the wavelength of light [44].

In present work Jasco V-650 spectrophotometer was used for recording the absorbance of the sample at a given wavelength.

2.6 Electrochemical technique

An instrument known as the potentiostat has control of the voltage across the working electrode-counter electrode pair, and it adjusts this voltage to maintain the potential difference between the working and the reference electrode (which it senses through a high-impedance feedback loop) in accord with the program defined by a function generator. One can also view the potentiostat as an active element whose job is to force through the working electrode whatever current is required to achieve the desired potential at any time. Since the current and the potential are related functionally, that current will be unique. Chemically, it is the flow of electrons needed to support the active electrochemical processes at rates consistent with the potential value. Thus in an electrochemical set up, the response from the potentiostat (the current) actually is the experimental observable [45]. There are three basic electrochemical processes that are considered useful in transducers for sensor applications: conductimetry, potentiometry, and (volt)amperometry. After applying a potential, when the current is recorded as a function of time, the technique is called chronoamperometry.

2.6.1 Instrumentation

The conventional voltametric set up consists of a waveform generator to produce the excitation signal, a potentiostat to apply this signal to an electrochemical cell, a current to

voltage converter to measure the resulting current, and data recorder to display the voltammogram.

2.6.2 Interdigitated array (IDA) microelectrodes

Silver coated IDA microelectrodes were fabricated. Each electrode had 20 digital pairs with 300 μm digit width. The PCB connector pitch is 2.5 mm wide. The two silver lines at the opposite faces of the membrane were used as two electrodes, which were held by a plastic clip holder with platinum contacts from which connections to the instruments were made.

Electrochemical measurements were performed at room temperature using an Autolab potentiostat / galvanostat, model PGSTAT20 (Eco Chemie, The Netherlands). The equipment was connected to a PC via an Autolab interface and controlled using Autolab GPES. The electrochemical cell was formed by a two-electrode arrangement using silver interdigitated screen-printed electrodes as already described. Current voltage characteristics of the polymer modified electrode were measured in the potential range from −0.5 V to 0 V. Pulsed amperometic measurements were carried out by applying pulse of -0.1 V for 2 seconds.

2.7 Zeta Potential

The liquid layer surrounding the particle exists as two regions; an inner region known as Stern layer where the ions are strongly bound and an outer (diffuse) region where they are less firmly associated [46]. Within the diffuse layer there is a notional boundary inside which the ions and the particles form a stable entity. When a particle moves (e.g. due to gravity), ions within the boundary move with it. Those ions beyond the boundary stay with the bulk dispersant solution. The potential at this boundary (surface of hydrodynamic shear) is called the zeta potential (Figure 2.5).

The magnitude of zeta potential gives an indication of the potential stability of the colloidal system under study. If all the particles in suspension have a large negative or positive zeta potential then they will tend to repel each other and there will be no tendency for the particles
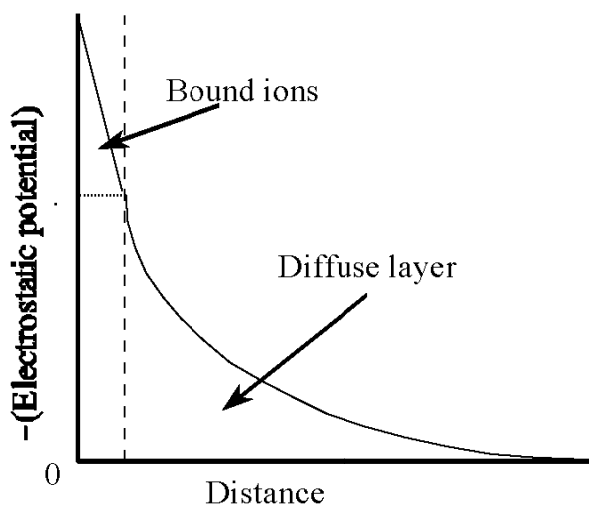
Figure 2.5 Electrostatic potential near a negatively charged spherical particle.

to come together and hence is considered a stable suspension. However, if the particles have low zeta potential values then there will be no force to prevent the particles from coming together and flocculating. The general dividing line between stable and unstable suspensions is generally taken at either +30 or -30 mV, depending on the surface charge of the particles. Particles with zeta potentials more positive than +30 mV or more negative than -30 mV are normally considered quite stable. However, if the particles have a density different form the dispersant, they will eventually sediment forming a close packed bed. The general method used to estimate the zeta potential is the electrophoresis [47]. The basic theory related to electrophoresis is introduced in the following section.

Chapter 2: Experimental methods

2.7.1 Electrophoresis

When an electric field is applied across an electrolyte solution, charged particles suspended in the electrolyte are attracted towards the electrode of opposite charge. But the viscous forces acting on the particles tend to oppose this movement. After reaching equilibrium between these two opposing forces, the particles move with constant velocity. The velocity is dependent on various factors such as the strength of the electric field or voltage gradient, the dielectric constant of the medium, the viscosity of the medium, and the zeta potential. The velocity of a particle in a unit electric field is referred the electrophoretic mobility of that particle. Zeta potential is related to the electrophoretic mobility by the Henry equation given by

$$U_E = \frac{2\varepsilon z f(\kappa a)}{3\eta}$$

(2.61)

where U_E = electrophoretic mobility, z = zeta potential, ε = dielectric constant, η = viscosity and $f(\kappa a)$ = Henry's function. The units of κ, termed the Debye length, are reciprocal length and κ^{-1} is often taken as a measure of the "thickness" of the electrical double layer. The parameter 'a' refers to the radius of the particle and therefore κa measures the ratio of the particle radius to the electrical double layer thickness. Electrophoretic determinations of zeta potential are most commonly determined in aqueous media and moderate electrolyte concentration. In this case, the value of $f(\kappa a)$ is 1.5, and this is referred to as the Smoluchowski approximation. Therefore calculation of zeta potential from the mobility is simple for systems that fit the Smoluchowski model, i.e. particles larger than about 0.2 microns dispersed in electrolytes containing more that 10^{-3} molar salt. Also, for small particles in low dielectric constant media (e.g. non-aqueous media), $f(\kappa a)$ becomes 1.0 and allows an equally simple calculation and this is referred to as the Huckel approximation [48].

Chapter 2: Experimental methods

Zeta potentials were determined with a Nanosizer Z (Malvern Instruments, Malvern, UK) by phase analysis light scattering with applied field strength of 2.5 x 10^3 V/m. The light source was He-Ne laser operated at 633 nm operating at 4.0 mW. The zetapotential values are calculated from the electrophoretic mobility data using Smoluchowsky approximation. The experiment was carried out using a quartz cuvette (universal 'dip' cell) with 10 mm light pathway. The measurements were performed at 25 ^{0}C.

2.8 Materials used

Cetyltrimethylammonium bromide (CTAB), tetradecyltrimethylammonium bromide (TTAB), decyltrimethyammonium bromide (DTAB), sodium 3-hydroxy naphthalene 2-carboxylate (SHNC), and sodium hexametaphosphate (HMP), were obtained from S. D. Fine Ltd. Mumbai (India). Sodium laurate (SL), sodium oleate (NaOL), sodium chloride (NaCl), sodium dihydrogen phosphate, disodium hydrogen phosphate, and bovine serum albumin (BSA), were procured from Sigma aldrich. Sodium 3-hydroxynaphthalene 2-carboxylate (SHNC) was obtained from M/S Atul Products, Mumbai (India). Aniline hydrochloride (AHC) and potassium peroxodisulfate (KPS) were purchased from Fluka, Germany. Progesterone standards in serum and progesterone antiserum from rabbit were obtained from ILCJ, BRIT, Mumbai (India). Solutions of biomolecules were stored in an environment at 4 °C when not in use. All chemicals were used as received without further purification. Deionized water from a Millipore-Milli-Q system (resistivity ~ 18 MΩ cm) was used to prepare all the aqueous solutions. Measurements were done at neutral pH. In case of CTAB/TTAB-SL mixed micelles experiments, the equilibration time was 24 hours at room temperature of 25 ^{0}C and for CTAB-NaOL mixed micelles experiments, equilibration time was 48 hours at room temperature of 25 ^{0}C and 30 minutes at a temperature of 50 ^{0}C.

CHAPTER 3

Mixed surfactant

systems

Chapter 3: Mixed surfactant systems

3.1 Introduction

Mixtures of cationic and anionic surfactants often display a rich variety of microstructures in aqueous solutions, governed by the molar ratio of the two components. Catanionic mixed surfactants exhibit synergistic interactions generated between oppositely charged surfactant pairs. This has stimulated extensive research interest among experimentalists as well as theoreticians [49, 50]. Complex structures such as elongated micelles, vesicles, liquid-crystalline phases, nanodisks, etc., can be formed by changing the composition of catanionic mixtures. At low surfactant concentrations, the microstructure is primarily decided by the ratio of cationic to anionic ingredients. The structural changes in such mixtures arise due to a delicate balance of the various noncovalent forces that drive the self-assembly process. In particular, the electrostatic repulsion of the charged heads localized on the micelle surface and steric repulsion due to the packing of surfactant chains get modified by the formation of catanionic pairs [51]. Hence, the addition of anionic surfactant to cationic micelles facilitates the transition from spherical to rod-like or worm-like micelles. This has been quantitatively explained in terms of the geometrical packing parameter, p, which depends on the ratio between the cross-sectional area of the hydrocarbon part and that of the head group. Low packing parameters (around 1/3) are found for single-chain surfactants with a strongly polar head group and they prefer to form spherical micelles, whereas a value close to 1/2 favors the formation of infinitely long rod-like aggregates [52, 53].

Addition of anionic surfactant to the cationic micelles leads to the formation of long, flexible worm-like micelles, vesicles, or precipitation of the catanionic salt. Though vesicle formation in catanionic mixtures have been reported, only few reports on the formation of

worm-like micelles in such mixtures are available, unless the individual surfactants themselves form worm-like micelles. This is mainly because the strong attraction between the cationic and anionic surfactants leads to the precipitation of the catanionic salt or the formation of vesicle phases that has spontaneous curvature much smaller than rod-like micelles [54-57]. With an increase in the length of worm-like micelles, micelles entangle into a transient network, which leads to viscoelastic nature to the surfactant solutions that are analogous to that of flexible polymer solutions. However, unlike ordinary polymers, worm-like micelles are in thermal equilibrium with their monomers in the bulk and the micellar chains can break and recombine reversibly on a characteristic time scale that is dependent on the system and the prevailing physicochemical conditions [58-65]. Such worm-like micelles have wide range of potential applications such as fracturing fluids in oil fields, thickening of personal care products, and drag reducing agents [66].

Recently Yuan *et al.* reported the formation of solid nanofibers of sodium laurate in the presence of sodium chloride and subsequent formation of hydrogels comprising nanofibers of sodium laurate [67]. Also, catanionic aggregates comprising cationic drugs and anionic surfactants have been investigated for controlled release of drugs [69]. Cationic drugs such as alprenolol, diphenylhydramine, lidocaine, propranolol, tetracaine, etc., can be complexed with lauric acid or capric acid to form drug-surfactant aggregates of wide ranging morphologies. These catanionic aggregates prolong the drug release from agar-agar or carbopol gels and decrease the apparent diffusion coefficient of drugs by a factor of 10 to 50. These natural fatty acids are more effective than traditional anionic surfactant, sodium dodecylsulfate in forming catanionic complexes with above drugs and the length of the hydrophobic part of the surfactant plays an important role in the formation of such

pharmaceutically important complexes. Lauric and capric acids are found in natural sources; for example, coconut oil contains approximately 50 % lauric acid [70] and it is one of the major components of mother's milk [71]. Inspite of its pharmaceutical relevance and biocompatibility, experimental data about microstructure and head group interactions in catanionic mixtures comprising lauric or capric acid is scarce. This is mainly due to their limited solubility in water at room temperature. Lin *et al.* reported that organic salts of the type tetralkylammonium bromides show an excellent ability to depress the Kraft points of sodium soaps such as sodium laurate (SL), sodium myristate, sodium palmitate, and sodium stearate due to the "salting in" effect of the electrolyte [68]. Their study is restricted to tetralkylammonium ions with alkyl chains shorter than four carbon atoms, as the solubility of such salts in water decreases with increasing alkyl chain length. However, this demonstrates a cooperative interaction between alkylammonium ions and the negatively charged sodium soaps. The solubility issue can be resolved if one uses the cationic surfactant cetyltrimethylammonium bromide (CTAB) or tetradecyltrimethylammonium bromide (TTAB) as an additive. With this motivation, the mixed self-assembly of cationic surfactant CTAB/TTAB and anionic sodium laurate in dilute aqueous solutions is investigated. Also Eastoe *et al.* investigated the effect of alkyl chain length on a series of alkyltrimethylammonium dodecylsulfates using small angle neutron scattering [72]. They showed that both axial and equatorial growth of the micelles in such catanionic mixtures are influenced by the asymmetry in the length of the alkyl chains of the constituent pairs.

The aim of this study was to understand the role of hydrophobic chain length on microstructure and intermolecular chain packing of C_nTAB–SL mixed micelles, where n = 16 (CTAB) and n=14 (TTAB). In the first section of the chapter, an investigation on the axial

and equatorial growth of CTAB/TTAB micelles in the presence of SL has been presented. Small angle neutron scattering (SANS) was used to identify the extent of elongation and cross sectional swelling (deviation from circular cross section) of rod-like micelles. It is observed that the elongation of TTAB micelles by the addition of SL is less than that is observed in CTAB micelles, while the cross sectional swelling of the micelles is higher in TTAB micelles. The second section of the chapter explains the effect of electrolyte NaCl on the growth behavior of CTAB/TTAB micelles in the presence of SL. A quantitative estimation of the electrostatic and steric contribution to the chain packing of CTAB/TTAB molecules has been identified and compared the results with the values predicted by Nagarajan [73].

3.2 Sodium Laurate induced micellar growth in CTAB/TTAB micelles

Sodium salts of naturally occurring fatty acids have limited solubility in water at room temperature due to the high Kraft points. Certain bulky inorganic salts such as tetralkylammonium bromides exhibit remarkable ability to depress the Kraft point and hence increase the soap solubility in water [68]. Among the family of natural fatty acid soaps such as sodium laurate (SL), sodium myristate, sodium palmitate and sodium stearate, sodium laurate has the lowest Kraft point. The ability of such salts to decrease the Kraft point of sodium soaps depends on the size of the alkyl chain in the tetralkylammonium ion as well. These results suggest a synergistic interaction between the quaternary ammonium ion and negatively charged head group of sodium soaps. Such synergistic interaction is highly conducive for the formation of complex supramolecular structures, even at low surfactant concentrations. Since the nature of the hydrophilic part in the cationic surfactant cetyltrimethylammonium bromide (CTAB) or tetradecyltrimethylammonium bromide

(TTAB) is similar to the tetralkylammonium salts, one would anticipate a similar interaction between the surfactants CTAB/TTAB and SL.

3.2.1 DLS studies

Firstly, the composition dependent microstructure of micelles formed by CTAB/TTAB and SL has been looked upon. Due to the very low solubility of SL in water at room temperature, focus of the study was on the cationic rich side of the binary surfactant mixture. The solubility of SL in water is enhanced in the presence of CTAB/TTAB micelles and it depends on the composition of the mixture. At a constant surfactant concentration of 0.1 M, SL gets solubilized in CTAB/TTAB micelles when the mole fraction of SL (x_{SL}) is less than around 0.35. At x_{SL} greater than 0.40, a turbid phase appears at all compositions. This behavior is different from other cationic–anionic mixtures for which a clear phase appears in both cationic and anionic rich side of the phase diagram. Since both SL and the catanionic salt are sparingly soluble in water at room temperature, the one phase region is limited to the cationic-rich side only.

Changes in the microstructure of CTAB/TTAB micelles upon addition of sodium laurate have been probed by dynamic light scattering (DLS). This technique is sensitive to the collective diffusion coefficient of the micelles. The apparent hydrodynamic radius (equivalent sphere diameter calculated using Stokes–Einstein relationship) of the micelles shows an increase with increasing mole fraction of sodium laurate in the CTAB/TTAB–SL mixed micelles, at a total surfactant concentration of 0.1 M as depicted in Figure 3.1. It can be noted that in the absence as well as at low mole fractions of sodium laurate (x_{SL}), apparent hydrodynamic radius of both CTAB–SL and TTAB–SL mixed micelles are almost same but with increasing x_{SL}, CTAB–SL micelles undergo rapid growth as compared to TTAB–SL

micelles, indicating length of the surfactant molecules plays an important role in the growth behavior of the mixed micelles. For CTAB/TTAB–SL micelles, at low x_{SL}, equivalent sphere radius is consistent with the value that is expected for small globular micelles. However, as x_{SL} increases, the equivalent sphere diameter of the micelles increases and it reaches a value inconsistent with the alkyl chain length of the surfactant. This clearly suggests the growth of
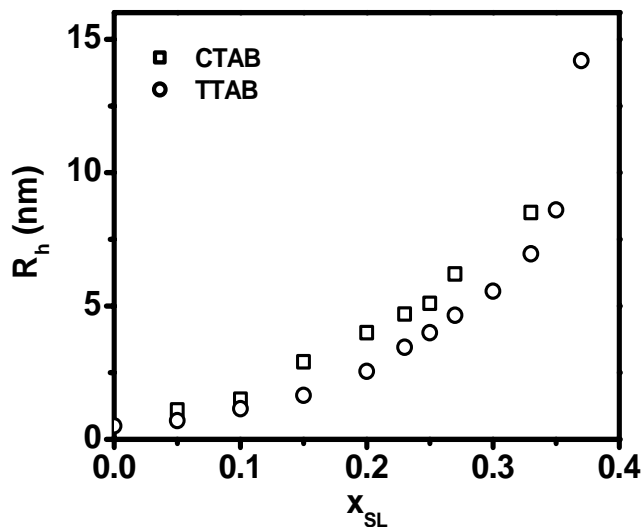
Figure 3.1 Variation of apparent hydrodynamic radius of CTAB/TTAB–SL mixed micelles (total surfactant concentration, $C_T = 0.1$ M) at different mole fractions of sodium laurate, x_{SL}.

the globular micelles to form anisotropic aggregates. Two alternate possibilities for the growth of globular micelles are either as disk-like (oblate) micelles or rod-like (prolate) micelles. As opposed to disk-like micelles, rod-like micellar growth leads to dramatic changes in the viscosity of the fluid upon structural transition. Indeed, the composition dependant rheological behavior of the fluid, which will be discussed later, indicates a rod-like micellar growth.

An attempt has been made to relate apparent diffusion coefficient D_a to the average length L of the rods. To extract information about the size of the micelles from D_a, the effect of interactions between neighboring micelles must be taken into account. The apparent diffusion coefficient D_a can be related to the diffusion coefficient D_0 at infinite dilution by

$$D_a = D_0[1 + k_D(c - cmc)] \tag{3.1}$$

where k_D is the diffusion virial coefficient, c is the surfactant concentration and k_D can be expressed as a competition between an osmotic pressure term that enhances the diffusion and a retarding hydrodynamic frictional term [74]. Thus

$$k_D = (2MB_2 - k_f - \bar{v}) \tag{3.2}$$

where M is the molecular weight of micelle, B_2 is the osmotic second virial coefficient, k_f is the hydrodynamic friction virial coefficient and $\bar{v}$ is the specific volume of the micelle. For a rigid rod, B_2 is given by [75]

$$B_2 = \left(\pi N_a d^2 L \big/ M^2 \right) f \tag{3.3}$$

where N_a is Avogadro's number, d is the diameter, L is the length of the rod, and

$$f = \frac{1}{4}\left[1 + \frac{L}{d}\left(1 + \frac{d}{2L} \right)\left(1 + \frac{\pi d}{2L} \right) \right] \tag{3.4}$$

The hydrodynamic friction virial coefficient k_f for suspensions of uncharged rods is given by [76]

$$k_f = \left(\frac{RT}{3\eta} \right)\left(\frac{L^2}{D_0 M} \right)\left(\frac{3d}{8L} \right)^{2/3} \tag{3.5}$$

Finally, the diffusion coefficient D_0 can be related to the length of the rod and its axial ratio $\frac{L}{d}$ by Broersma's relationship [77]:

$$D_0 = \frac{k\,T}{3\pi\eta L}\left[\ln \frac{L}{d} + \zeta \right] \tag{3.6}$$

where k is Boltzmann's constant, T the absolute temperature, η the solvent viscosity, and ζ the shape factor which is a function of axial ratio L/d. In the case of micellar solutions at low volume fractions, the effect of interparticle interactions can be neglected and D_a can be approximated to D_0. The expressions of Tirado *et al.*, which are valid for axial ratios in the range of 4 – 30, relate ζ to (L/d) [78]:

$$\zeta = 0.312 + 0.5656/(L/d) - 0.05/(L/d)^2 \qquad (3.7)$$

As it is impossible to calculate both d and L from the translational diffusion coefficient alone, it is logical to fix the diameter of the rod-like micelle as twice the length of the hydrocarbon chain of the surfactant. With this approximation, using the above relationship, one can calculate the length of the micelles from D_a. Such an analysis suggests that the length of the CTAB–SL micelles varies from a few nanometers to about 50 nm, as x_{SL} varies from 0 to 0.33 and the length of TTAB–SL micelles varies from few nanometers to about 100 nm, as x_{SL} varies from 0 to 0.37 (Figure 3.2).
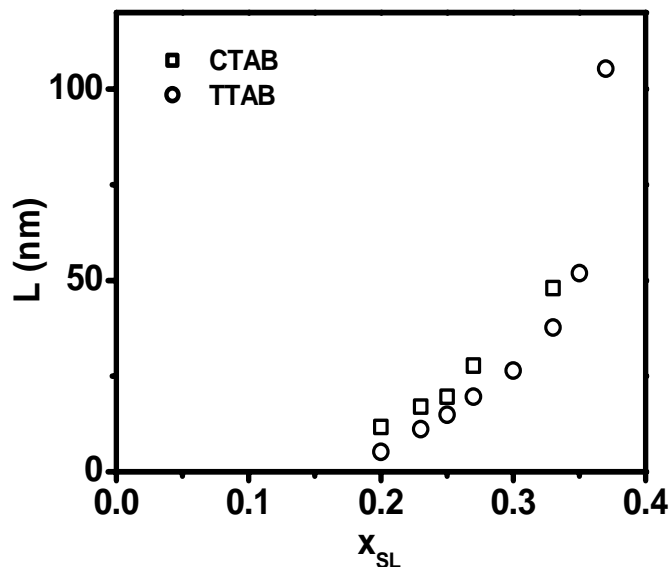
Figure 3.2 Average length (L) of the mixed micelles as a function of the mole fraction (x_{SL}) of sodium laurate ($C_T = 0.1$ M).

At small x_{SL} values, D_a could not be analysed using the above relationship for both the mixed micellar systems, suggesting that the axial ratio is smaller than 4.

3.2.1.1 Effect of steric repulsion of surfactant chain on micellar packing parameter

Now, an attempt has been made to model the observed structural transition in terms of the changes in the packing of the surfactant molecules within the aggregate. The electrostatic repulsion of the charges on the head groups as well as the steric repulsion of the tails can influence the optimum packing of the surfactant molecules. As already discussed, the geometrical packing parameter depends on the ratio between the cross-sectional area of the hydrocarbon part and that of the head group. Low packing parameters (around 1/3) are found for single-chain surfactants with a strongly polar head group and it prefers to form spherical micelles, whereas a value close to 1/2 favors the formation of infinitely long rod-like aggregates. The changes in the packing parameter in a mixture of CTAB/TTAB and SL can be envisaged if one considers the formation of a cationic-anionic ion-pair. The reduced electrostatic repulsion in such an ion-pair will increase the packing parameter as compared to that of single chain amphiphiles. From the known relations for the total volume and surface area of a rod-like micelle, comprising a cylindrical body of length (*L-d*) and two hemispherical end-caps of radius $d/2$ as drawn in Figure 3.3, the effective packing parameter of rod-like micelle (p_{rod}) can be derived as follows,

Volume of the rod (V_{rod}) can be written as

$$V_{rod} = \left(\pi \left(\frac{d}{2} \right)^2 (L - d) \right) + \left(\frac{4}{3} \pi \left(\frac{d}{2} \right)^3 \right) \tag{3.8}$$

$$= \frac{\pi d^2 (L - d)}{4} + \frac{\pi d^3}{6} \tag{3.9}$$
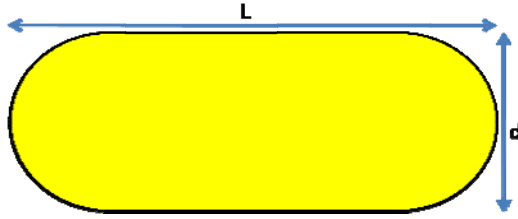
Figure 3.3 Schematic diagram of a rod-like micelle with hemispherical endcaps, having length L and diameter d.

Surface area of the rod (A_{rod}) can be given as

$$A_{rod} = \left\{ \left[2\pi \left(\frac{d}{2} \right)(L-d) \right] + \left[4\pi \left(\frac{d}{2} \right)^2 \right] \right\} \tag{3.10}$$

$$= \pi d(L-d) + \pi d^2 \tag{3.11}$$

Therefore, packing parameter of the rod (p_{rod}) can be derived as follows

$$p_{rod} = \frac{V_{rod}}{A_{rod} * d/2} = \frac{3L-d}{6L} \tag{3.12}$$

Such hemispherical end-caps are energetically favorable for rod-like micelles as it avoids the unfavorable contact of water and hydrocarbon chains at the two ends of the rods and hence a realistic model to assess the sphere to rod transition. Moreover, in the limit of $L=d$, the cylindrical body disappears and it becomes a spherical micelle with diameter d. Thus, the average p for such a micelle, computed using equation 3.12, varies from $p_{rod}=1/3$ when L is equal to d and $p_{rod} = \frac{1}{2}$ when L is infinity. Since the length of the micelle varies with the addition of sodium laurate, the effective packing parameter of the micelles and its variation with the mole fraction of the additive can be computed using equation 3.12. The effective p_{rod}, obtained in this way can be approximated as the weighted sum of the packing parameter of ion-pairs and free surfactants. With the assumption that when $x_{SL} < 0.5$, the added laurate ions

complexes with an equal number of CTAB/TTAB molecules, the mole fraction of positively

charged free CTAB/TTAB (x_1) and neutral ion-pair (x_2) can be written as

$$x_1 = \frac{1 - 2x_{SL}}{1 - x_{SL}} \tag{3.13}$$

$$x_2 = \frac{x_{SL}}{1 - x_{SL}} \tag{3.14}$$

If p_1 represents the packing parameter of free surfactant and p_2 represents the packing

parameter of the ion-pair, the effective packing parameter of the mixture can be obtained as

$$p_{rod} = \frac{1 - 2x_{SL}}{1 - x_{SL}} p_1 + \frac{x_{SL}}{1 - x_{SL}} p_2 \tag{3.15}$$

Henceforth, the free CTA^+/ TTA^+ is designated as unimer while the ion-pair CTA^+L^-/

TTA^+L^- is designated as dimer. p_2 can be related to the effective area a_2 occupied by the

dimer species, knowing the volume V_2 and the length l_2 of the dimer. The volume V_2 can be

taken as the sum of the volumes of CTA^+ / TTA^+ and L^- ions, i.e. 730 Å^3 for CTA^+L^- and 674

Å^3 for TTA^+L^- while the length l_2 can be equated to the longer of the two surfactants i.e. 22 Å

for CTA^+L^- and 18 Å for TTA^+L^-. This gives the ratio V_2/l_2 for the dimer as 35.5 Å^2

(CTA^+L^-) and 37.5 Å^2 (TTA^+L^-). With this value of V_2/l_2 and taking p_1 as 1/3 (since the

unimers are expected to form spherical micelles), from equations 3.12 and 3.15, the effective

head group area of the dimer a_2 can be estimated as a function of x_{SL} and are depicted in

Figures 3.4 (A) and 3.4 (B) for CTAB–SL and TTAB–SL mixed micelles respectively.

Surprisingly, in both the mixed micellar systems, the estimated head group area of the dimer

a_2 does not remain constant at different x_{SL} instead it increases non-linearly with x_{SL}. This

non-linear variation in the head group area can be explained if we consider that the dimer-

dimer interaction is different from the dimer-unimer interaction. The increase in a_2 with increase in dimer fraction indicates more repulsive interaction between two dimers as compared to dimer-monomer interaction. Since the dimer is practically neutral, as it is formed by ion pairing, this repulsion arrives from the steric forces of the bulky double-chains associated to the dimers. This can be conveniently modeled if we consider the number of dimer-dimer interaction possible in a lattice of randomly arranged monomers and dimers.

If x_2 represents the mole fraction of dimer in a micelle, the number of dimers in the micelles is proportional to x_2 and the probability to find another dimer nearest to a dimer is again proportional to x_2. Thus, the dimer-dimer interaction in a micelle is proportional to x_2^2.

Since $x_2 = \dfrac{x_{SL}}{1 - x_{SL}}$, by incorporating the dimer-dimer interaction term in the effective area, we can write the x_{SL}-dependence of head group area a_2 as,

$$a_2 = a_{2_0} + k_1 \frac{x_{SL}{}^2}{(1 - x_{SL})^2} \tag{3.16}$$

where a_{2_0} is the area occupied by the dimer in the absence of any dimer-dimer interaction and k_1 is a constant that depends on the dimer-dimer interaction. k_1 is positive when dimer-dimer interaction is repulsive leading to an increase in the effective area and is negative if the dimer-dimer interaction is attractive. In the limit of $x_{SL} \rightarrow 0$, the second term in equation 3.16 vanishes and effective area represents the interfacial area of the dimer when it is surrounded by unimers only. In the opposite limit of $x_{SL} \rightarrow 0.5$, all surfactant molecules exist as ion-pairs and the dimer is surrounded by dimers alone without any extra unimers. A reasonably good fit to the variation of interfacial area of the dimer with the mole fraction of SL (x_{SL}) is obtained using equation 3.16. This gives the interfacial area of the free dimer a_{2_0} as 44 Å^2 for

CTAB–SL mixed micelles and with the addition of SL it increases to a value of 55.5 Å^2 at x_{SL} equal to 0.33 and in the case of TTAB–SL mixed micelles, interfacial area of the free dimer a_{2_0} is found out to be 48 Å^2 and with the addition of SL it increases to a value of 62 Å^2 at x_{SL} equal to 0.37. It means that the steric repulsion of the chains in the dimer increases with an increase in the mole fraction of the dimer. This reflects the role of steric repulsion of surfactant chains in deciding the packing of the molecules, in addition to the electrostatic effects.

(A)   **(B)**
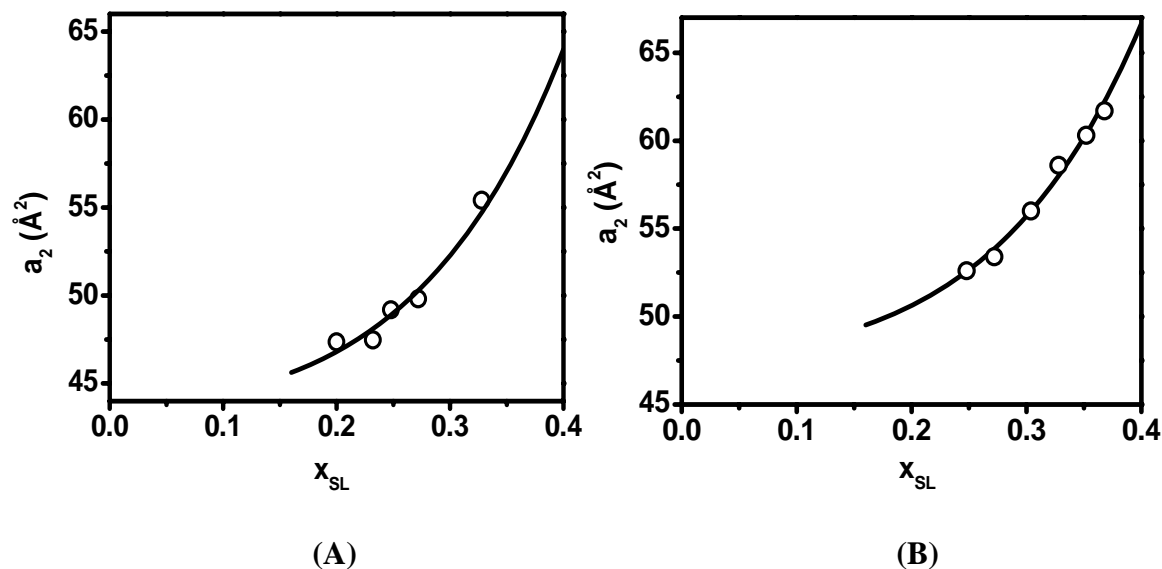
Figure 3.4 Effective head group area per molecule of ion-pair (a$_2$) in (A) CTAB–SL mixtures and (B) TTAB-SL mixtures as a function of the mole fraction (x_{SL}) of sodium laurate (C$_T$ = 0.1 M). The solid lines are the fit to the data using equation 3.16.

Though rod-like micelles have been reported in other cationic-anionic mixtures, such microstructural changes through enhanced solubilization of the surfactant are scarce. For example, aqueous mixtures of highly soluble surfactants SDS and DTAB do form rod-like micelles and vesicles, the axial ratio of the micelles are not very large [55]. This is because of

the strong association between the two surfactants to form vesicles or insoluble precipitates. The binding of tetralkylammonium ions to alkylcarboxylate surfactants has wide implications in the phase behavior of the surfactants. Clouding and phase separation upon heating, that are generally observed in nonionic surfactants, have been shown to occur in tetrabutylammonium perfluoroalkanoates, mixtures of sodium perfluorooctanoate and tetrapropylammonium bromide and mixtures of sodium alkylsulfates and tetrabutylammonium or tetrapentylammonium salts [79-85]. The phase separation is explained in terms of the crowding of the large TBA ions around the micelles and also to be due to the capacity of the TBA ions to self associate in water into ill-defined aggregates [86-91].

3.2.2 SANS studies

The sphere to rod transition observed by the addition of SL to CTAB/TTAB micelles can be verified from SANS measurements as well. CTAB/TTAB–SL mixtures form short ellipsoidal micelles at ambient conditions and the length of which could be suitably controlled by tuning the mole fraction of SL. Figures 3.5 and 3.6 show the SANS spectra obtained from CTAB–SL and TTAB–SL mixed micelles respectively at different x_{SL}, keeping the total surfactant concentration constant at 0.1 M. For both the mixed micellar systems, in the absence of sodium laurate, the spectrum shows a characteristic correlation peak at intermediate q value. This indicates the presence of repulsive intermicellar interaction between the positively charged CTAB/TTAB micelles. With increasing x_{SL}, there is a shift in the peak position to lower q values and an increase in the low q scattering intensity. These features are characteristic of a structural transition from globular to rod-like micelles. Also the correlation peak in the spectrum of both the micellar systems shows a broadening with increasing mole fraction of sodium laurate, suggesting a decrease in the electrostatic

63
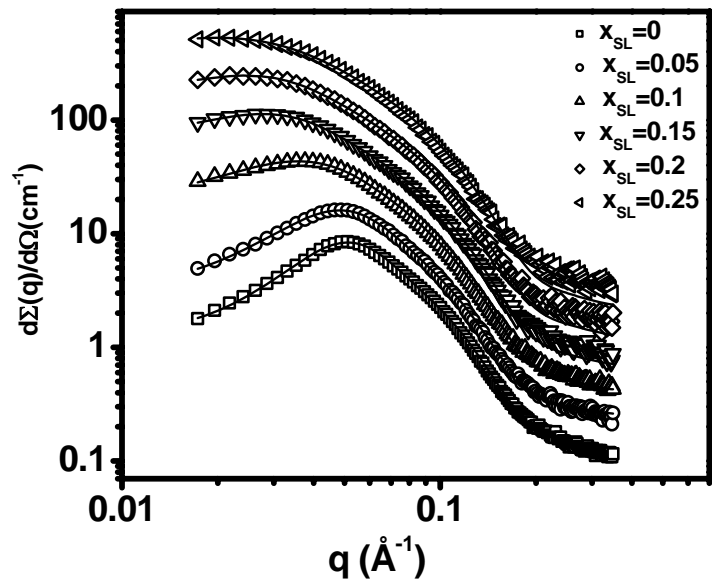
Figure 3.5 SANS spectra for CTAB–SL mixtures (C_T = 0.1 M) at different mole fractions of sodium laurate. The data for x_{SL}=0 are absolute values while the remaining plots are offset by a factor of 2 for clarity. The solid lines are fit to the data using a model for charged ellipsoids, as discussed in the text.
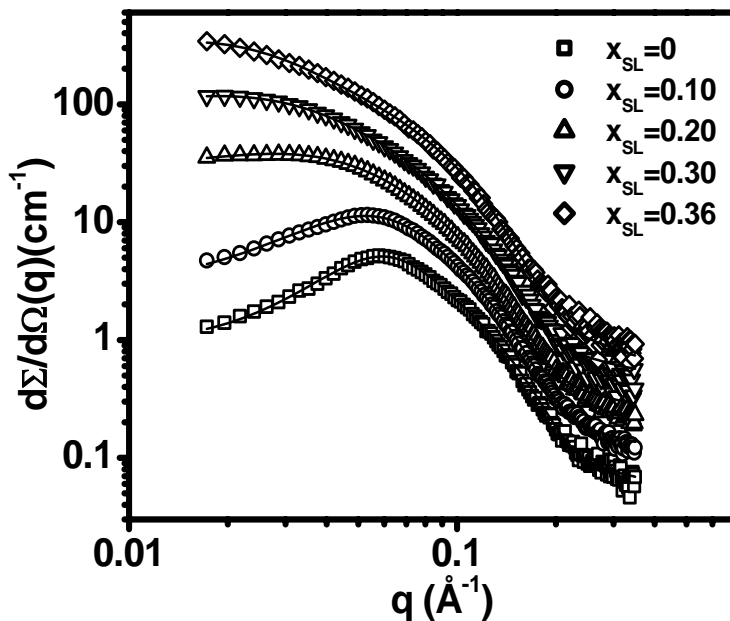
Figure 3.6 SANS spectra for TTAB–SL mixtures (C_T = 0.1 M) at different mole fractions of sodium laurate. The data for x_{SL} = 0 are absolute values while the remaining plots are offset by a factor of 2 for clarity (solid lines show the fits to the data).

interactions between the micelles. This observation indicates a synergistic interaction between the cationic and anionic surfactants in the mixed micelles. Quantitative estimates of aggregate morphology can be obtained from model fitting the SANS spectra using plausible models. Previous reports suggest that the SANS spectrum of CTAB/TTAB micelles can be modeled as charged prolate ellipsoids interacting through a screened Coulomb potential [92]. Thus, the data were analysed by this model for which the differential scattering cross section per unit volume $(d\Sigma/d\Omega)$ as a function of scattering vector q, can be written as

$$\frac{d\Sigma}{d\Omega} = n(\rho_m - \rho_s)^2 V^2 [< F(q)^2 > + < F(q) >^2 (S(q) - 1)] + B \qquad (3.19)$$

where n denotes the number density of micelles, ρ_m and ρ_s are the scattering length densities of the micelle and the solvent, respectively, and V is the micelle volume. $F(q)$ is the single particle form factor and $S(q)$ is the interparticle structure factor. B is a constant term, which represents the incoherent scattering background. $F(q)$ is calculated using the relation:

$$F(q, \mu) = \frac{3(\sin x - x \cos x)}{x^3} \qquad (3.20)$$

$$x = q[a^2 \mu^2 + b^2 (1 - \mu^2)]^{1/2} \qquad (3.21)$$

where a and b are the semimajor and semiminor axis of an ellipsoidal micelle, respectively, and μ is the cosine of the angle between the directions of a and wave vector transfer q. The interparticle structure factor $S(q)$ has been calculated using expressions derived by Hayter and Penfold from the Ornstein–Zernike equation and using the rescaled mean spherical approximation. In this approximation micelles are assumed to be rigid equivalent spheres of diameter $\sigma = 2(ab^2)^{1/3}$ interacting through a screened Coulomb potential, which is given by

$$u(r) = u_0 \frac{\sigma}{r} exp[-\kappa(r - \sigma)], \qquad\qquad r > \sigma \qquad (3.22)$$

Where u_0 is the contact potential, κ the Debye-Huckel inverse screening length which depends on the CMC, fractional charge on the micelles and the concentration of the added electrolyte. The fractional charge α (= z/N, where z is the micellar charge and N the aggregation number of the micelles) is an dditional parameter in the calculation of S(Q).

Due to the limited q-range of the instrument, SANS measurements are sensitive to the structural changes of these micelles at small axial ratios. For data fitting of CTAB–SL mixed micellar system, the semiminor axis of the ellipsoid is fixed as 22 Å^2, as estimated from the length of the surfactant chain. The fractional charge on the micelle and semimajor axis are used as variables in the fit and for data fitting of TTAB–SL mixed micellar system, fractional charge, semiminor axis, and semimajor axis are used as the variables in the fit. In order to obtain good fit for both the systems, a polydispersity in the semimajor axis is necessary and is included using Schultz distribution [93]. In all samples, a polydispersity parameter $z = 35$ was used in the semimajor axis. The aggregation number was calculated from the relation $N = 4\pi ab^2/3v$, where v is the surfactant monomer volume, which has been estimated using Tanford formula. The experimental data fits well with the model and the parameters of the fit are summarized in Tables 3.1 and 3.2 for CTAB–SL and TTAB–SL mixed micellar systems respectively. Consistent with the DLS results for both CTAB–SL and TTAB–SL mixed micelles, the axial ratio of the micelles increases with increase in x_{SL}. The semimajor axis of CTAB/TTAB–SL mixed micelles becomes very large at high x_{SL}, leading to the formation of long flexible micelles. The surface charge of the micelles decreased to a neutral value at high x_{SL}. The association of sodium laurate and CTAB/TTAB, which are oppositely charged, leads to neutralization of the electrostatic charges on the micellar surface. In the case of TTAB–SL system, it was observed that the semiminor axis also increases with an increase

Table 3.1 Micellar parameters obtained from the SANS analysis of 0.1 M CTAB–SL mixed micelles at different mole fractions of sodium laurate.

S.No.	Mole fraction of Sodium laurate (x_{SL})	Aggregation number (N_{agg})	Fractional charge (α)	Semimajor axis, a (Å)	Axial ratio
1	0	157	0.14	47.0	2.1
2	0.05	178	0.09	52.0	2.4
3	0.1	306	0.03	87.7	4.0
4	0.15	618	0.02	173.6	7.9
5	0.2	756	0.02	207.8	9.4
6	0.25	881	0.01	237.0	10.8

Table 3.2 Micellar parameters obtained from the SANS analysis of 0.1 M TTAB–SL mixed micelles at different mole fractions of sodium laurate.

S.No.	Mole fraction of Sodium laurate (x_{SL})	Aggregation number (N_{agg})	Fractional charge (α)	Semiminor axis, b (Å)	Semi major axis, a (Å)	Axial ratio	Cross-sectional radii, Rcs (Å)
1	0	99	0.15	18.1	40.2	2.21	17.4
2	0.1	126	0.07	19.5	42.9	2.20	18.7
3	0.2	221	0.01	21.0	62.2	2.96	19.4
4	0.3	435	0.01	21.9	108.8	4.97	20.2
5	0.36	1698	0.01	21.0	449.2	21.36	21.3

in x_{SL}. This indicates that the TTAB micelles undergo both swelling and elongation upon addition of SL.

When a comparison study of the micellar parameters of TTAB–SL mixed micelles to that of CTAB–SL micelles has been done, it was observed that at a given x_{SL}, elongation of the micelles is more pronounced in CTAB micelles than in TTAB micelles. The semiminor axis of CTAB micelles did not show appreciable changes with the addition of SL while TTAB

micelles showed a progressive increase in the semiminor axis. Having found that TTAB micelles undergo swelling with the addition of SL, further analysis of SANS data in the intermediate q-range using the cross sectional Guinier analysis to obtain cross section radius of gyration of rod-like aggregates has been done. According to Porod, for a random distribution of rod-like particles, the scattering intensity in the intermediate q range follows the relation: [94, 95]

$$q.I(q) = K \exp(-q^2 R_{G,CS}{}^2)/2 \qquad (3.23)$$

where $R_{G,CS}$ is the weight-average radius of gyration of the cross section of the cylinder and K is a constant that depends on the sum of the neutron scattering lengths and volume per surfactant monomer in the micelles and the scattering length density of the solvent.

For a circular cross section, the micellar radius is given by

$$R_{cs} = \sqrt{2}.R_{G,CS} \qquad (3.24)$$

Using equations 3.23 and 3.24, cross section radii (R_{cs}) for the TTAB–SL mixed micelles at different mole fractions of sodium laurate was calculated from the slope of $\ln(I(q).q)$ versus q^2 graph as shown in Figure 3.7. It is worth mentioning that the position of the maximum intensity in the cross sectional Guinier plot shifts to lower q values with increasing x_{SL}, indicating an increase in the length of the micelles. The slope of the plot increases with an increase in the mole fraction of sodium laurate, indicating that the micelles are growing equatorially also as observed from the model fits.

A similar analysis has been done with the SANS spectra obtained for CTAB–SL mixed micelles. The variation in the cross sectional radii of the ellipsoidal micelles formed by CTAB and TTAB with the addition of SL, as obtained from the cross sectional Guinier

analysis are depicted in Figure 3.8. It is found that the R_{cs} of CTAB micelles vary marginally

(from 21 Å to 22.5 Å) while that of TTAB micelles varies from 17.5 Å to 21.5 Å with an
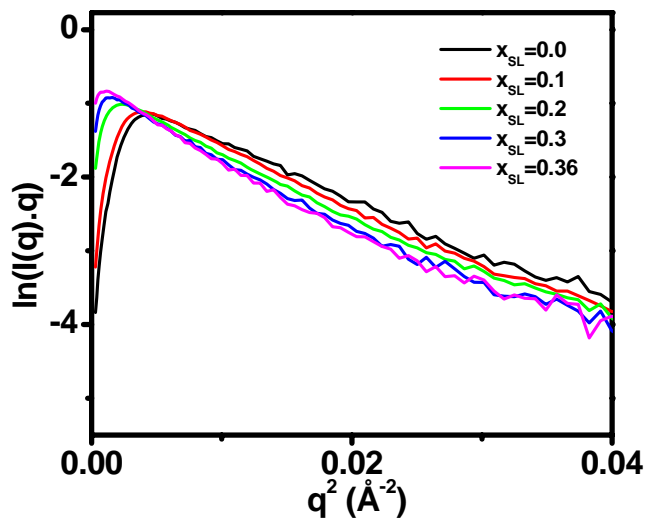
Figure 3.7 Guinier-like plot of the SANS data in the low-q region for TTAB–SL mixtures (C_T = 0.1 M) at different mole fractions of sodium laurate.
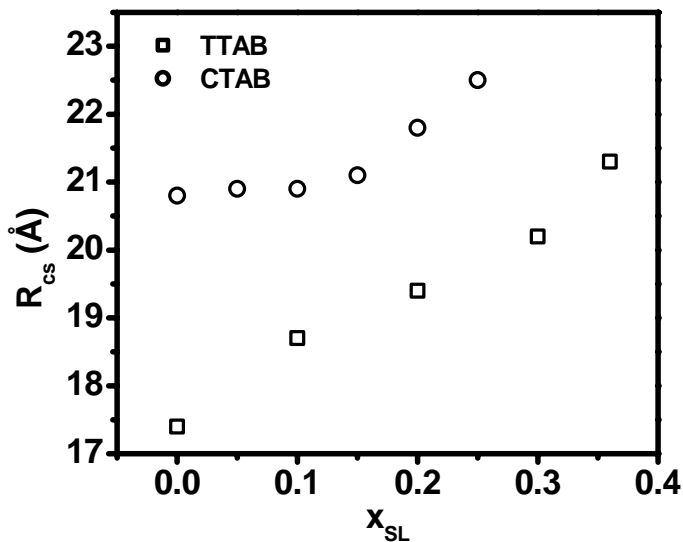
Figure 3.8 Variation in the cross section radius (R_{cs}) for the C_nTAB–SL mixtures (C_T = 0.1 M) at different mole fractions of sodium laurate.

increase in x_{SL}. The cross sectional radius calculated from the Guinier analysis, assuming a circular cross section, is consistent with the value obtained from model fitting. However, the swelling or increase in the cross sectional Rg can be well understood in terms of deviation from circular cross section of the micelles to elliptical cross section. This is due to the fact that increase in circular cross section from a value larger than the extended length of surfactant chain is energetically unfavorable. A schematic representation is shown in Figure 3.9.
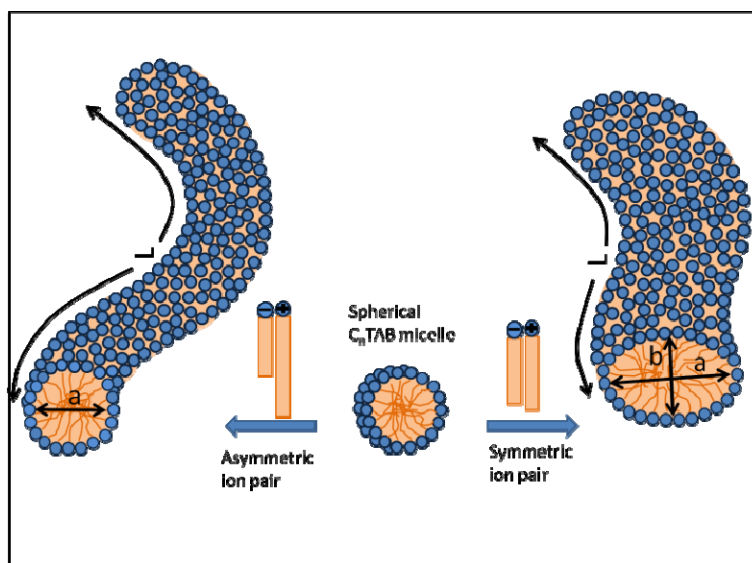
Figure 3.9 Schematic representation of the elongated micelles formed by CTAB-SL and TTAB-SL mixtures (*a* and *b* are the cross sectional axes and *L* is the length of the rod-like micelle).

Our results are consistent with the reports that nanodisks or ribbon like micelles are formed when the surfactant composition is sufficiently balanced to allow significant reduction in curvature [96]. Phase behavior and microstructural changes in mixtures of DTAB and SL has been reported by Yin *et al.* recently [97]. Depending on the mixing ratios, vesicular and lamellar phases were observed. At a total surfactant concentration of 80 mM, when the

mixing ratio deviates from the equimolar line greatly (SL: DTAB ratio 1:3), spherical micelles are the preferred aggregates. As the mixing ratio approaches equimolar line, spherical micelles grow and large vesicular aggregates form at a SL: DTAB ratio of 1:1.3. Further increase in the SL content leads to associative phase separation of the mixture to form two coexisting liquid phases. DLS studies showed that by small changes in composition, in the absence of any electrolytes, DTAB micelles transform to large vesicles and no viscoelastic phases were observed. This is different from what is observed from mixtures of SL and CTAB where long polymer-like micelles are formed over a wide range of composition. This suggests that minute changes in the structure of additives alter the phase behavior significantly. Eastoe *et al.* studied the effect of chain length on the axial and equatorial growth of the micelles for a series of alkyltrimethylammonium dodecylsulfates using small angle neutron scattering. For alkyl chain length comprising 3-4 carbon atoms (m = 3-4), the micelles were found to be predominantly cylindrical, whereas for m = 6-7, disk-shaped ones were formed [72]. It was observed that when the asymmetry between the chain length of surfactants is more, formation of cylindrical micelles are favored whereas when the asymmetry is less, disk shaped mixed micelles are formed. If one compares the chain lengths in TTAB–SL mixture with that of CTAB–SL, the difference in the chain length of the two components is less in TTAB–SL. This will favor the formation of disk-like micelles as opposed to rods. Thus, the equatorial growth of the micelles will be more favorable in TTAB–SL mixtures as compared to CTAB–SL mixtures. At x_{SL} = 0 and 0.1, the presence of intermicellar interaction can affect the cross sectional Guinier analysis, though the effect is marginal at intermediate q-range. However, at low surfactant concentrations, the effect of such intermicellar interactions can be minimized by the addition of electrolytes such as NaCl.

3.2.3 Rheological studies

Microstructural changes associated with binding of oppositely charged surfactants impart changes in macroscopic transport properties of the fluid as well. Rheological measurements were done on the CTAB/TTAB–SL mixed micelles containing different x_{SL}, at a total surfactant concentration of 0.1 M. Figures 3.10 and 3.11 show the data from linear rheological measurements for CTAB–SL and TTAB–SL mixed micelles systems respectively. For both the systems, a Newtonian plateau at low shear rates was observed for all the samples but a shear thinning behavior was observed at high shear rates for the samples containing high x_{SL}.
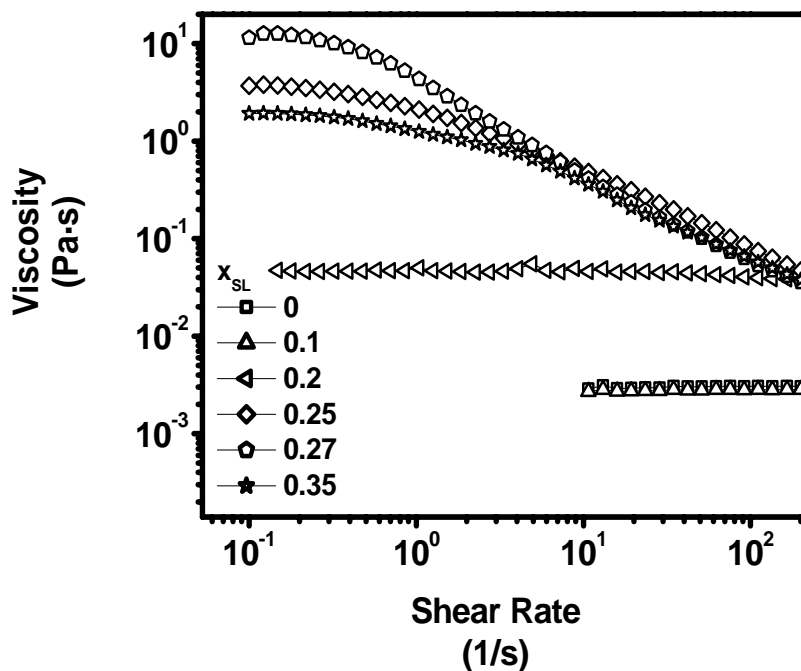
Figure 3.10 Viscosity, η, of CTAB–SL mixtures (C_T = 0.1 M) as a function of shear rate at different mole fractions of sodium laurate.

Figure 3.12 compares the zero-shear viscosities (plateau viscosities) of TTAB–SL mixed micelles with that of CTAB–SL mixed micelles at different x_{SL}. At low x_{SL}, zero shear
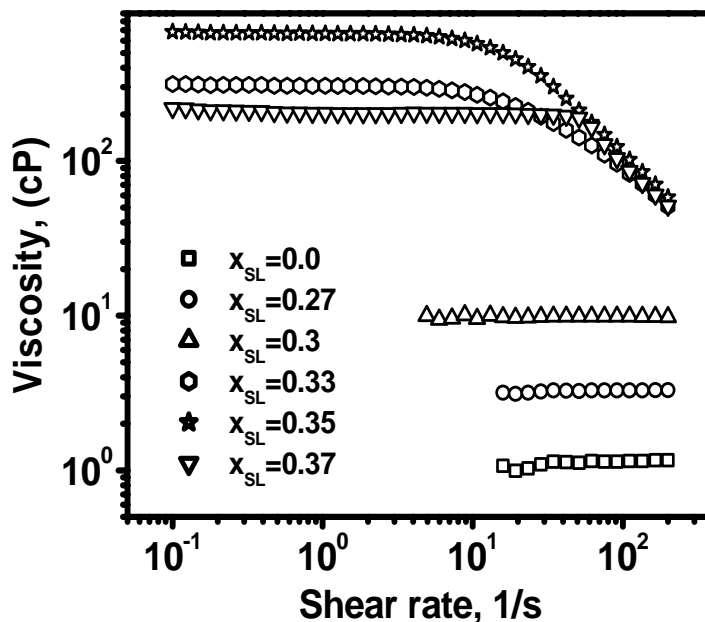
Figure 3.11 Viscosity, η, of TTAB–SL mixtures ($C_T = 0.1$ M) as a function of shear rate at different mole fractions of sodium laurate.

viscosities of CTAB/TTAB–SL mixtures are comparable to that of water and it increases slowly at low x_{SL} and rapidly at higher values of x_{SL}. It reaches a peak viscosity value and then decreases again. In the case of CTAB–SL mixed micelles, the maximum is around x_{SL} equal to 0.27 and in TTAB–SL mixed micelles, the maximum is around x_{SL} equal to 0.35. The peak viscosity is about 4 orders of magnitude higher than that of pure surfactant solution, suggesting the formation of long flexible micelles. The rapid increase in the viscosity can be attributed to the micellar growth from nearly globular to elongated micelles. The micelles eventually develop into long, flexible micelles, owing to which the system exhibits shear thinning behavior. This behavior is similar to that reported for other worm-like micellar fluids containing surfactants and hydrotropes [98, 99]. The occurrence of maxima in viscosity is generally attributed to the formation of branched micelles [100]. At a given volume fraction, the viscosity of branched micelles are lower than that of linear micelles, as the branch points

can slide along the length of the micelles, providing an additional mechanism for stress relaxation. Such branching occurs in worm-like micelles when the electrostatic interactions are sufficiently screened such that the energy of branch points is lower than the end-cap energy. Entanglement of such long flexible micelles can impart viscoelasticity to the fluid.
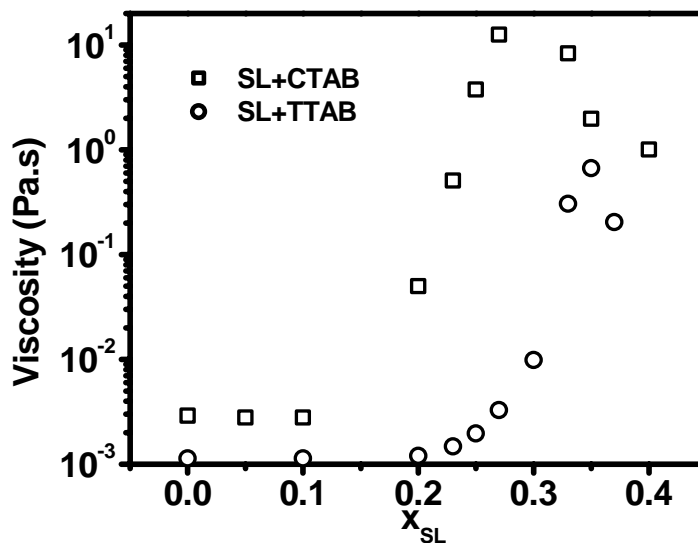
Figure 3.12 Variation of the zero-shear viscosity, η_0, of TTAB–SL and CTAB–SL mixed micelles with mole fraction of sodium laurate ($C_T = 0.1$ M).

To assess the viscoelastic behavior, dynamic rheological studies were performed on selected samples near the viscosity maximum. Figure 3.13 shows the frequency dependant shear moduli (storage modulus and loss modulus) of a representative sample containing 70/30 mixture of CTAB–SL and Figure 3.14 shows the variation of G' and G'', in the form of Cole-Cole plot for the same. At low frequencies, the behavior is similar to that one expects for a typical viscoelastic fluid (Maxwellian behavior). As already discussed for a Maxwell fluid, the storage modulus G' and loss modulus G'' varies with frequency as,

$$G'(\omega) = \frac{(\omega\tau_R)^2}{1+(\omega\tau_R)^2}G_0$$

74

and $G''(\omega) = \dfrac{\omega \tau_R}{1 + (\omega \tau_R)^2} G_0$

where G_0 is the plateau modulus and τ_R is the characteristic relaxation time. At high frequencies, the spectrum shows deviations from the Maxwellian behavior. Such deviations can arise from various factors. As micelles are in dynamic equilibrium with monomers, they undergo reversible breakage and recombination at a time scale shorter than the reptation time of the long micelles. Competition between reptation and breakage of micelles influences the high frequency behavior of dynamic rheology [101]. In addition, polydispersity in micellar length and contributions from Rouse mode or breathing mode of the chains can cause an upturn in the loss modulus at high frequencies. The model of Granek and Cates that takes into account the short time dynamics of polymers clearly captures the high frequency
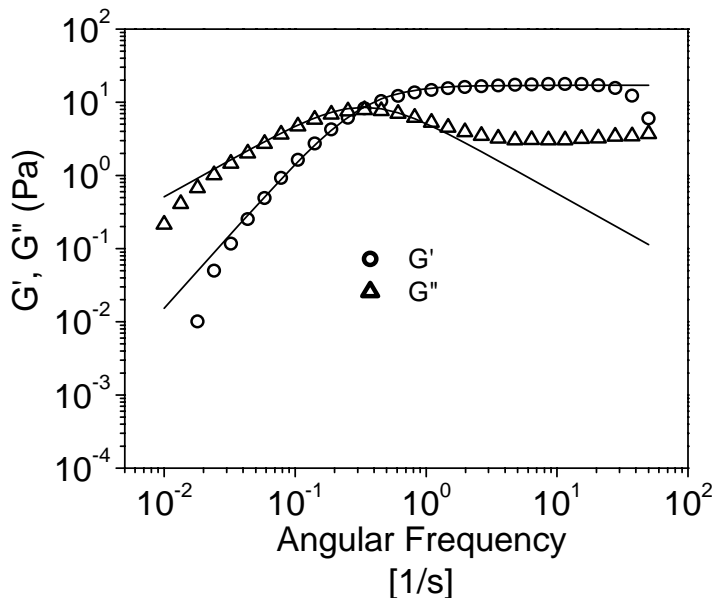
Figure 3.13 Variation of the storage modulus (G') and loss modulus (G'') as a function of angular frequency (ω) at 25°C, for a CTAB–SL mixture. The mole fraction of SL (x_{SL}) is 0.30, and the total surfactant concentration is 0.1 M. The solid lines are fit to the low frequency data using Maxwell model.
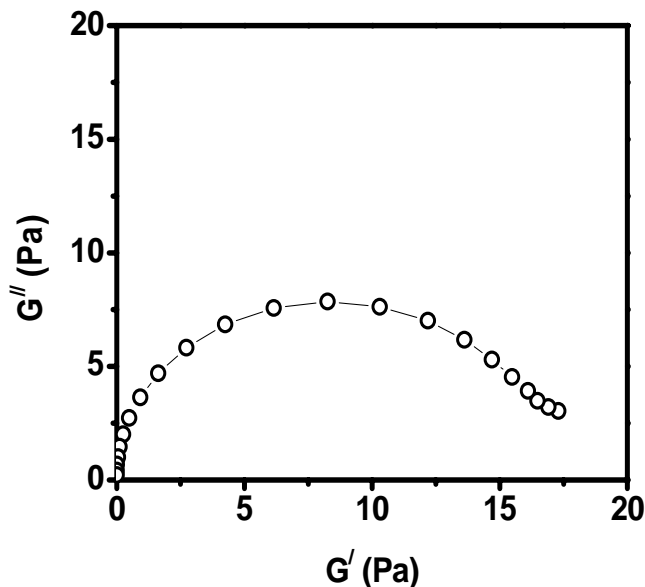
Figure 3.14 Variation of the loss modulus (G") as a function of storage modulus (G') for CTAB–SL mixed micelles at $x_{SL} = 0.3$ ($C_T = 0.1$ M).

behavior [101]. The dynamic rheology of CTAB/TTAB–SL mixtures that exhibit a shear thinning behavior clearly shows viscoelastic nature of the fluid, much like entangled polymer solutions. Figure 3.15 shows photographs of pure 30 mM SL solution and 30 mM SL in presence of 70 mM CTAB, showing the viscoelastic nature of the mixed surfactant solution.

30mM sodium laurate

(Turbid)

30mM sodium laurate + 70mM CTAB

(Clear and viscoelastic)
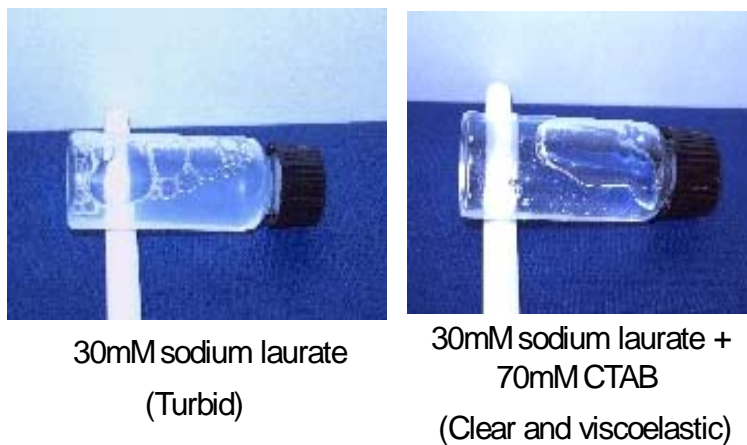
Figure 3.15 Photographs of samples containing pure 30 mM SL and 30 mM SL in presence of 70 mM CTAB.

As depicted in Figure 3.12, the position of the maximum is different for CTAB–SL and TTAB–SL mixtures. The viscosity maximum is at lower mole fraction of sodium laurate for CTAB–SL mixture compared to TTAB–SL mixture, indicating that elongation is more for CTAB–SL mixture. Therefore, the length of the hydrocarbon chain plays an important role in inducing axial growth of the mixed micelles. It appears that subtle changes in the hydrophobic tail of individual components in a catanionic mixture can determine the extent of swelling and elongation of rod-like micelles formed by them. Such modulations in the microstructure can arise from the changes in the configurational entropy of the chains in ion pairs. When the chain lengths of the two components are significantly different, the configurational entropy of the chains increases and favors loosely packed aggregates with highly curved cross section. When this mismatch decreases, the configurational entropy decreases and association of the components lead to closely packed ion pairs that are preferred for lamellar or disk-like aggregates. Thus, cross sectional swelling of rod-like micelles seems to be an intermediate state between polymer-like micelles and vesicles. Such swelling or elongation of the cross section of rod-like micelles occurs at the expense of average length of the micelles.

The results suggest a cooperative association between SL and cationic surfactant CTAB/TTAB to form viscoelastic networks at room temperature. These assemblies are different from the recently reported solid nanofibers formed by salt induced gelation of SL [68]. However, it was speculated that the solid gel phase formed in their study is originated from molecular quasi-crystallization of rod-like micelles induced by the addition of sodium ions. The present study reveals the formation of stable rod-like micelles in CTAB/TTAB–SL mixtures. The role of CTAB/TTAB in these mixed assemblies is manifold. Being cationic in nature, CTAB/TTAB can cooperatively associate with anionic SL molecules to form

aggregates of widely different morphologies, depending on the mixing ratio. Secondly, the head group in CTAB/TTAB is similar to the tetralkylammonium salts that have the ability to depress the Kraft point of SL and hence enhance the solubility in water. Complex assemblies comprising SL with potential application in cosmetic and pharmaceutical formulation have been reported recently [102]. Significant reduction in the cytotoxicity of alkyl oligoethyleneoxide carboxylates were observed by the addition of SL. The drug release studies employing catanionic vesicles and micelles entrapped in gels show that such mixtures are beneficial for obtaining prolonged release of drugs such as lidocaine, ibuprofen, naproxen, alprenolol, etc., as the drug release was prolonged significantly compared to the release of pure drug substances from the gel [103]. Formation of rod-like micelles and liquid-liquid phase separation in mixtures of DTAB and SL has been reported recently [104]. Three kinds of surfactant rich phases have been observed in DTAB-SL mixtures, depending on the mixing ratio. This includes entangled rod-like micelles, densely packed vesicles and lamellar phases. Thermally reversible ionogels of SL were prepared in a room temperature ionic liquid, ethyl ammonium nitrate [105]. These gels are formed by lamellar arrangement of SL-lauric acid mixtures in ionic liquid, as revealed by SAXS.

3.3 Effect of NaCl on CTAB/TTAB-SL mixed micelles

As discussed earlier in chapter 1, micelles are formed by self-aggregation of surfactant molecules in aqueous solution. The micelles formed at low concentrations are spherical and their structure changes with temperature, concentration, and in the presence of additives such as electrolytes, alcohols, and amines [106-108]. Addition of electrolytes like NaCl influences the growth behavior of ionic micelles. In the presence of electrolyte, the micellar growth is enhanced due to the screening of surface charges and dehydration of surfactant head group.

Chapter 3: Mixed surfactant systems

The same effect is applicable for the growth behavior of catanionic mixed micellar systems in the presence of electrolyte. An attempt has been made to relate the effect of electrolyte NaCl in modulating the packing of surfactant molecules in the micelles and hence alter the microstructure.

3.3.1 DLS studies: steric and electrostatic contribution to surfactant head group area

From the previous discussion, it is obvious that the equilibrium interfacial area occupied by the surfactant molecule arises from the steric repulsion of the hydrocarbon chain as well as the electrostatic repulsion of the charged head groups. The above two contributions can be separated if one looks into the effect of electrolytes on the equilibrium interfacial area. As discussed earlier, from the dimensions of the micelles, an effective packing parameter can be estimated which in turn is related to the effective interfacial area of the head group. For CTAB/TTAB–SL mixtures it is envisaged that the added electrolyte primarily influences the electrostatic interaction between unimers, as the dimers (ion-pairs) are electrically neutral. Figure 3.16 shows the variation in the diffusion coefficients of CTAB–SL mixed micelles as a function of NaCl concentration at different mole fractions of SL. As expected, the diffusion coefficient decreases with added NaCl concentration indicating growth of the micelles. From the measured diffusion coefficient of the micelles, the micellar length (L) is estimated, using the Perrin's relation (Figure 3.17). Similarly, Figure 3.18 shows the variation in the length of the TTAB–SL mixed micelles (as deduced from the apparent diffusion coefficient) with NaCl concentration, at different x_{SL}.
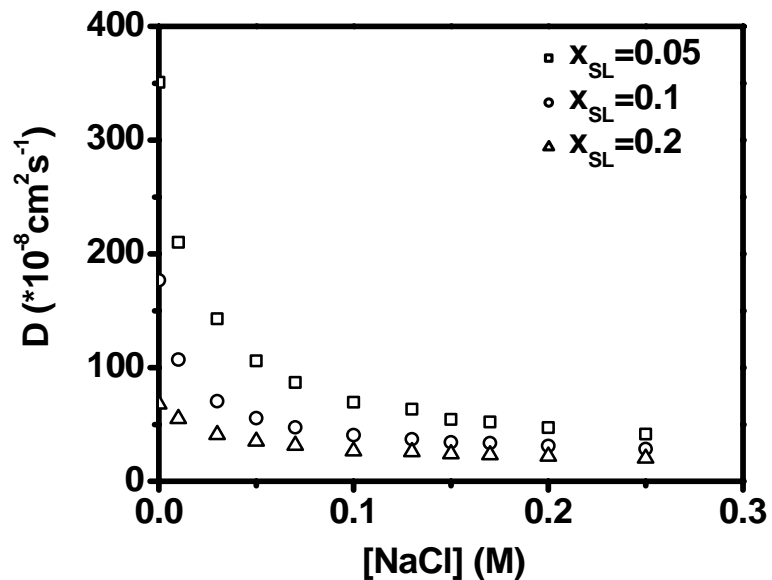
Figure 3.16 Diffusion coefficient of CTAB–SL mixed micelles as a function of NaCl concentration for three different mole fractions of sodium laurate (C_T = 0.1 M).
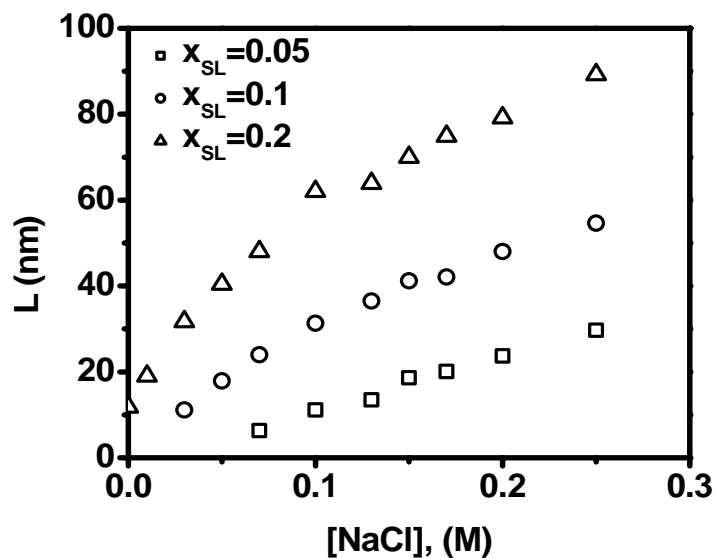
Figure 3.17 Variation in length (L) of CTAB–SL mixed micelles with NaCl concentration for three different mole fractions of sodium laurate (C_T = 0.1 M).
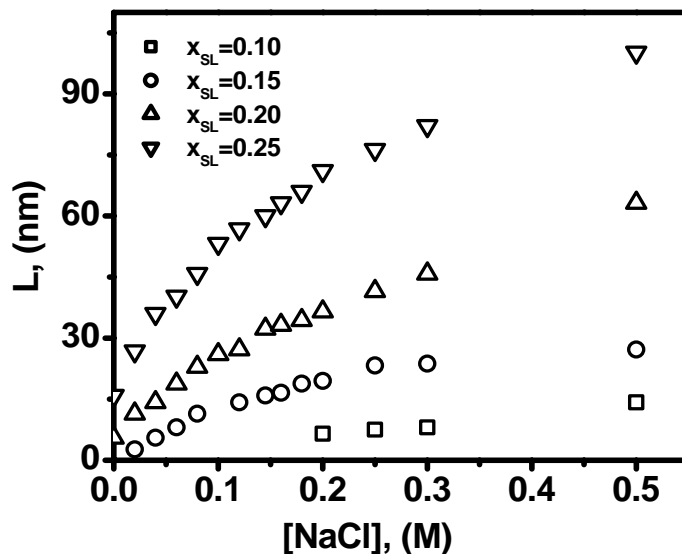
Figure 3.18 Variation in length (L) of TTAB–SL mixed micelles with NaCl concentration for four different mole fractions of sodium laurate ($C_T = 0.1$ M).

Substituting this value of L in equation 3.12 and equating it to equation 3.15, the packing parameter of the excess unimer in the mixture can be estimated, assuming a constant value for p_2. Since all measurements are restricted to $x_{SL} < 0.2$, it is reasonable to assume that the head group area of the dimer in CTAB–SL mixtures is approximately constant, being equal to 47.4 Å^2 which corresponds to a $p2$ of 0.75 (Figure 3.4A) and in the case of TTAB–SL mixed micelles, the head group area of the dimer equals 52.6 Å^2, as obtained from the infinite dilution value corresponding to $p2$ of 0.71 (Figure 3.4B). The variation in the equilibrium head group area per molecule of excess surfactant (CTAB) as a function of NaCl, at different mole fractions of SL, is shown in Figure 3.19 and Figure 3.20 depicts the variation in the equilibrium head group area per molecule of excess surfactant (TTAB) as a function of NaCl, at different mole fractions of SL. At all mole fractions, the equilibrium area per molecule decreases with electrolyte concentration. This decrease in the area per molecule as a

function of added electrolyte concentration suggests electrostatic repulsion between charged head groups, in addition to the steric repulsion between molecules. At sufficiently high electrolyte concentration, it saturates to a value that corresponds to the area arising from steric and electrostatic contribution. The electrostatic contribution to the interfacial area is the one that is sensitive to electrolyte concentration. This has been addressed by Nagarajan in terms of the Debye-Huckel form of the interaction free energy, and the ionic strength dependence of the electrostatic contribution can be written as [73]

$$a_e = a_0 (\frac{1}{1 + \kappa l_c})^{1/2}$$

(3.25)

where a_0 is electrostatic interaction area in the absence of electrolytes, l_c is the length of hydrocarbon chain and κ is the inverse Debye screening length, given by

$$\kappa = \left[\frac{8 \pi n_0 e^2}{\varepsilon k_B T} \right]^{1/2}$$

(3.26)

where n_0 is the number of counterions in solution per cm^3 and e is the electronic charge. Incorporating this term, the total interfacial area per surfactant as a function of the added electrolyte can be written as

$$a_1 = a_{st} + a_0 (\frac{1}{1 + \kappa l_c})^{1/2}$$

(3.27)

where a_{st} is the head area due to steric contribution. The measured area per surfactant (CTAB) as a function of NaCl concentration can be fitted reasonably well (solid lines in Figure 3.19a, b and c) using equation 3.27 and the corresponding values of a_{st}, a_0 and a_{total} (where $a_{total} = a_{st} + a_0$) are summarized in Table 3.3. Similarly, the measured area per surfactant (TTAB) as a function of NaCl concentration can be fitted reasonably well (solid lines in Figure 3.20a,

b and c) and the corresponding values of a_{st}, a_0, and a_{total} (where $a_{total}=a_{st}+a_0$) are summarized in Table 3.4.
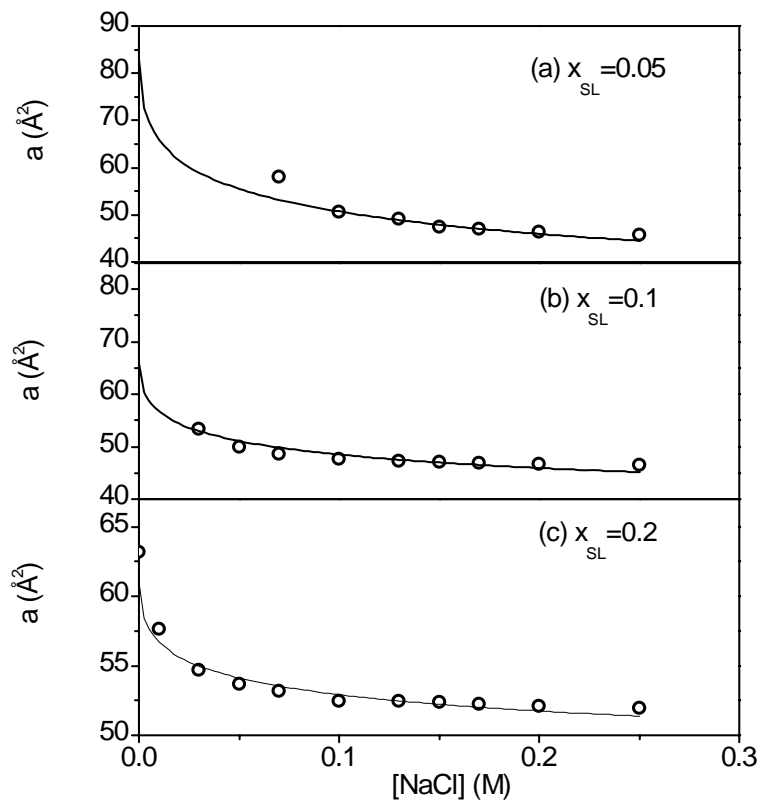
Figure 3.19 Variation of the effective area per molecule of excess CTAB in a mixture of CTAB and SL (C_T = 0.1 M) with NaCl concentration, at a fixed mole fraction of sodium laurate a) x_{SL}=0.05, b) x_{SL} =0.1, c) x_{SL} =0.2. The solid lines are fit to the data using equation 3.27.

Table 3.3 Values of steric (a_{st}) and electrostatic (a_0) contribution to the head group area of surfactant (CTAB) in CTAB–SL mixed micelles at different mole fractions of sodium laurate (x_{SL}).

Mole fraction of sodium laurate (x_{SL})	a_{st} (Å^2)	a_0 (Å^2)	a_{total} (Å^2)
0.05	11	72	83
0.1	27	39	66
0.2	43	18	61

83
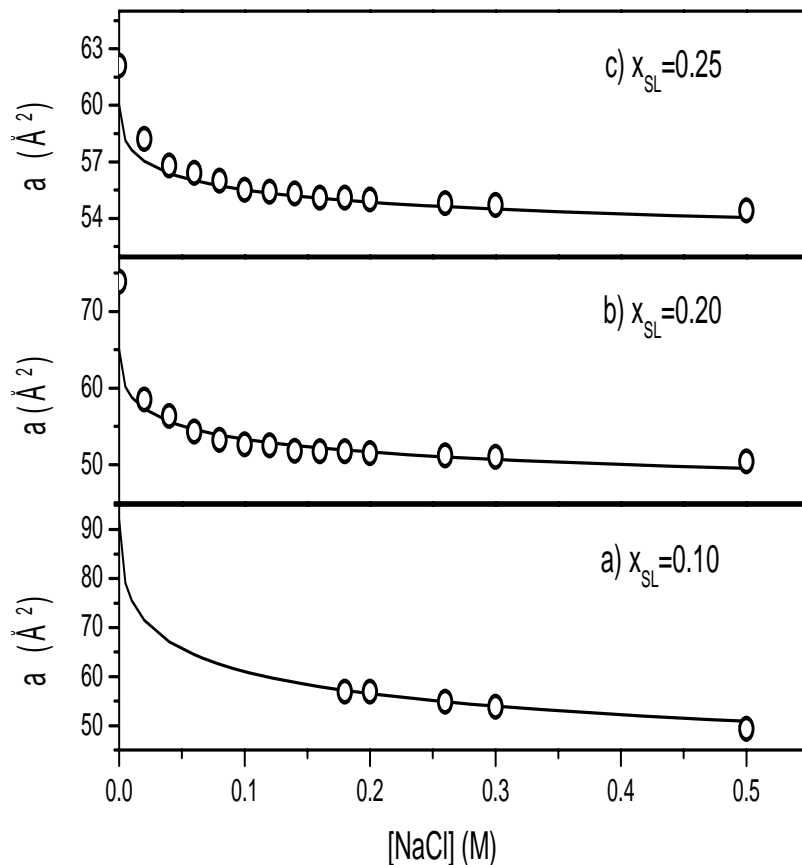
Figure 3.20 Variation of the effective area per molecule of excess TTAB in a mixture of TTAB and SL (C_T = 0.1 M) with NaCl concentration, at a fixed mole fraction of sodium laurate a) x_{SL}=0.10, b) x_{SL} =0.20, c) x_{SL} =0.25. The solid lines are fit to the data.

Table 3.4 Values of steric (a_{st}) and electrostatic (a_0) contribution to the head group area of surfactant (TTAB) in TTAB–SL mixed micelles at different mole fractions of sodium laurate (x_{SL}).

Mole fraction of Sodium laurate (x_{SL})	a_{st} (Å^2)	a_0 (Å^2)	a_{total} (Å^2)
0.10	23	69	92
0.20	26	39	65
0.25	50	10	60

This allows us to separate the steric and electrostatic contribution to the head group area of surfactant. The calculation of equilibrium area per surfactant molecule rests on the

assumption that there is no specific interaction between the surfactant and cation–anion pair. It is noted that the steric contribution increases with sodium laurate addition while the electrostatic contribution decreases. The observed strong variation in the steric and electrostatic contribution to the head group area arises from the fact that with increase in x_{SL}, the ionic surfactants are farther apart due to the intervening neutral ion pairs. As more and more ion pairs are present the steric repulsion due to the bulky alkyl chains of the dimer and monomer increases while the charged unimers are now farther apart and hence the electrostatic area decreases. The electrostatic contribution to the head group area of the CTAB surfactant at the lowest mole fraction of SL is 72 Å^2 and that of the TTAB surfactant is 69 Å^2. Both the values are consistent with the values reported by Nagarajan [73].

3.3.2 SANS studies on the effect of NaCl on CTAB–SL mixtures

SANS measurements were also performed on CTAB–SL samples, in the presence of 0.1 M NaCl, at different x_{SL} as depicted in Figure 3.21. In contrast to the spectra in Figure 3.5 (in the absence of NaCl), the correlation peak is less pronounced, which indicates that interparticle interaction between the micelles is negligible. This is expected as the added electrolyte can screen the electrostatic repulsion. One can clearly see the increase in forward scattering with the addition of SL. For long, rod-like micelles the scattering intensity should lead to a q^{-1} behavior in the scattering curve. A q^{-1} line is added to Figure 3.21 for comparison. It is clear that the scattering pattern at high x_{SL}, approaches to q^{-1} behavior. The scattering pattern at x_{SL}=0.1 and 0.2 are practically identical suggesting a saturation in the growth behavior. However, the R_h of the micelles (measured by DLS, Figure 3.1) at x_{SL}=0.1 and 0.2 are significantly different. This is due to the fact that the accessible length scale

probed by the SANS instrument is shorter than the maximum length of the micelles at x_{SL}=0.2. Since the intermicellar interaction is relatively weak in the presence of NaCl, we

Figure 3.21 SANS spectra for CTAB–SL mixed micelles in 0.1 M NaCl with varying mole fraction of sodium laurate (C_T = 0.1 M).The spectra of x_{SL} > 0 are offset by a factor of 2 for clarity. The solid lines are fit to the data using ellipsoidal micelles.

first employed the model independent IFT method, to assess the structural changes. The IFT method allows us to evaluate the pair distance distribution function (PDDF), p(r), of the micelles. The scattering intensity is related to the p(r) by the equation

$$I(q) = 4\pi \int_0^\infty p(r) \frac{\sin{(qr)}}{qr} dr \qquad (3.28)$$

where $\qquad p(r) = \Delta\tilde{\rho}^2(r)r^2. \qquad (3.29)$

The PDDF is directly related to the internal structure of the particle through the convolution of the scattering length density profile. The Fourier transformation is performed using the program GENOM developed by Svergun [109]. Variations in the p(r) function of the micelles

with changes in x_{SL}, as obtained from the IFT analysis, are depicted in Figure 3.22. The PDDF of pure CTAB micelles, shows the influence of structure factor (though weak), as indicated by a weak oscillation in $p(r)$. With the addition of SL, this oscillation disappears and the micelles continuously transform to short rods with nearly constant cross-sectional dimension and
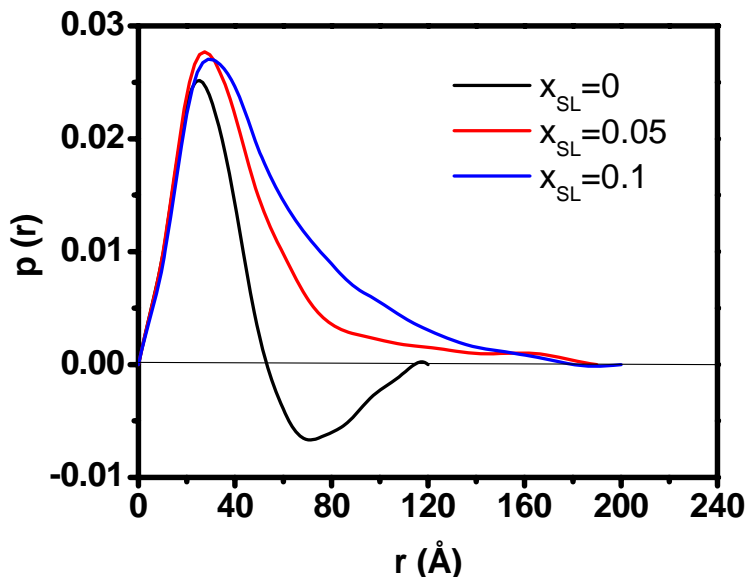
Figure 3.22 PDDFs (obtained from the IFT analysis of the SANS spectra) of CTAB–SL mixed micelles in 0.1 M NaCl with varying mole fraction of sodium laurate ($C_T = 0.1$ M).

increasing average length. Based on the structural information obtained from IFT analysis, the SANS data were fitted using a prolate ellipsoid model. In the absence of NaCl, the intermicellar interaction is taken into account using a screened coulomb form of the potential. In the presence of NaCl, no interparticle interaction is taken into account. The solid lines in Figure 3.20 are model fits to the data and the parameters obtained are summarized in Table 3.5. In electrolyte, the trend with mole fraction of SL is similar to that in the absence of salt, except that the growth is less pronounced at high x_{SL}. This is consistent with the electrolyte

Table 3.5 Micellar parameters obtained from the SANS fit for 0.1 M CTAB–SL mixed micelles with varying mole fraction of sodium laurate in the presence of 0.1 M NaCl.

S.No.	Mole fraction of Sodium laurate (x_{SL})	Aggregation number (N_{agg})	Fractional charge (α)	Semiminor axis, a (Å)	Semimajor axis, b (Å)	Axial ratio
1	0	177	0.20	22.0	52.8	2.4
2	0.05	281	0.02	22.2	81.0	3.6
3	0.1	462	0.02	23.5	115.9	4.9
4	0.2	395	0.02	22.8	101.4	4.4

screening the charge on the excess cationic surfactants and promoting micellar growth. As x_{SL} increases, the charge density of the micelles decreases, hence the effect of electrolyte is marginal. Both model dependant analysis and IFT analysis clearly suggests a transition from globular micelles to short rod-like aggregates.

3.3.3 SANS studies on the effect of NaCl on CTAB–SL mixtures

Figure 3.23 shows the SANS spectra for TTAB–SL mixed micelles with increasing x_{SL}, (total surfactant concentration of 0.1 M), in the presence of 0.2 M NaCl. Variations in the $p(r)$ function of the micelles at different x_{SL}, as obtained from the IFT analysis, are depicted in Figure 3.24. Analysis shows that $S(q)$ effects are present at low x_{SL}, as indicated by a weak oscillation in $p(r)$. With the addition of SL, this oscillation disappears and the micelles continuously transform to short rods with increasing average length. All the $p(r)$ curves show

pronounced peak in the low r side with an asymmetric tail in the higher r side indicating prolate ellipsoidal micelles. With increase in x_{SL}, the position of the peak in the $p(r)$ function

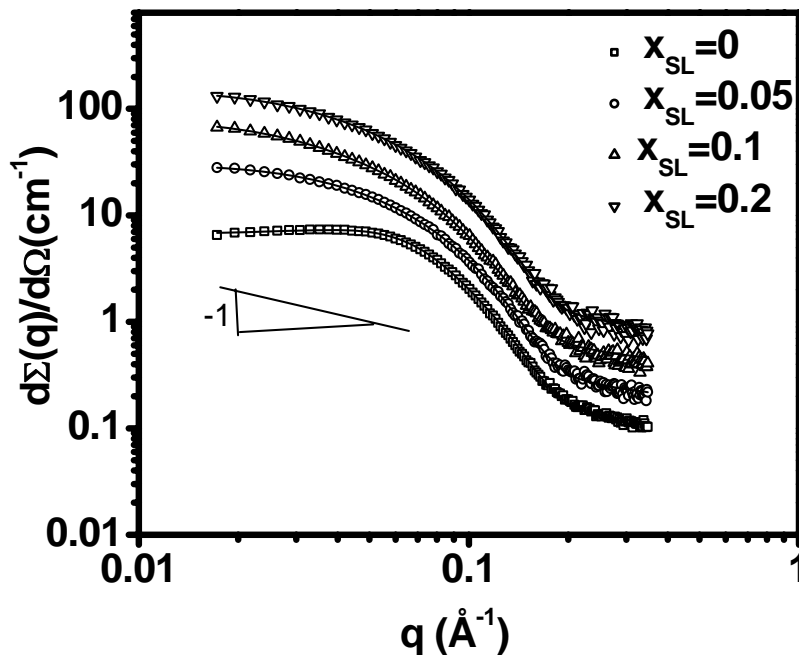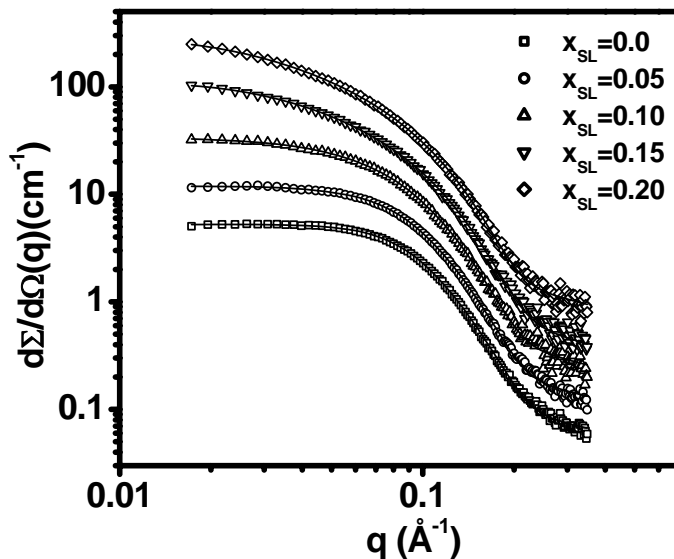**Figure 3.23** SANS spectra for TTAB–SL mixed micelles in 0.2 M NaCl at different mole fractions of sodium laurate ($C_T = 0.1$ M). The spectra of $x_{SL} > 0$ are offset by a factor of 2 for clarity (solid lines show the fits to the data).
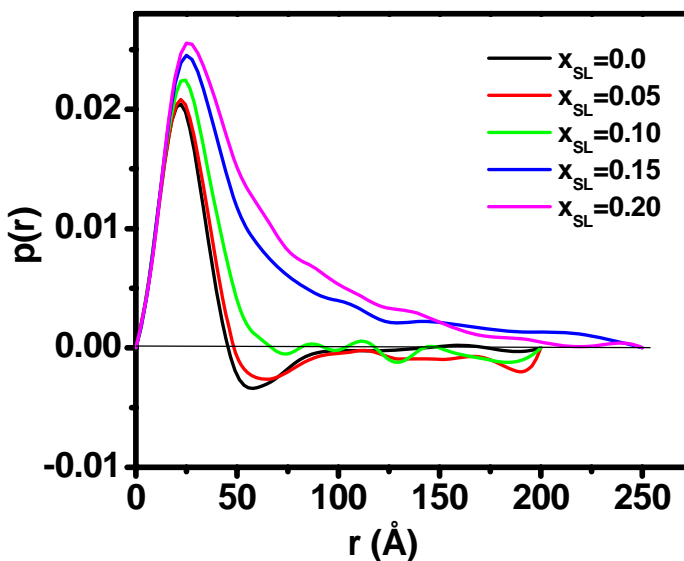
Figure 3.24 PDDFs (obtained from the IFT analysis of the SANS spectra) of TTAB–SL mixed micelles in 0.2 M NaCl at different mole fractions of sodium laurate ($C_T = 0.1$ M).

shift slightly to higher r-values confirming that swelling of the cross section indeed occurs. The maximum r at which $p(r)$ disappears increase with increase in x_{SL}. Based on the structural information obtained from IFT analysis, the SANS data were fitted using a prolate ellipsoid model, without considering any intermicellar interaction. The solid lines in Figure 3.23 are model fits to the data, and the parameters obtained are summarized in Table 3.6.

Table 3.6 Micellar parameters obtained from the SANS fit for 0.1 M TTAB–SL mixed micelles with varying mole fraction of sodium laurate in the presence of 0.2 M NaCl.

S.No.	Mole fraction of Sodium laurate (x_{SL})	Aggregation number (N_{agg})	Fractional charge (α)	Semiminor axis, b (Å)	Semimajor axis, a (Å)	Axial ratio
1	0	105	0.21	18.8	39.6	2.11
2	0.05	120	0.16	19.2	42.4	2.20
3	0.1	143	0.01	19.6	48.0	2.45
4	0.15	254	0.01	19.1	87.7	4.58
5	0.2	350	0.01	19.8	110.61	5.58

Also, the variation in the aggregation numbers of TTAB–SL mixed micelles both in the absence (Figure 3.6) and in the presence of NaCl (Figure 3.23) is depicted in Figure 3.25. At low x_{SL}, the aggregation numbers are almost same; indicating that salt concentration is just enough to screen the charges on the micelles and does not induce any further growth. However, at high x_{SL}, since the effective charge on the micelle is already low, added NaCl induces further growth of the micelles. Since the main aim of adding electrolyte to the micelles is to screen the surface charge of the micelles, SANS studies in the presence of electrolyte is restricted to low x_{SL} values.
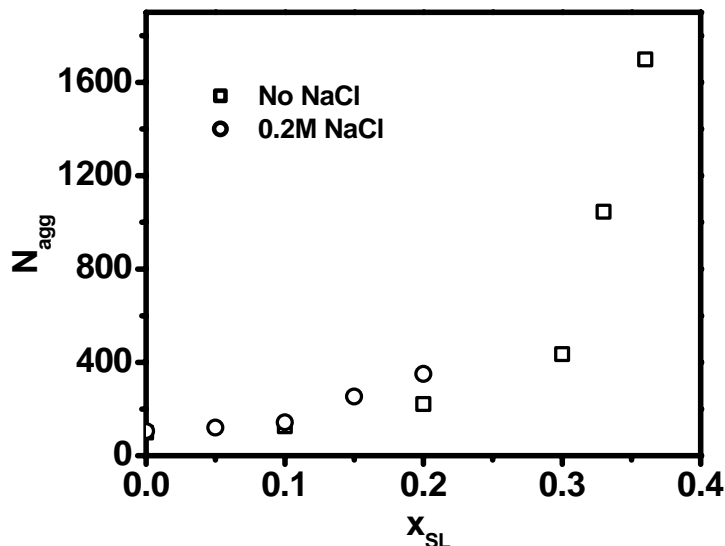
Figure 3.25 Aggregation number of TTAB–SL mixtures (C_T = 0.1 M) at different mole fractions of sodium laurate, in the presence (0.2 M NaCl) and absence of NaCl.

A detailed study of different salts on the mixtures of DTAB and SL has been reported by Vlachy *el al.* [110]. The mechanism of salt binding and the micellar growth was governed by the ability of counterion to dehydrate the surfactant head group. Also, the effect of salt on the head group of the mixed micelles of sodium dodecylsulfate (SDS) and dodecyltrimethylammonium chloride (DTAC) has been demonstrated recently by Sylvain *et al.* [111]. They studied the effect of ions on the head group of pure surfactants in a catanionic pair by using ions that mimic the head group of the paired surfactant. For example, tetramethylammonium chloride (TMACl) was added as an external electrolyte to SDS and sodium methylsulfate (SMS) to DTAC micelles. The effect of salt addition to these two surfactants is clearly strongly ion specific.

3.3.4 Rheological studies on the effect of NaCl on CTAB-SL mixed micelles

Next a preliminary study on the effect of electrolyte on the rheology of CTAB–SL mixed micelles has been done, as the structural transition in the mixed micelles changes the

rheological properties of the fluids significantly. The shear dependent viscosity of CTAB–SL mixed micelles with NaCl concentration for three different mole fractions of sodium laurate, x_{SL}= 0.05, 0.1, and 0.2 (total surfactant concentration taken as 0.1 M) are depicted in Figures 3.26, 3.27 and 3.28 respectively. It is noted that in the case of x_{SL} 0.05 and 0.1, the viscosity is independent of shear rate i.e. they are behaving as Newtonian fluids but in the case of x_{SL} equals 0.2, at high concentration of NaCl, the viscosity becomes shear dependant with a shear thinning behavior at high shear rates. This non-Newtonian (shear thinning) behavior is observed when the micelles are long enough to form entangled structures. In all samples, a viscosity plateau is observed at low shear rates, enabling us to evaluate the zero shear
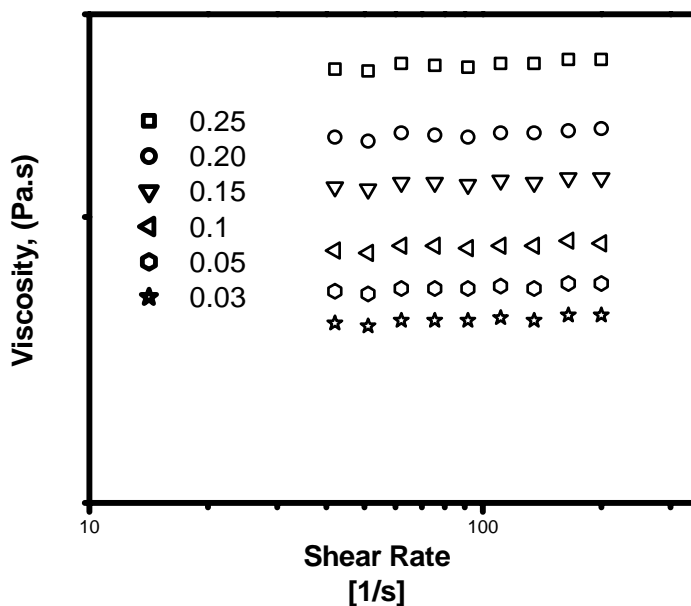
Figure 3.26 Viscosity, η, of CTAB–SL mixtures (C_T = 0.1 M) as a function of shear rate with varying concentration of NaCl at x_{SL} = 0.05.
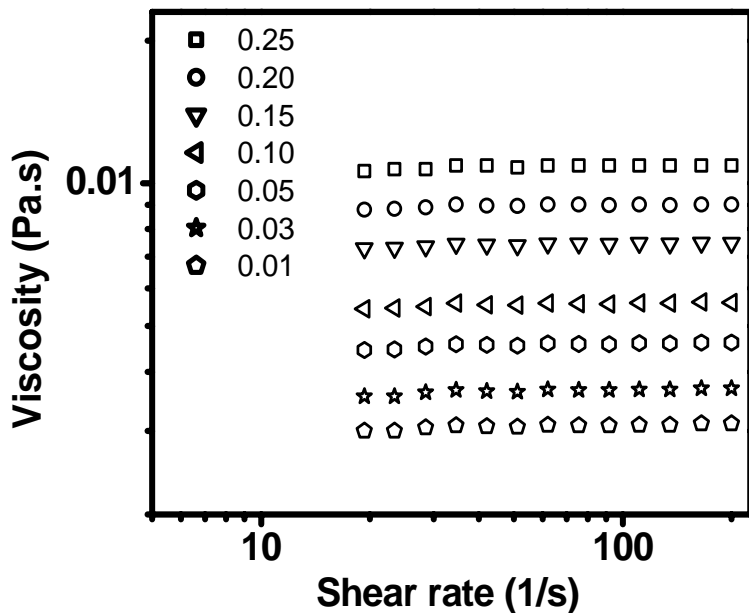
Figure 3.27 Viscosity, η, of CTAB–SL mixtures ($C_T = 0.1$ M) as a function of shear rate with varying concentration of NaCl at $x_{SL} = 0.10$.
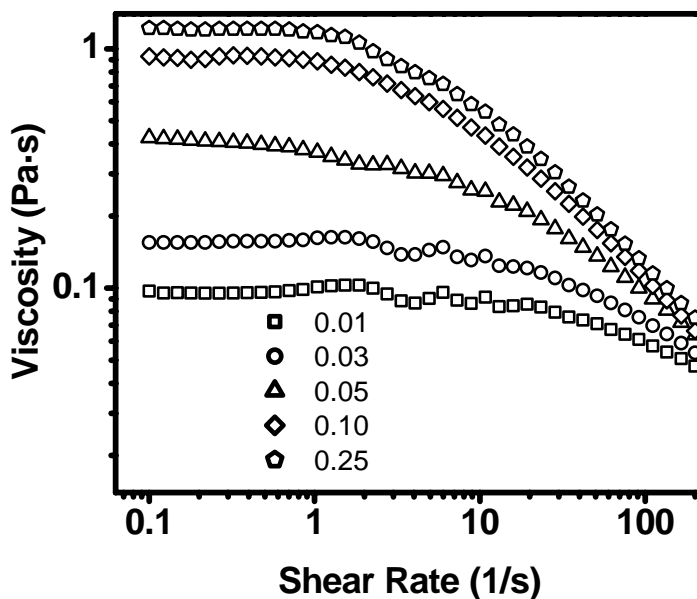
Figure 3.28 Viscosity, η, of CTAB–SL mixtures ($C_T = 0.1$ M) as a function of shear rate with varying concentration of NaCl at $x_{SL} = 0.20$.

93

viscosity of the micellar fluid. The variation in the zero shear viscosity with NaCl concentration for three different mole fractions of sodium laurate, x_{SL} 0.05, 0.1, and 0.2 (total surfactant concentration taken as 0.1 M) is depicted in Figure 3.29.
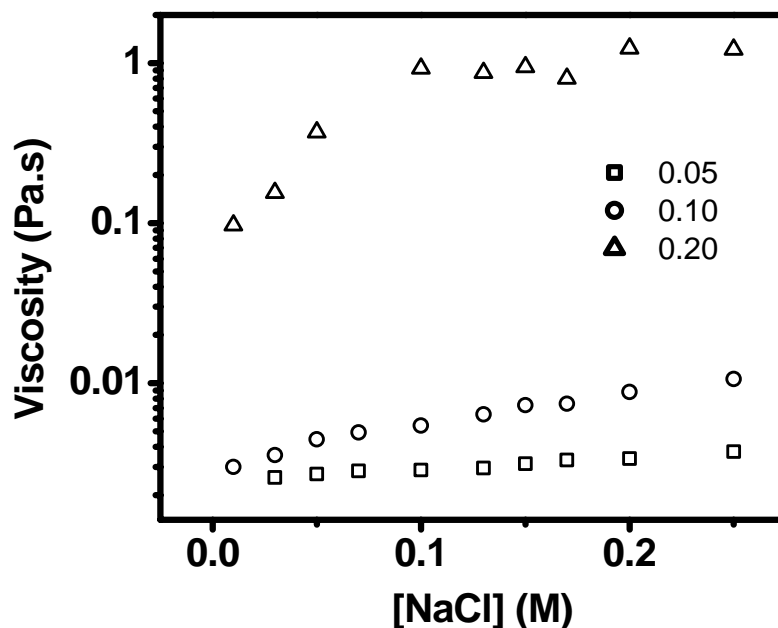
Figure 3.29 Variation of the zero-shear viscosity, η_0, of CTAB–SL mixed micelles with varying concentration of NaCl at $x_{SL} = 0.05$, 0.1, and 0.2 ($C_T = 0.1$ M).

It can be observed that there is a structural growth with the addition of NaCl. As seen from Figure 3.1, the R_h of the micelles are small in the case of x_{SL} 0.05 and 0.1, hence the effect of NaCl on the growth behavior is not very prominent in the studied concentration range of electrolyte. But in the case of x_{SL} 0.2, the effective fractional charge on the micelles is negligible, R_h value is high, hence the addition of NaCl causes a strong structural growth of the micelles and the micelles eventually develop into long, flexible, randomly oriented micelles, owing to which the system exhibits shear thinning behavior.

3.4 Conclusion

The aim of the present work was to understand the effect of chain length asymmetry on the equatorial and axial growth of the C_nTAB─sodium laurate mixed micelles. Besides being naturally occurring, lauric acid and its sodium salt are biocompatible ingredients with self-assembling properties. However, their applications are limited due to high Kraft point, which is well above the room temperature. In the presence of CTA/TTA based cationic surfactants, the Kraft point decreases and it undergoes cooperative self-assembly to form long worm-like micelles. Using SANS, the axial and equatorial growth of CTAB/TTAB micelles induced by the addition of SL have been investigated. Both CTAB and TTAB micelles undergo elongation to form rod-like assemblies by the addition of SL. The axial growth is more pronounced in CTAB micelles. However, TTAB micelles undergo equatorial swelling and elongation by the addition of SL. Difference in the growth behavior of TTAB and CTAB micelles can be attributed to the asymmetry in the chain lengths of cationic-anionic pairs. The fact that CTAB has two carbon atoms more in the hydrocarbon chain than in TTAB leads to greater asymmetry in the chain lengths of CTAB and SL. This induces subtle changes in the packing parameter of the mixtures by incorporation of catanionic salt with a packing parameter favorable for axial elongation of the micelles. However, in TTAB─SL mixed micelles, the catanionic salt will have a packing parameter close to unity, as the two chains have more or less equal lengths. This favors disk-like micelles and hence in a mixture of TTAB and SL, the local structure of the micelles will favor disk-like aggregates. This induces equatorial growth of the micelles in addition to elongation. The effective interfacial area occupied by the cationic─anionic pair was estimated from the measured length of the rod-like aggregates and it indicates enhanced steric repulsion between the ion pairs. Also, from the

95

electrolyte effect on the equilibrium area per monomer, the contributions from steric and electrostatic effects can be separated. The formation of an ion pair leads to decrease in the electrostatic contribution to the head group area due to charge neutralization and the steric contribution from the hydrocarbon tails increases with increasing fraction of ion pairs. In the presence of the electrolyte, micellar growth is more pronounced due to its screening effect. Rheological studies confirm the formation of rod-like aggregates in CTAB/TTAB─SL mixture with an increase in the mole fraction of sodium laurate. Steady flow rheological measurements indicate Newtonian behavior when the axial ratio of the micelles is small, while non-Newtonian (shear thinning) behavior is observed when the micelles are long enough to form entangled structures. Dynamic rheology of the entangled micelles is similar to Maxwell fluids, which is the basic model for a viscoelastic fluid. Comparing the position of maxima in the zero shear viscosity vs concentration of C_nTAB-SL mixtures suggests that axial growth is more for surfactant with longer hydrocarbon chain.

CHAPTER 4

Worm-like micelles and vesicles in mixed surfactants: Rheology and Microstructure

4.1 Introduction

Surfactant based viscoelastic fluids comprises rod-like or worm-like micelles in aqueous solution. When the number density of these worm-like micelles is sufficiently large, they entangle into a transient network leading to viscoelastic solutions that are analogous to that of semidilute polymer solutions [66, 101]. These worm-like micelles are similar to polymers as they are quite flexible and exhibit contour lengths of the order of micrometers [63, 112]. However, unlike classical polymers, worm-like micelles constantly break and recombine on a characteristic time scale as they are in thermal equilibrium with its monomers. Hence, they do not exhibit a quenched contour length (molecular weight) distribution and they are often called as 'equilibrium' polymers or 'living' polymers. Hence basic polymer chemistry has been very useful to gain additional insight into the physical chemistry of viscoelastic surfactant solutions.

The scaling of rheological parameters of such worm-like micelles (WLMs) have been studied in detail by various groups and explained in terms of the reptation-reaction theory [113]. Typically WLMs are formed by ionic surfactants in the presence of electrolytes or oppositely charged additives. This is because addition of salts or oppositely charged additives screens the electrostatic interaction between the charged head groups and allows closer packing of the surfactant monomers in the aggregate. This favors transition from spherical to cylindrical aggregates. One common feature in the rheology of such WLMs is that various ionic surfactants show a pronounced maximum of the zero-shear viscosity as the salt/surfactant ratio is varied [114-117]. This has been attributed to the formation of branched micelles at high salt to surfactant ratio. Direct observation of microstructures by cryo-TEM in a variety of micelles beyond the viscosity maximum proved the existence of micellar

branching. The scaling exponents of rheological parameters of entangled polymers have shown to be sensitive to polymer topology. For example, comparing the rheological spectra of linear and star polymer melts show widely differing properties. As opposed to linear polymers, a much broader range of relaxation time is observed for branched polymers [113]. The rheological behavior of worm-like micelles follows simple scaling laws [118, 119], also discussed later in the chapter. However, experimental results prove that the scaling law is applicable for nonionic worm-like surfactant systems. It has been reported that there is a deviation from this law for ionic worm-like micelles, due to the electrostatic interactions among the constituent ionic surfactant moieties [56]. However, there is no report on the dependence of the scaling of plateau modulus G_0 on the structural properties of the micellar system. An effort has been made to span the entire range of concentrations, comprising both linear and branched micelles and a clear difference in the scaling behavior of shear modulus could be identified. Theoretical models developed to account for the viscosity of linear and branched micelles assumed a constant value of scaling exponents for the shear modulus. Here, the rheological scaling of plateau modulus in a worm-like micellar fluid in the concentration range where linear and branched micellar transition occurs has been explored. Typically, worm-like micelles are formed by the addition of oppositely charged hydrotropes or surfactants to an ionic micellar solution. Surfactant mixtures will be the preferred choice than hydrotropes for this study, as there is a possibility of changes in the composition of mixed micelles in case of surfactant–hydrotrope mixtures. This is due to the fact that hydrotropes, by itself, do not form any aggregates at low concentration and hence the composition of hydrotropes in the micelles can vary with concentration.

Rheological studies on the viscoelastic fluids comprising long chain cationic alkyltrimethylammonium bromide and hydrophobic counter ions or anionic surfactants have already been reported by other groups [120-130]. The length of the hydrocarbon chain in alkyltrimethylammonium bromides (C_nTAB) affect the rheology of C_nTAB–sodium oleate (NaOL) mixtures, as reported by Raghavan *et al.* [18]. They hypothesized the occurrence of the maximum in the viscosity plot of NaOL/C_8TAB mixtures as a function of total surfactant concentration is due to the formation of branched micelles. Later Cui *et al.* has demonstrated through cryo-TEM imaging that the maximum in the shear viscosity is due to the transition from linear to branched micelles [131]. In this study, NaOL has been selected as the anionic surfactant for the formation of catanionic micelles in conjunction with cationic CTAB solution. The selection of NaOL was based on the fact that NaOL being a surfactant, there is minimal possibility of being leached out of the mixed micelles upon dilution, as opposed to hydrotropes. Hence rheological parameters of a given mole fraction can be investigated over a wide range of concentration. With this aim, a detailed rheological study on the CTAB–NaOL catanionic mixture was done to determine the effect of structural transition on the rheological parameters of the mixed micelles.

4.2 Theoretical Background: Dynamics of 'living' polymers

The dynamics of such a "living" polymer solution in the semidilute regime was studied in detail by Cates and co-workers [64, 132, 133]. The model of Cates is based on the reptation model of polymer dynamics but including the effect of reversible scission kinetics on the viscoelastic behavior. This model involves two relevant time scales that are the reptation time, τ_{rep}, and the breaking time, τ_b. The reptation time corresponds to the curvilinear diffusion of a chain of the mean length $\bar{L}$ along a tube that is constrained by the

entanglements from other chains and the breaking time corresponds to the mean time required

for a chain of length $\bar{L}$ to break into two pieces. It is assumed that the chemical relaxation

process is the reversible unimolecular scission characterized by a temperature-dependent rate

constant k_1 per unit arc length per unit time, which is same for all elongated micelles and is

independent of time and of volume fraction. This assumption results in

$$\tau_b = (k_1 \bar{L})^{-1}$$

(4.1)

For $\tau_b \gg \tau_{rep}$, the dominant stress relaxation mechanism is reptation. Then the stress

relaxation function indeed obeys the equation [64]

$$\mu(t) \sim \exp(-t/\tau_{rep})^{1/4}$$

(4.2)

as expected for a system of chains with exponential polydispersity. Thus in this regime the

terminal relaxation time, $\tau_R = \tau_{rep}$.

The zero shear viscosity η_0 is related to the terminal time τ_R and the plateau modulus G_0 by

the relation

$$\tau_R = \eta_0/G_0$$

(4.3)

When $\tau_b \ll \tau_{rep}$, an interesting new regime occurs. In this regime, chain breakage and

recombination will both occur often, for a typical chain, before it reptates out of the tube

segment. The stress relaxation is then characterized by a new intermediate time scale;

$$\tau_R = (\tau_b \tau_{rep})^{1/2}$$

(4.4)

that is associated with a process whereby the chain breaks at a point close enough to a given

segment of tube for reptation relaxation of that segment to occur before a new chain end is

lost by recombination. The stress relaxation function thus becomes more like a single

exponential because before a given tube segment relaxes, the chain occupying it typically

undergoes many scission and recombination reactions, so that there is no memory of either the initial length of the chain or the position on the chain initially corresponding to the tube segment. Thus at low frequencies the behavior of the liquid is Maxwellian and is described by equations 2.50 and 2.51. The Cole-Cole representation, in which the imaginary part $G''(\omega)$ of the frequency-dependent shear modulus is plotted against the real part $G'(\omega)$, can be used to get an estimate of the relaxation time, τ_R. Thus at low frequencies the behavior of the liquid is Maxwellian and is ascertained by a semicircular shape of the Cole-Cole plot $G''(G')$, but deviations from the half circle occur at a circular frequency, ω, of the order of the inverse of the breaking time of the micelles. The model of Granek and Cates [70] can also be applied to study the regimes involving small time scales where the dominant polymer motion is not reptation but either breathing (which arises from the tube length fluctuations) or the local Rouse-like motion (arising from stretches of chain shorter than the entanglement length, l_e). This regime is characterized by an apparent turn up of both $G'(\omega)$ and $G''(\omega)$ at high frequencies. This results in a minimum in the G" vs G' plot (G''_{min}) and extrapolation of G' to x-axis yields G'_∞. This picture applies when the entanglement length, l_e, is much larger than the persistence length, l_p, and the breaking time is much larger than the Rouse time, τ_e. It was found that, provided $\tau_b \gg \tau_e$, the value of $G''(\omega)$ at the dip obeys the relation

$$G''_{min} / G'_\infty = l_e / \bar{L}$$

(4.5)

From the values of G''_{min}, G'_∞, and l_e one can thus obtain an estimate of micellar length $\bar{L}$. For flexible micelles the entanglement length, l_e, can be estimated from the relation [134]

$$G'_\infty = \frac{k_B T}{\xi^3} = \frac{k_B T}{l_e^{9/5} l_p^{6/5}}$$

(4.6)

where ξ is the correlation length which gives the mesh size of the network.

4.2.1 Scaling behavior to dilution

The reptation theory of semidilute polymer solutions predicts that [135]

$$\tau_{rep} \propto \bar{L}^3 \varphi^{3/2} \tag{4.7}$$

where φ is the total volume fraction of micelles

Combining equation 4.6 with the $\varphi^{1/2}$ dependence of $\bar{L}$ yields

$$\tau_{rep} \propto \varphi^3 \tag{4.8}$$

Combining equation 4.1 with the $\varphi^{1/2}$ dependence of $\bar{L}$ yields

$$\tau_b \propto \varphi^{-1/2} \tag{4.9}$$

For flexible micelles in the fast breaking limit the stress relaxation time, τ_R obeys the equation 4.4 and therefore combining equations 4.7 and 4.8 together with the equation 4.4 gives

$$\tau_R \sim \varphi^{5/4} \tag{4.10}$$

In the slow breaking limit, $\tau_R = \tau_{rep}$ and it follows from equation 4.8 that

$$\tau_R \sim \varphi^3 \tag{4.11}$$

The mesh size varies according to the power law [136, 137]

$$\xi \approx \varphi^{-3/4} \tag{4.12}$$

For semidilute solutions, it has been shown that

$$G_0 = \frac{kT}{\xi^3} = kT\varphi^{2.3} \tag{4.13}$$

The zero shear viscosity is related to the terminal time and plateau modulus according to the equation

$$\eta_0 = G_0\tau_R \tag{4.14}$$

Therefore, in the fast breaking limit zero shear viscosity scales as

$$\eta_0 \propto \varphi^{3.5} \tag{4.15}$$

Whereas in the slow breaking limit, η scales as

$$\eta_0 \propto \varphi^{5.3} \tag{4.16}$$

The above scaling exponents were obtained assuming good solvent conditions and for fully screened electrostatic effects. But deviations from the above mentioned scaling behavior occurs due to the presence of electrostatic effects.

4.3 Rheology of CTAB-NaOL mixture

Sodium oleate (NaOL) is a well-known surfactant for its high interfacial activity. It has been applied in many fields such as being one of the main constituents of cell membranes, useful for biological applications, and also can be used as collectors in the flotation deinking of paper and minerals [138, 139]. The presence of a long hydrocarbon chain with an unsaturation makes it conducive for the formation of complex catanionic aggregates without phase separation [140]. CTAB–NaOL mixtures form viscoelastic fluids over a wide range of composition and concentration. Under appropriate conditions, linear or branched worm-like micelles are formed in CTAB–NaOL mixtures. Traditionally, the existence of branched micelles has been hypothesized from a decrease in the viscosity of the fluid with increase in mole fraction or concentration. Firstly, the microstructural evolution has been identified from steady shear rheology. Figure 4.1 shows the shear dependent viscosity of CTAB–NaOL micelles (total surfactant concentration is 0.1 M) at different mole fractions of NaOL (x_{NaOL}). At lower x_{NaOL}, viscosity is independent of shear rate, i.e. Newtonian flow behavior is observed in the studied shear range. When the mole fraction is above 0.2, the Newtonian behavior occurred at low shear rates only and shear thinning is observed at large

deformations, when the shear rate exceeds a critical value. With an increase in x_{NaOL} upto a value of 0.25, the critical shear rates for shear thinning shift gradually to lower values. However, with further increase in x_{NaOL}, again higher deformation rates are required to induce shear thinning. The zero shear viscosity i.e. viscosity plateau at low shear rates, as a function
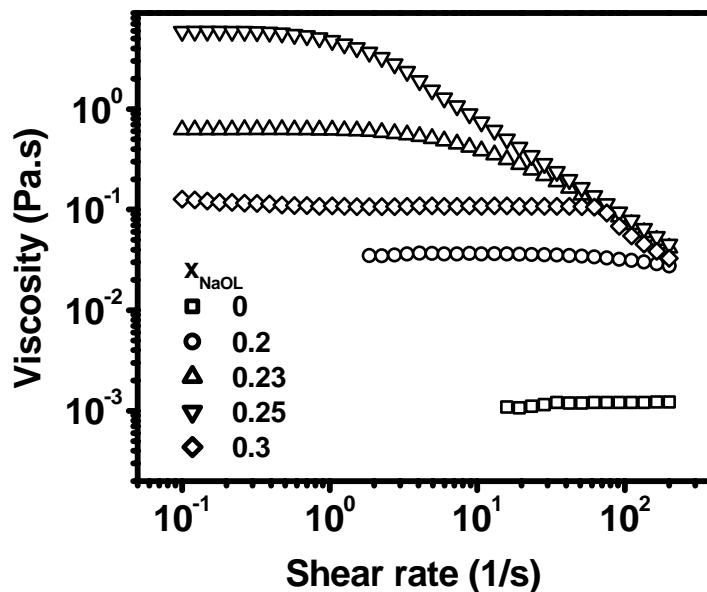
Figure 4.1 Viscosity, η, of CTAB–NaOL mixtures (total surfactant concentration, C_T = 0.1 M) as a function of shear rate at different mole fractions of sodium oleate (x_{NaOL}).

of x_{NaOL} is depicted in Figure 4.2. The zero shear viscosity is comparable to that of water at low x_{NaOL}, which increases to a maximum, nearly 4 orders of magnitude higher than that of water and then again decreases with increasing x_{NaOL}. This rheological behavior is typical of worm-like micellar system exhibiting a structural transition from linear to branched micelles. At a given volume fraction, the viscosity of branched micelles are lower than that of linear micelles, as the branch points can slide along the length of the micelles, providing an additional mechanism for stress relaxation.

To understand the concentration scaling of the rheological parameters of CTAB–NaOL catanionic mixtures, linear and dynamic rheological measurements were performed on the mixed micelles as a function of concentration, at fixed x_{NaOL}. Variation of zero shear viscosity at three different mole fractions of sodium oleate, 0.1, 0.23, and 0.3, as a function of
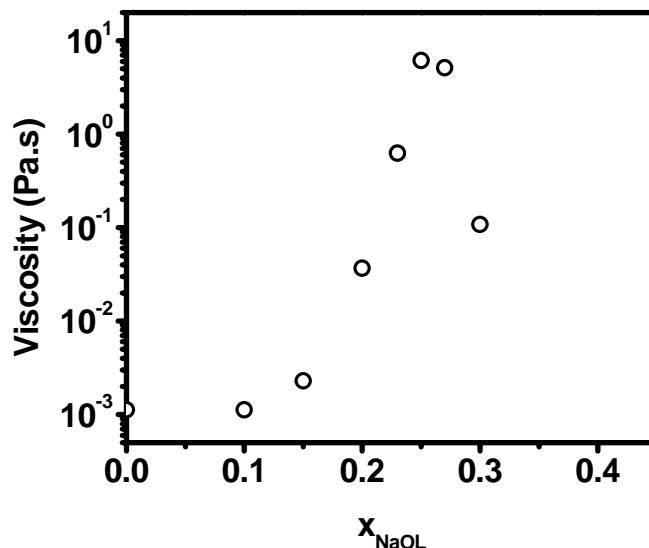
Figure 4.2 Variation of the zero-shear viscosity, η_0, of CTAB–NaOL mixed micelles with varying mole fraction of sodium oleate ($C_T = 0.1$ M).

volume fraction of micelles (φ) is depicted in Figure 4.3. The mole fractions of the mixed micelles are chosen such that the compositions span different regimes in the viscosity plot; viz. below, near and above the viscosity maximum. For x_{NaOL} 0.1, viscosity change is marginal at low φ values, suggesting very small growth and low number density of the mixed micelles. An increase in the viscosity occurs at $\varphi \approx 0.05$ and continues to increase in a linear manner. This increase in viscosity above a critical volume fraction indicates transition from dilute to semidilute regime of ellipsoidal micelles. In the semidilute regime, the viscosity varies linearly with the volume fraction. This observed linear scaling behavior indicates that

no structural transition has occurred in the studied concentration range. This suggests that for x_{NaOL} 0.1, short ellipsoidal micelles retain their structure with an increase in φ; with a mere increase in the number density of micelles. However, the behavior is different at higher mole fractions of sodium oleate, x_{NaOL} 0.23 and 0.3. At x_{NaOL} equal to 0.23, the viscosity increases even at low φ and a linear increase in the viscosity is observed only upto a particular value of φ, thereafter the viscosity decreases slowly. Occurrence of the semidilute regime even at low volume fraction indicates that the micelles are long. The decrease in viscosity at very high φ values indicates a transition from linear to branched micelles. This indicates that at this mole fraction, a slight change in concentration favors the formation of branched micelles and hence the viscosity decreases with concentration.
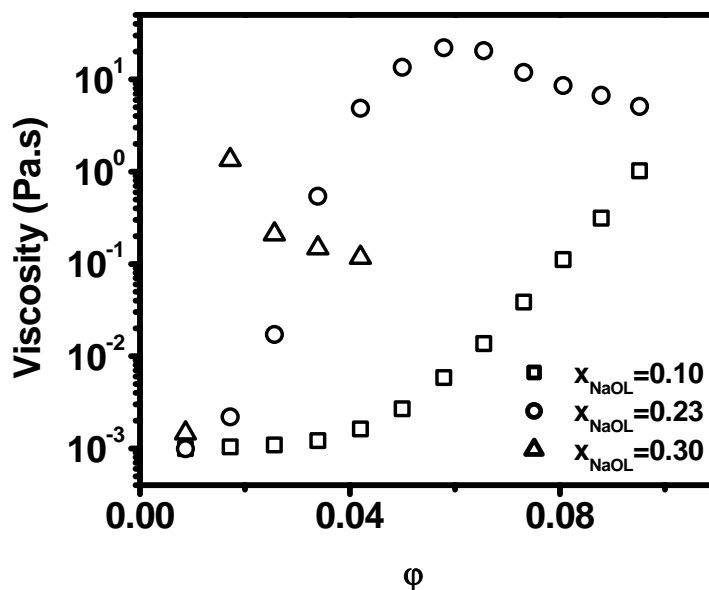
Figure 4.3 Variation of zero-shear viscosity of CTAB–NaOL mixed micelles as a function of micelle volume fraction (φ) at x_{NaOL} = 0.1, 0.23, and 0.3.

From the initial steady shear data, it is inferred that the mole fraction 0.23 is ideal to explore the scaling of rheological parameters of both linear and branched micelles, as it spans both

regimes. At low volume fractions mostly linear micelles are formed while at high volume fractions only branched micelles are favored.

Another feature in the rheology of worm-like micelles is their anomalous concentration dependence. Figure 4.4 depicts the shear dependent viscosity at a constant mole fraction of sodium oleate, x_{NaOL} 0.23 at different volume fractions of micelles (φ). At low φ, system shows Newtonian behavior. With increasing φ, catanionic mixture shows shear thinning behavior at large deformations. With further increase in φ, shear thinning occurs at lower shear rates and zero shear viscosity increases as already discussed above. At this mole
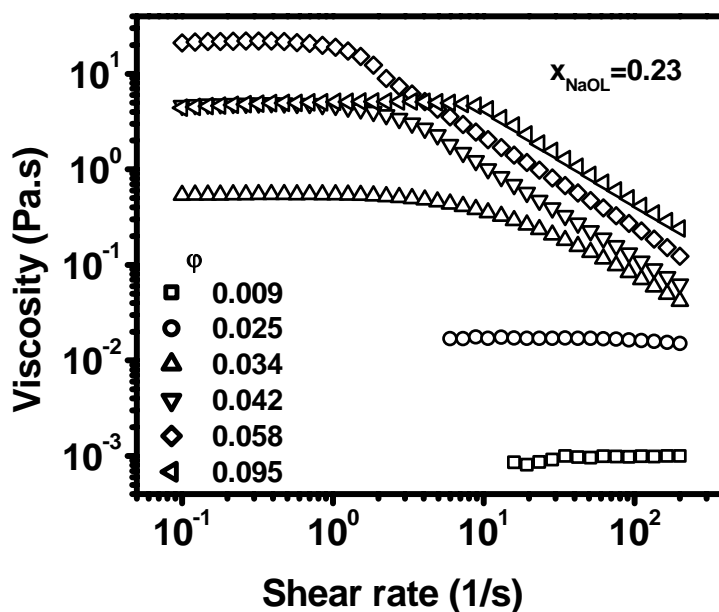
Figure 4.4 Shear viscosity versus shear rate for CTAB–NaOL mixed micelles with varying volume fraction of micelles (φ), at $x_{NaOL} = 0.23$.

 fraction, long polymer-like micelles are preferred to spherical micelles and the number density of the worm-like micelles increases with an increase in φ, forming a network structure. Network structure of the catanionic mixture is deformed by applying a shear, and

shear thinning occurs due to the alignment of aggregates under flow, if the deformation is faster than the time required for regaining equilibrium network structure. Also relaxation becomes slower with an increase in network structure, explaining shear thinning at lower shear rates. At large φ, CTAB–NaOL mixtures again start exhibiting shear thinning behavior at large deformations with a decrease in viscosity, suggesting the formation of branched micelle. Note that, here the linear to branched micelle transition is induced by a change in volume fraction of the micelles. With increasing φ, spontaneous interfacial curvature of aggregate decreases, increasing the energy cost for the formation of hemispherical end caps of the cylindrical micelles. The end cap energy can be minimized if the free ends of the cylindrical micelles fuse with cylindrical part of its own or other micelles, thus developing into branched worm-like micelles. When stress is applied, such micellar joints can slide along its cylindrical body (contour) thereby allowing a fast stress relaxation process. This is consistent with the recent report on sodium oleate-octyltrimethylammonium bromide (C_8TAB) mixtures by Chellamuthu *et al.* [141]. At a fixed molar ratio, 70/30 of NaOL to C_8TAB, the shear rheology measurements showed a maximum in shear viscosity at 4wt% followed by a sharp decrease in viscosity with increasing total surfactant concentration. With the help of cryo-TEM, it was concluded that the maximum in shear viscosity for these fluids corresponds to the transition from linear entangled to branched micelles. The branched micelles eliminate the strain hardening due to the ghost-like crossing of the two entangled worm-like micelles and the sliding of branch points along the length of a worm-like micelle.

The dynamic rheology of worm-like micelles has been explored in detail, in the past decades, both in linear and branched micelle regimes. The scaling exponents of the zero shear viscosity and the stress relaxation time show marked difference during transition from linear

to branched micelles. However, no significant changes in the scaling exponents of plateau moduli are reported so far. This is contrary to the reports on melt rheology of branched polymers, which suggest that the introduction of branching leads to a decrease in the plateau modulus. The limited concentration range over which branched micelles exists restricts precise determination of the scaling exponents in the branched micelle regime. In certain cases, identification of a well-defined plateau in the storage modulus becomes difficult due to overlap of Rouse mode. To investigate the scaling of rheological parameters in linear and branched regime, dynamic rheological measurements were performed on CTAB–NaOL catanionic mixtures with varying φ. All measurements were restricted to the mole fraction 0.23. Figure 4.5 shows the variation of storage and loss modulus, $G'and G''$ respectively, as a function of frequency ω, at total surfactant concentration of 100 mM and at 298 K. It can be
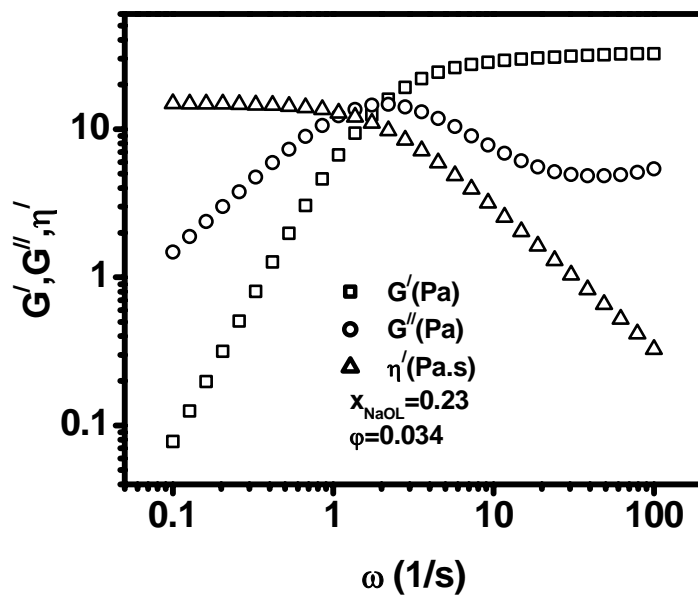
Figure 4.5 Variation of the storage modulus (G'), loss modulus (G"), and real part of the complex viscosity (η') as a function of frequency (ω) at 25 °C for a CTAB–NaOL mixture. The mole fraction of sodium oleate (x_{NaOL}) is 0.23, and the volume fraction of micelles (φ) is 0.034.

seen that the solution shows typical viscoelastic behavior, as G' varies as ω^2 and G'' varies as ω, at low frequencies. $G'(\omega)$ and $G''(\omega)$ crosses each other at an intermediate frequency, i.e. cross over frequency (ω_R). Assuming that the behavior is close to Maxwell model, the relaxation time and plateau modulus can be obtained from the values of modulus and frequency at the cross over point.

The stress relaxation time (τ_R) is obtained as the reciprocal of the cross over frequency while the plateau modulus can be taken as twice the value of the modulus at the cross over point. Figure 4.6 depicts the variation of τ_R with volume fraction (φ) of micelles.
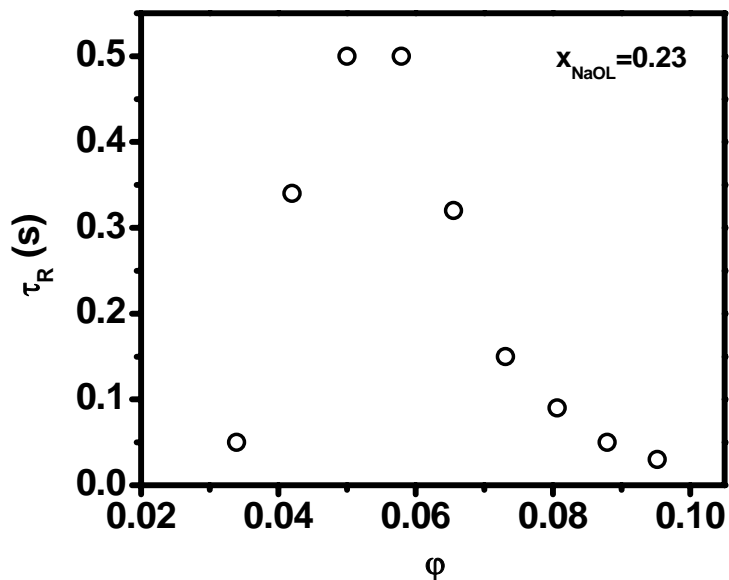
Figure 4.6 Variation of the stress relaxation time (τ_R) of CTAB–NaOL mixtures as a function of volume fraction of micelles (φ) at a fixed $x_{NaOL} = 0.23$.

With increasing φ, there is an increase in τ_R, followed by a maximum around $\varphi \approx 0.06$. With further increase in φ, τ_R decreases after reaching a maximum, indicating the structural transition to branched micelles as already discussed. A plot of log (G_0) as a function of log (φ) has been depicted in Figure 4.7. One can clearly identify two distinct regimes, consistent with

the linear and branched regimes as inferred from viscosity data. A linear plot is obtained upto

$\varphi \approx 0.05$ with a slope of 3.78. For $\varphi > 0.05$, the slope of the plot changes to 2.32. This clearly

suggests that the scaling exponents of G_0 for linear and branched micelles are significantly

different. A schematic representation has also been presented in Figure 4.8. Moreover, the

exponent for branched micelles is lower than that of linear micelles, as is the case with

polymer melts.
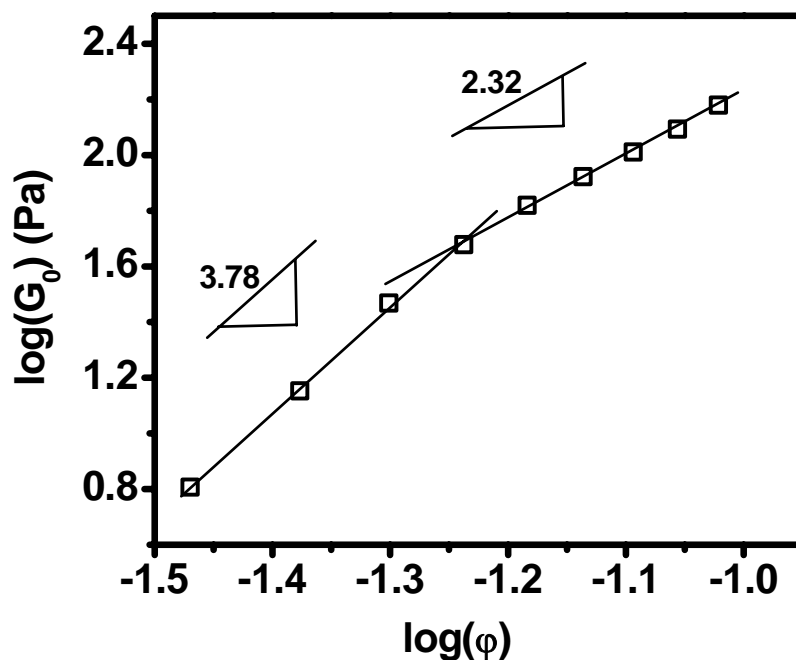
Figure 4.7 Variation of logarithm of the plateau modulus (G_0) as a function of logarithm of volume fraction of CTAB–NaOL micelles (φ), at a fixed $x_{NaOL} = 0.23$. A change in the slopes of the graph indicates change in the scaling exponent.
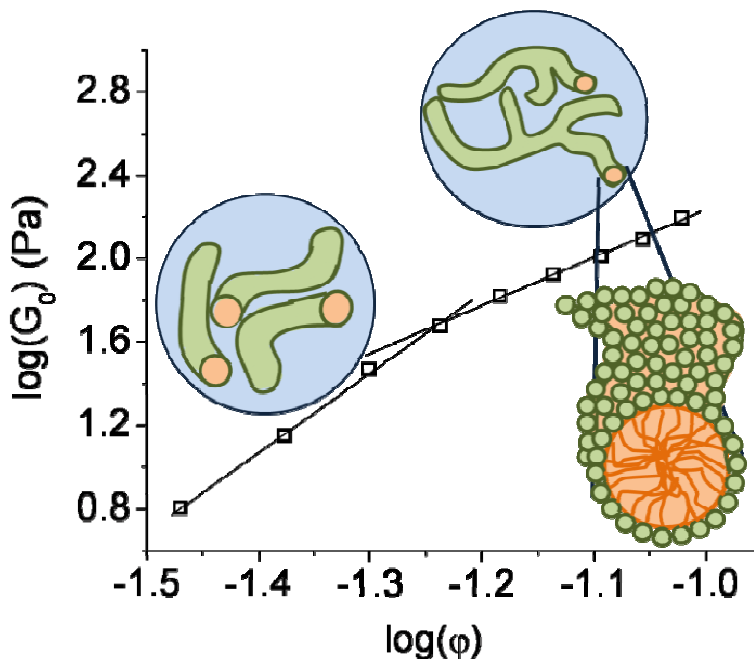
Figure 4.8 Schematic representation of scaling behavior with structural transition in CTAB–NaOL micelles.

Figure 4.9 shows the variation of *G′* and *G″*, in the form of Cole-Cole plots, (at different φ) and attempts were made to fit the data using Maxwell model employing G_0 and τ_R reported above. It was found that at low frequencies the Maxwell model fits reasonably well to the data (fit not shown). However, at high frequencies the plateau modulus deviates from the value expected from Maxwell model. Alternately, the exact value of plateau modulus can be obtained from an extrapolation of the Cole-Cole plot to the x-axis, as shown in Figure. The variation of   , obtained by such an extrapolation also shows different scaling exponents in the two regimes, negating the possibility of biased errors in the estimation. From   , entanglement length (l_e) for the flexible micelles can be calculated using equation 4.6.
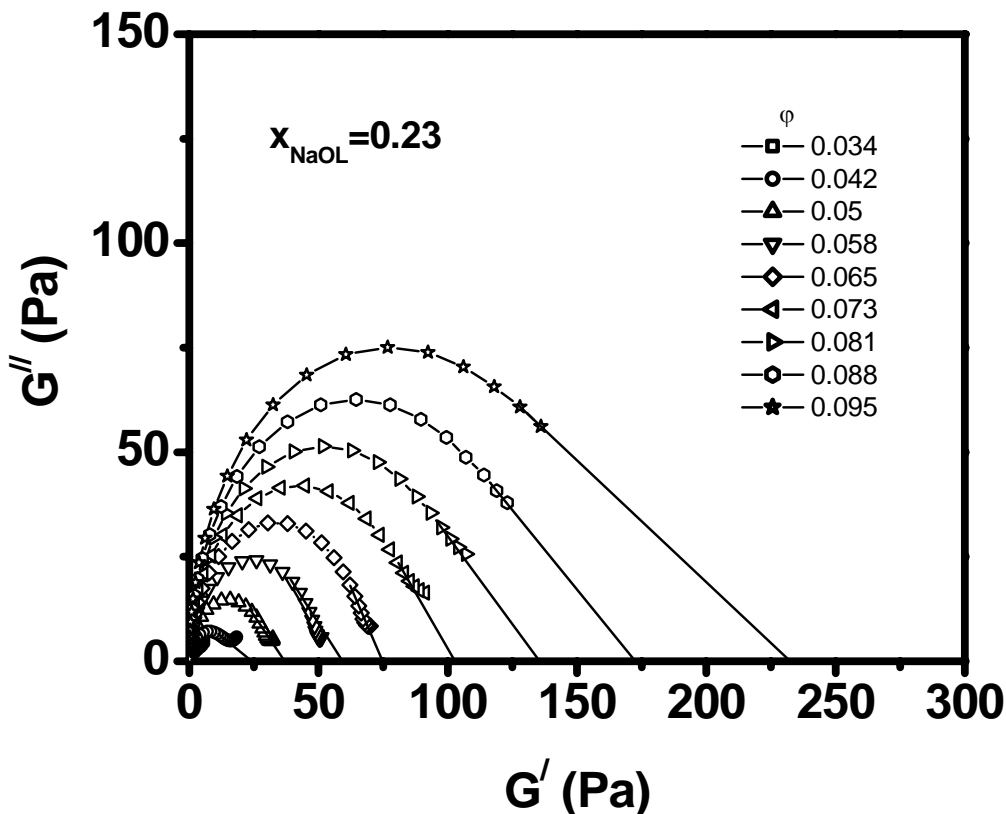
Figure 4.9 Variation of loss modulus (G") as a function of storage modulus (G') at different volume fractions of CTAB–NaOL micelles (φ) at a fixed x_{NaOL} = 0.23. The solid lines show an extrapolation of the high frequency data to obtain G'$_\infty$.

Figure 4.10 depicts entanglement length, l_e as a function of the volume fraction of micelles, φ, assuming the value of persistence length of the CTAB–NaOL micellar system to be 200 Å [133]. It can be observed that the slope of the graph changes with the structural transition from linear to branched micelles, which is in line with G_0 vs φ graph. This also supports our study of changes in the scaling behavior of the rheological parameters with the structural transition in the micellar system.
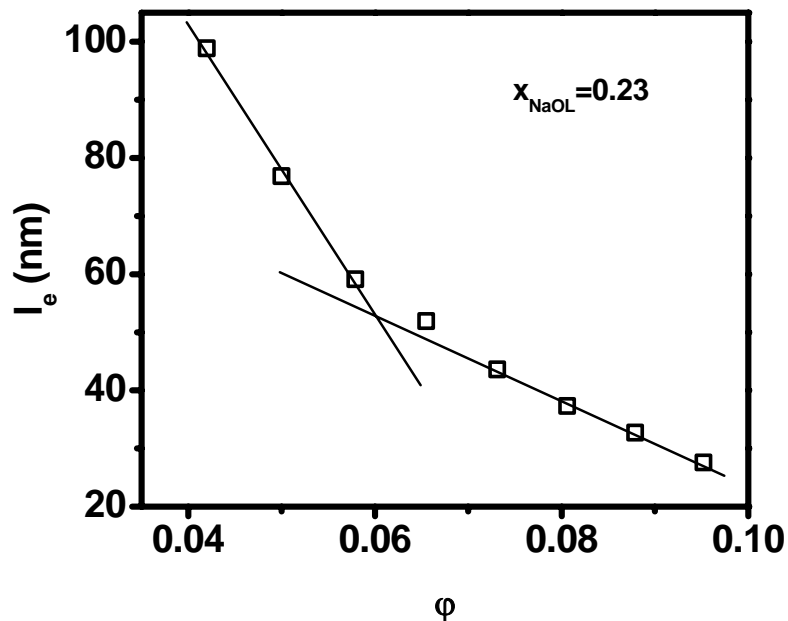
Figure 4.10 Variation of entanglement length (l_e) as a function of volume fraction of CTAB–NaOL micelles (φ), at a fixed $x_{NaOL} = 0.23$.

Recently the scaling behavior of different worm-like mixed micelles, including sodium decanote (SD)/CTAB, sodium laurate (SL)/CTAB, sodium didecaminocystine (SDDC)/CTAB, and sodium dilauraminocystine (SDLC)/CTAB, has been investigated by Fan *et al.* and compared the results with Cates model [58]. It has been shown that the scaling behavior is influenced by the surfactant structure and the mixing ratios. Such behavior is mainly due to the electrostatic interactions between the worm-like micelles i.e. the charge density of worm-like micelles, regardless of the surfactant structure. Cates model is applicable when the charge density of the worm-like micelles is below a threshold value, regardless of the possible changes in the chain packing. The presence of electrostatic interactions can significantly affect the scaling exponents. The preparation and structure-property behavior of linear and branched thermoplastic poly (urethane urea)s (TPUU) and polyureas with different soft segments have been investigated. A comparison of the rheological behavior of linear and

branched polymers suggests that the hyperbranched polymers show a lower plateau modulus as compared to linear polymers [142].

4.4 Micellar growth in CTAB-NaOL mixtures

The growth of micelles by the addition of oppositely charged additives or electrolytes can be quantified from small angle neutron scattering (SANS) measurements. SANS is an ideal tool to assess the structural polymorphism in surfactant assemblies due to the large scattering contrast that can be achieved by using deuterated solvents. Though the linear and branched micelles cannot be differentiated from the SANS analysis, the structural evolution from spherical to elongated micelles can be assessed in a quantitative manner by SANS analysis. SANS spectra of mixed micelles at different mole fractions of sodium oleate, x_{NaOL}, at a total surfactant concentration of 100 mM, are depicted in Figure 4.11. SANS spectrum of
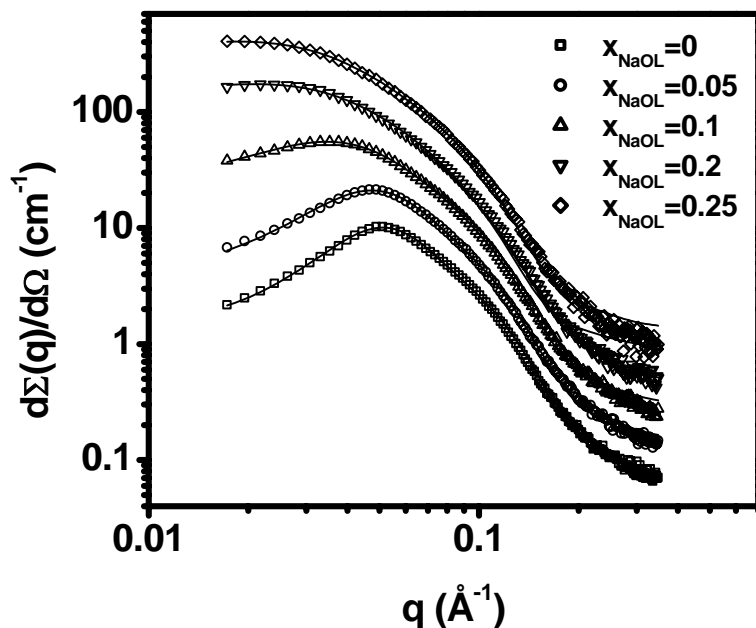
Figure 4.11 SANS spectra for CTAB–NaOL mixtures (C_T = 0.1 M) at different mole fractions of sodium oleate. The data for x_{NaOL}=0 are absolute values while the remaining plots are offset by a factor of 2 for clarity. The solid lines are fit to the data using a model for charged ellipsoids, as discussed in the text.

pure 100 mM CTAB solution shows a characteristic correlation peak at intermediate q, indicating electrostatic interaction between the micelles as they are positively charged. It can be observed that the correlation peak broadens and shifts to lower q values with an increase in x_{NaOL}, indicating a decrease in the range of electrostatic interactions. Also with increasing x_{NaOL}, the scattering intensity increases at low q, suggesting a growth in the micellar structure. To obtain structural parameters of the micelles, the SANS spectra were modeled as charged prolate ellipsoids interacting through a screened Coulomb potential [92]. Fractional charge, semimajor axis, and semiminor axis are used as the variables in the fit. In order to obtain good fit, a polydispersity parameter $z = 35$ was used in the semimajor axis and is included using Schultz distribution in all the samples. The aggregation number was calculated using Tanford formula. The experimental data fits reasonably well with the model and the parameters of the fit are summarized in Table 4.1. With an increase in x_{NaOL}, the axial ratio of the micelles increases and the fractional charge decreases, suggesting the growth of CTAB–NaOL mixed micelles from spherical to rod-like micelles.

Table 4.1 Micellar parameters obtained from the SANS analysis of 0.1 M CTAB–NaOL mixed micelles with varying mole fraction of sodium oleate.

S.No.	Mole fraction of sodium oleate (x_{NaOL})	Aggregation number (N_{agg})	Fractional charge (α)	Semiminor axis, b (Å)	Semimajor axis, a (Å)	Axial ratio
1	0	157	0.14	21.4	49.3	2.3
2	0.05	188	0.09	22.4	53.9	2.4
3	0.1	335	0.01	23.2	88.1	3.8
4	0.2	497	0.01	26.4	96.3	3.6
5	0.25	947	0.01	25.6	199.9	7.8

Changes in the microstructure of CTAB micelles upon addition of sodium oleate, have also been probed by dynamic light scattering. Figure 4.12 depicts the apparent hydrodynamic radius (R_h) of CTAB–NaOL catanionic mixture as a function of increasing mole fraction of sodium oleate, x_{NaOL}. Apparent hydrodynamic radius, deduced using Stokes-Einstein equation, increases with increasing x_{NaOL}. At low x_{NaOL}, R_h is consistent with the value of that of spherical micelles. However, with an increase in x_{NaOL}, the equivalent sphere diameter of the micelles increases and it reaches a value inconsistent with the alkyl chain length of the surfactant, suggesting growth of the globular micelles to form anisotropic aggregates. Catanionic micelles can grow either as disk-like (oblate) or rod-like (prolate) micelles. Rheology and SANS have already indicated the structural transition from spherical to rod-like micelles. From the measured diffusion coefficient of the micelles, the micellar length (L) is estimated, using the Perrin's relation (Figure 4.12). With the variation of x_{NaOL} from 0 to 0.27, length of the micelles varies from a few nanometers to about 35 nm. At small x_{NaOL}, L could not be analysed using the above relationship, suggesting that the axial ratio is smaller than 4.
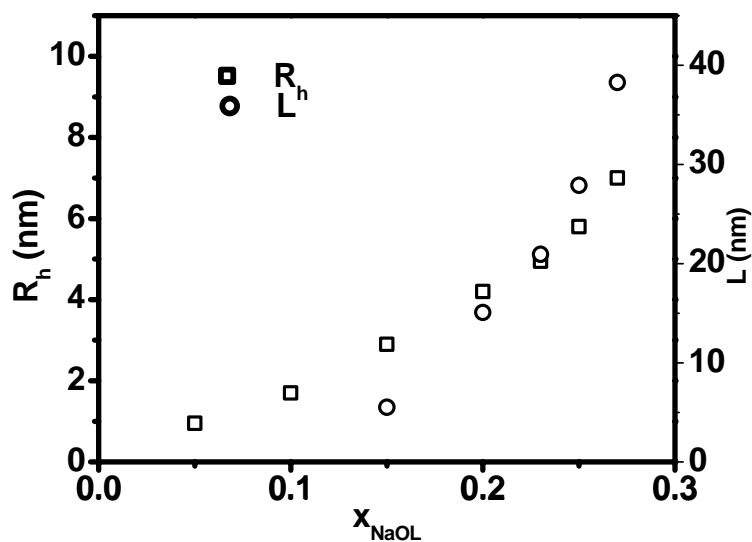
Figure 4.12 Variation of apparent hydrodynamic radius (R_h) and micellar length (L) of CTAB–NaOL mixed micelles ($C_T = 0.1$ M) at different mole fractions of sodium oleate.

4.5 Effect of electrolytes on growth behavior

Though the observed deviation in the scaling exponent of plateau modulus, at high surfactant concentration, occurs at a concentration where branched micelles are formed, the possibility of changes in the electrostatic interactions or flexibility of the micelles cannot be ruled out. This is because of the fact that increase in the concentration of surfactants leads to an increase in the counterion concentration and hence can affect the growth behavior due to the variation in the ionic strength of the medium. This effect is more pronounced when the surface charge of the micelles is rather high. Hence the effect of ionic strength on these mixed micelles using NaCl as the electrolyte has been investigated. SANS spectra for NaOL–CTAB mixed micelles, at constant x_{NaOL} of 0.05 (C_T =100 mM), with varying concentration of NaCl is shown in Figure 4.13. Considering the fact that small amount of counterion variation will
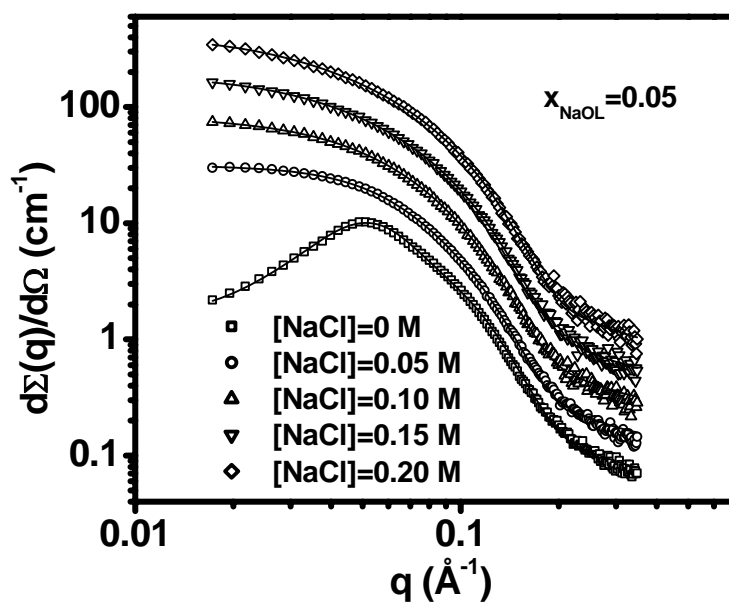
Figure 4.13 SANS spectra for CTAB–NaOL mixed micelles at a fixed x_{NaOL} = 0.05 and varying concentration of NaCl. The spectra of x_{NaOL}=0.05 in the absence of NaCl are absolute values while the remaining plots are offset by a factor of 2 for clarity. The solid lines are fit to the data using ellipsoidal micelles.

118

have little effect on neutral micelles, the mole fraction of mixed micelle was kept at 0.05 so that the micelles do remain as charged. In the absence of NaCl, the spectrum shows a correlation peak, indicating the presence of repulsive intermicellar interaction between the catanionic micelles, arising due to a net positive charge on the micelles. With the addition of NaCl, the correlation peak is less pronounced, which indicates interparticle interaction between the micelles is negligible. The added electrolyte has effectively screened the electrostatic repulsion. With increasing NaCl concentration, forward scattering also increases, suggesting growth of the micelles. As intermicellar interaction is relatively weak in the presence of NaCl, the model independent IFT method has been employed, to assess the structural changes. The IFT method allows us to evaluate the pair distance distribution function (PDDF), $p(r)$, of the micelles. Variation in the $p(r)$ function of the micelles with increasing NaCl concentration is depicted in Figure 4.14. The PDDF of mixed micelles
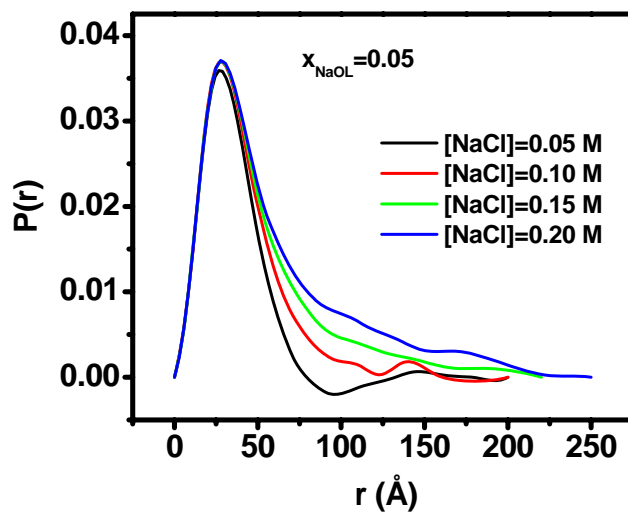
Figure 4.14 PDDFs (obtained from the IFT analysis of the SANS spectra) of CTAB–NaOL mixed micelles at a fixed $x_{NaOL} = 0.05$ ($C_T = 0.1$ M) and varying concentration of NaCl.

composed of x_{NaOL} of 0.05 ($C_T = 100$ mM), in the low electrolyte concentration shows the influence of structure factor, $S(q)$, (though weak), as indicated by a weak oscillation in $p(r)$.

119

With increasing the NaCl concentration of the mixed micelles, this oscillation disappears and the micelles continuously transform into short rods with increasing average length. Based on the structural information obtained from IFT analysis, the SANS data were fitted using a prolate ellipsoid model. In the presence of NaCl, no interparticle interaction is taken into account. The experimental data fits reasonably well with the model and the parameters of the fit are summarized in Table 4.2.

At low salt concentration, the axial ratio of the micelles increases with increasing electrolyte concentration, as salt produces the screening effect in the catanionic mixture. It should be noted that the growth of the catanionic mixture is very large when the mole fraction of sodium oleate is increased compared to the growth of the catanionic mixture with increasing electrolyte concentration. Once the interactions are screened, further addition of

Table 4.2 Micellar parameters obtained from the SANS fit for 0.1 M CTAB–NaOL mixed micelles with varying NaCl concentration at a fixed mole fraction of sodium oleate (x_{NaOL} = 0.05).

S.No.	[NaCl], (M)	Aggregation number (N_{agg})	Fractional charge (α)	Semiminor axis, b (Å)	Semimajor axis, a (Å)	Axial ratio
1	0	188	0.09	22.4	53.9	2.4
2	0.05	279	0.01	22.6	78.6	3.5
3	0.1	278	0.01	22.6	77.6	3.4
4	0.15	313	0.01	22.0	92.2	4.2
5	0.2	345	0.01	21.6	105.9	4.9

NaCl produces very little changes in the aggregation number. This suggests that the effect of electrolytes on neutral micelles is negligible and hence the observed changes in the shear

modulus arise mainly from branching of the micelles. Addition of non penetrating counterions like NaCl results in small growth of the catanionic mixed micelles, due to the screening effect or by decreasing the charge density of the micelles. But the addition of penetrating Oleate (OL^-) ion binds strongly to the CTA^+ ions and hence the growth is in the form of giant worm-like micelles. Recently Gokul *et al.* has compared the growth behavior of NaOL in the presence of a binding salt (triethylammonium chloride, Et_3NHCl) and simple salt (potassium chloride, KCl). Both salts promote the growth of micelles. Simple salt like KCl showed a growth of the micelles from spherical to worm-like micelles but binding salt like Et_3NHCl also modifies the phase behavior of NaOL solution. There is cloud point behavior in solutions of NaOL and Et_3NHCl, attributed to the onset of attractive interactions between the anionic micelles at high temperatures due to strong binding of the counterions [143]. The contour lengths and flexibility of long micelles are greatly influenced by the chemical structure of the additives. The role of electrostatic and specific ion binding in tuning the contour lengths and the flexibility of the mixed micelles of cetyltrimethylammonium 2,6-dichlorobenzoate and cetyltrimethylammonium chloride as a function of surfactant and salt concentrations has been reported by Magid *et al.* Addition of highly hydrated, non penetrating electrolyte like NaCl salt will form small and globular micelles over a wide range of surfactant and salt concentrations. However, addition of less hydrated, penetrating counterions like 2,6-dichlorobenzoate form giant worm-like micelles even at low concentrations of hydrophobic counterions. Increasing the composition of penetrating counterions of the catanionic pair, lower the 1D bending modulus of the micelles and increase their flexibility [144]. However, the effect of these parameters on shear modulus appears to be minimal and the observed variation in shear modulus clearly suggests different scaling for linear and branched micelles.

4.6 Vesicle formation in CTAB-NaOL mixtures

In the catanionic system, an aggregate structure of considerable interest is spontaneously formed vesicles. Unilamellar vesicles are aqueous compartments enclosed by a single bilayer membrane with both polar ends facing the aqueous medium, mimicking the type of structures encountered in phospholipids. Since Kaler *et al.* [145] gave the example of spontaneous vesicle formation from mixed cationic and anionic single-chained surfactants using cetyltrimethylammonium tosylate (CTAT) and sodium dodecylbenzenesulfonate (SDBS), the isothermal ternary phase diagrams of some cationic surfactant–anionic surfactant–H2O (or D2O) systems have been constructed by using several techniques including NMR, imaging, and scattering methods [145-151]. Spontaneous vesicle formation, driven primarily by the electrostatic interactions of the oppositely charged head groups of surfactants, is dependent on the molecular geometry of the surfactants and hydrocarbon chain asymmetry of the surfactant pair used in the catanionic mixture [152]. Thermodynamically stable, unilamellar vesicles are usually observed in solutions where one of the surfactants, usually the shorter chain surfactant, is in excess. Vesicles are stabilized by the excess charge while chain asymmetry favors spontaneous curvature through favorable packing distribution of the individual surfactants in the monolayers [149, 151].

These equilibrium vesicles have emerged as attractive candidates for a broad range of applications such as encapsulation and as potential vectors for biological compounds [153-155] and material synthesis [156-158]. From long past they have been utilized in the encapsulation and cellular delivery of probes, drugs, and DNA in pharmacology, medical diagnosis, and cosmetics, to cite but a few applications, owing to their ability to entrap both hydrophilic and hydrophobic cargos [159-164]. This interest stems mainly from their

spontaneous formation and long term stability, when compared to most lipidic vesicle formulations [165]. Theoretical work concerning the stability and topology of vesicles based on flexible surface [165-170], molecular geometry [171, 172], or thermodynamic [173, 174] models has also attracted early and renewed interest.

A detailed study on the mixture of cetyltrimethylammonium bromide (CTAB) and sodium oleate (NaOL) indicates interesting phase behavior when the mole fraction of anionic surfactant (x_{NaOL}) is varied in the catanionic surfactant mixture, keeping the total surfactant concentration (C_T) at 300 mM. For making the discussion simple, the phases have been divided into different regions and the rich variety of phase behavior is evident from the photographs of representative samples from different regions (different mole fractions of sodium oleate) as shown in Figure 4.15. From pure 300 mM CTAB solution to x_{NaOL} =0.23 (C_T = 300 mM) (region 1), the catanionic surfactant solution is clear and isotropic. This represents the region where either spherical or worm-like micelles have been observed. In the range of x_{NaOL} 0.23-0.37 (region 2), the solution exhibits birefringence when observed under crossed polaroids as shown in Figure 4.16, indicating the formation of anisotropic structures with orientational order. Such liquid crystalline phases can be formed by the alignment of rod-like aggregates, as in the case of nematic liquid crystals. Figure 4.17 (a) and (b) depicts the polarized optical microscopic images of the birefringent phase (x_{NaOL} = 0.3), at a total surfactant concentration of 300 mM, when viewed under parallel and perpendicular polarization, respectively. The possibility of forming other liquid crystalline structures such as lamellar phases cannot be neglected. However, no attempts were made to characterize the liquid crystalline phases. With further increase in x_{NaOL} from 0.38-0.45 (region 3), the solution turns turbid and the turbidity increases with increase in x_{NaOL}. These turbid solutions show

good colloidal stability and form a bluish translucent liquid upon dilution. This is a clear indication of formation of vesicles. From x_{NaOL} 0.46-0.68 (region 4), the solution separates

Figure 4.15 Representative photographs of samples indicating different phases in CTAB–NaOL mixed surfactant system. The numbers on the top of the samples represent different regions as explained in the text.

into two phases; a turbid colloidal solution in equilibrium with an excess of precipitate. This precipitate could be the insoluble catanionic salt. Further in the range of x_{NaOL} 0.69-0.74
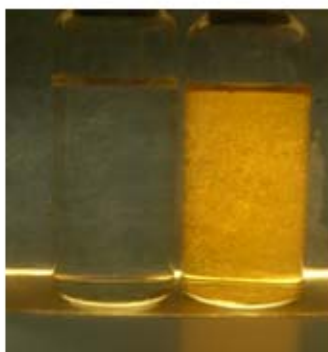
Figure 4.16 Images representing the non-birefringent and birefringent phases fromed in CTAB–NaOL mixed micelles as observed using a crossed polarizer, at (a) x_{NaOL} = 0.1 and (b) x_{NaOL} = 0, keeping C_T = 0.3 M.

(region 5), again a turbid phase appears that increases with increasing x_{NaOL}. This is very similar to the reported results on other catanionic mixtures where two vesicle phases exist on either side of the equimolar ratio. Again, the solution separates into two phases in the range of x_{NaOL} 0.75-0.95 (region 6). As the mixture becomes rich in anionic surfactant, the solution again turns clear for x_{NaOL} 0.96-1 (region 7). Here, we restrict our microstructural studies to the vesicle phases only (region 3 and 5).
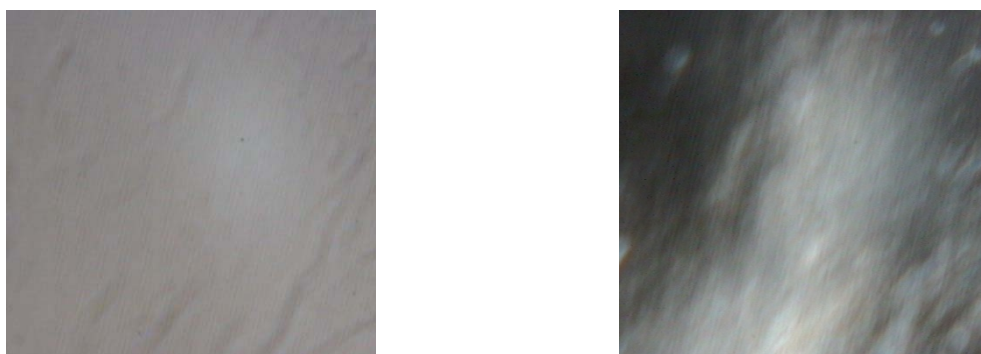
Figure 4.17 Polarized optical micrographs of CTAB-NaOL mixture at $x_{NaOL} = 0.3$ ($C_T = 0.3$ M) (a) parallel polarization and (b) perpendicular polarization.

4.6.1 Characterization of vesicle phases by DLS and Zeta potential

As concluded from the phase behavior study discussed above, region 3 and 5 contain stable vesicles at room temperature of 25 ^{0}C. Figure 4.18 depicts the apparent hydrodynamic diameter (D_h) of catanionic vesicles formed in region 3, diluting to a total surfactant concentration of 1.2 mM from the total surfactant concentration of 300 mM, to avoid multiple scattering from vesicles, and equilibrated at a temperature of 50 ^{0}C for 30 minutes. DLS results show that region 3 contains vesicles of hydrodynamic diameter of 250 nm. Similarly Figure 4.19 depicts the apparent hydrodynamic diameter of catanionic vesicles formed in

region 5, diluting to a total surfactant concentration of 0.16 mM from 300 mM and equilibrated at 50 ^{0}C for 30 minutes. DLS results show that region 5 contains catanionic vesicles of average hydrodynamic diameter of 200 nm. Region 3 is rich in cationic surfactant CTAB, hence the anionic oleate surfactant solubilizes into CTAB micelles to form catanionic vesicles with excess CTAB and region 5 is rich in anionic surfactant, therefore in this region, cationic CTAB gets solubilized into oleate micelles to form catanionic vesicles with excess NaOL. Further zeta potential studies were performed on the same samples.
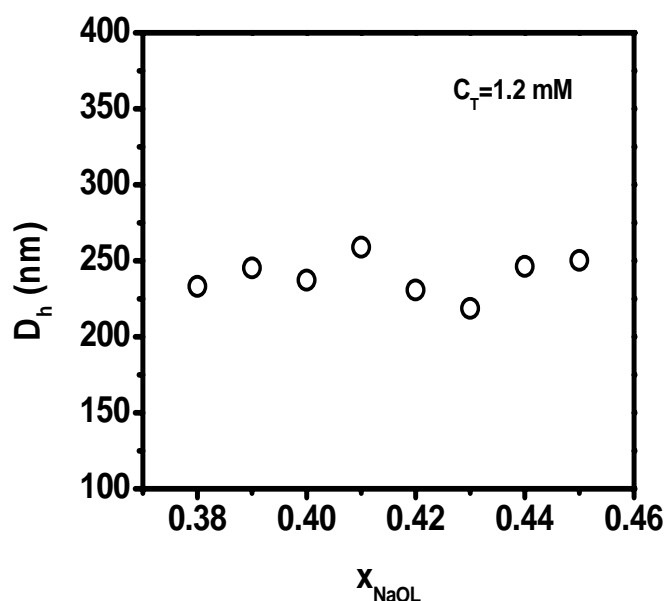
Figure 4.18 Variation of apparent hydrodynamic radius of CTAB–NaOL mixed micelles (C_T = 1.2 mM) at different mole fractions of sodium oleate.

Figure 4.20 depicts the zeta potential distribution of the catanionic vesicles formed in region 3 and 5. The catanionic vesicles present in region 3 show a zeta potential of +52 mV and the catanionic vesicles formed in region 5 show a zeta potential of -13 mV. It can be concluded that the vesicles in region 3 is net positively charged, as concentration of CTA^+ ion is more in the catanionic vesicles, whereas vesicles in region 5 is net negatively charged due to the presence of more of OL^- ion in the catanionic vesicles.

126
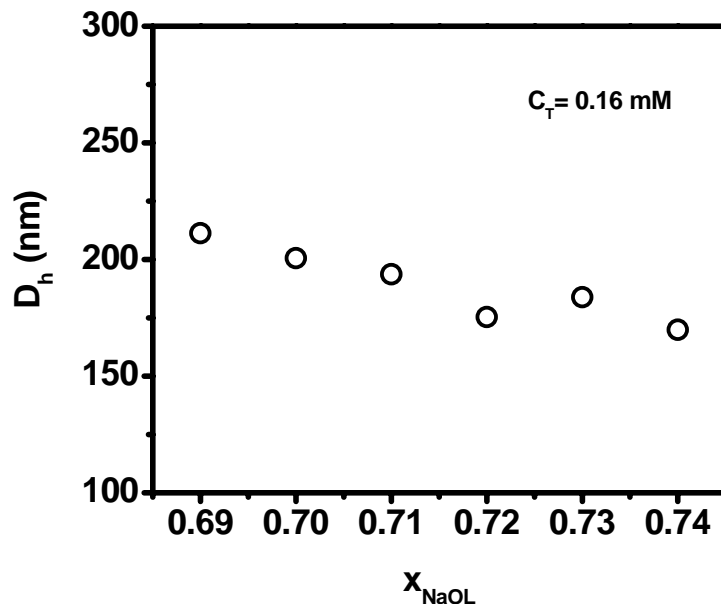
Figure 4.19 Variation of apparent hydrodynamic radius of CTAB–NaOL mixed micelles (C_T = 0.16 mM) at different mole fractions of sodium oleate.
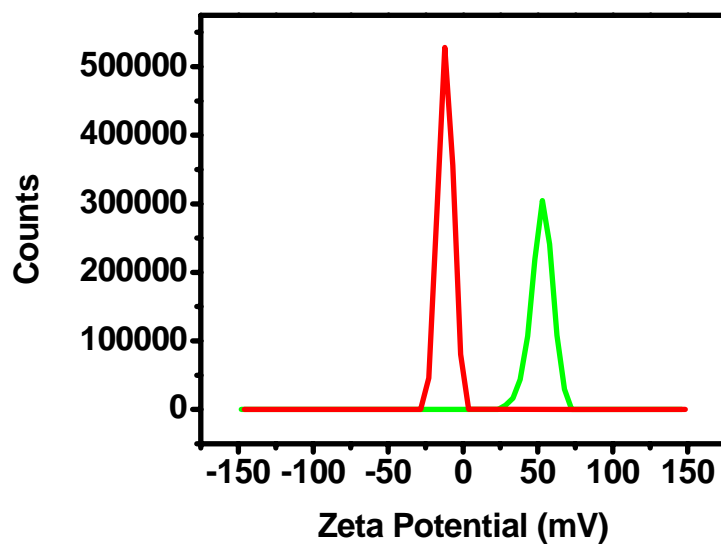
Figure 4.20 Intensity versus zeta potential plot for CTAB–NaOL mixed micelles at x_{NaOL}= 0.39 (C_T = 1.2 mM) and at x_{NaOL} = 0.73 (C_T = 0.16 mM).

The bilayer structure of the vesicles can be assessed from SANS measurements as well. Figure 4.21 depicts the SANS spectra for catanionic vesicles of x_{NaOL} = 0.41 and 0.72 at

a total surfactant concentration of 300 mM. For both the SANS spectra, the characteristic

feature of the scattering curve is two sets of damped oscillations with a $I \sim q^{-2}$ envelope at
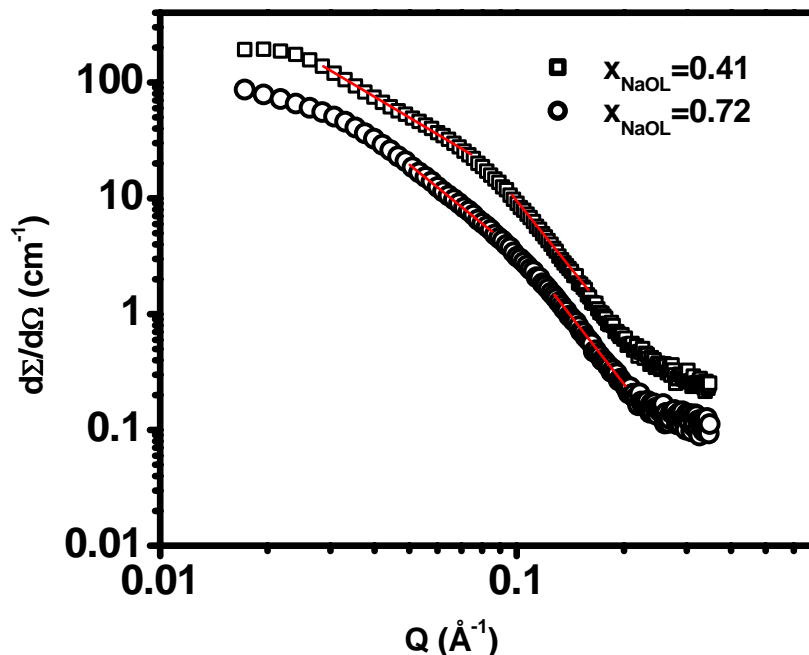
Figure 4.21 SANS spectra for CTAB–NaOL mixtures at $x_{NaOL} = 0.41$ and 0.72, keeping $C_T = 300$ mM. The spectra of $x_{NaOL} = 0.72$ are absolute values while the plot of $x_{NaOL} = 0.41$ is offset by a factor of 2 for clarity.

intermediate q, and a $I \sim q^{-4}$ Porod envelope at large q. This behavior is characteristic for

hollow spherical structures such as vesicles [175-177].

4.7 Conclusion

The rheological behavior of CTAB─NaOL mixed micelles over a wide concentration

range exhibiting both linear and branched micelles has been studied. The aim of the study is

to understand the scaling behavior of linear and branched micelles and identify if there is any

difference in the scaling exponents, as in the case of polymers. Due to the presence of a long

hydrocarbon chain with an unsaturated bond in anionic oleate moiety, CTAB─NaOL mixtures form viscoelastic fluids over a wide range of composition and concentration. Hence, under appropriate conditions, linear or branched worm-like micelles are formed in CTAB-NaOL mixtures, without precipitation of the catanionic salt. Small angle neutron scattering, dynamic light scattering and rheological measurements suggest the microstructural transition from sphere to rod-like to worm-like micelles with an increase in the mole fraction of sodium oleate in the CTAB─NaOL mixed micelles. Steady flow rheological measurements indicate Newtonian behavior when the axial ratio of the micelles is small, while non-Newtonian (shear thinning) behavior is observed when the micelles are long enough to form entangled structures. Dynamic rheology of the entangled micelles is similar to Maxwell fluids, which is one of the basic models for a viscoelastic fluid. According to Cates *et al.*, the rheological behavior of worm-like micelles follows simple scaling laws. Concentration dependence study of CTAB─NaOL mixed micelles at a fixed mole fraction of sodium oleate (x_{NaOL}=0.23), has shown that the exponents in the scaling laws change when the structural transition occurs from linear to branched micelles. The slope in the graph of plateau modulus vs volume fraction of the CTAB-NaOL micelles change from 3.78 to 2.32, when the structural transition occurs from linear to branched micelles. This is different from what is predicted by Cates and others. Most of the reports on worm-like micelles suggested a constant scaling exponent for linear and branched micelles, and no attempts have been made so far to account for any changes in the shear modulus of linear and branched micelles. The present studies indicate that the scaling exponents for branched micelles of the catanionic surfactant system agrees well with the values predicted by theoretical models, while for linear micelles an increase in the exponent is observed. Also slope of the plot of entanglement length vs volume fraction of

the micelles show an abrupt change in the linear to branched micelle regime. This rheological behavior of the mixed micelles is analogous to the polymer melts, as previous studies report that a comparison of the rheological behavior of linear and branched polymers suggests that the hyperbranched polymers show a lower plateau modulus as compared to linear polymers. Also, a detailed phase behavior study of CTAB-NaOL mixed micellar system has shown various interesting phases including a birefringent phase and two vesicular phases at two different regions of the phase diagram. Zeta potential studies have indicated the presence of oppositely charged vesicles at these two different regions of the phase diagram. The explanation for such behavior is given as in the region that is rich in cationic surfactant CTAB, the anionic oleate surfactant solubilizes into CTAB micelles to form net positively charged catanionic vesicles and in the region where anionic surfactant is more, cationic CTAB gets solubilized into oleate micelles to form net negatively charged catanionic vesicles. SANS studies indicated the presence of vesicles at these two regions.

CHAPTER 5

Dilution induced

structural transition in

mixed micelles

5.1 Introduction

In recent years, investigation on the mixed micellar systems of ionic surfactants and oppositely charged hydrophobic molecules have gained a lot of attention due to their applications as heat-transfer fluids, drag reduction agents, fracturing fluids in oil fields, personal care products, and templates for material synthesis [178-181]. The hydrotropes are mildly surface active and tend to self-aggregate and coaggregate with other organic compounds. The organic hydrotrope show very complex cooperative interactions by binding strongly to the micellar surface due to the electrostatic interaction and the hydrophobic effect of the counterion, often penetrating it [182, 183]. Similar to catanionic surfactant mixture, complex structures such as, elongated micelles, vesicles, liquid-crystalline phases, nanodisks, etc., can be formed by changing the composition of cationic to hydrotrope ratio. The structural changes in such mixtures arise due to a delicate balance of the various noncovalent forces that drive the self-assembly process. Hence, the addition of an organic hydrotrope to cationic micelles facilitates the transition from spherical to rod-like to worm-like micelles, quantitatively explained in terms of the geometrical packing parameter, p, as explained earlier for catanionic surfactant mixtures.

Since hydrotropes are structurally similar to surfactants, their combination with long alkyl chain trimethylammonium salts can be viewed as a mixed surfactant system. A number of organic hydrotropes such as sodium salicylate, sodium p-toluene sulphonate, alkyl sulphates and sodium 3-hydroxy naphthalene 2-carboxylate have been studied in combination with cationic surfactants. Elongated flexible micelles have been observed in aqueous solutions of cationic surfactants such as alkyltrimethylammonium surfactants with different binding organic counterions and were investigated in detail by techniques such as light scattering

[184, 185], NMR [186, 187], flow birefringence [188-190], electron microscopy [191, 192] and rheology [193, 194]. Subtle changes in the surfactant geometry, counterion, and added electrolyte alter the dimensions, flexibility, and interaction of the micelles. Such control of micellar structure is very useful in drug delivery vehicles and as templates for nanostructures [66].

Interaction of hydrobhobic salt sodium 3-hydroxynaphthalene 2-carboxylate (SHNC) with long chain alkyl trimethylammonium surfactants has been studied by many research groups. Recently Gunjan *et al.* has reported the microstructural transition of cetyltrimethylammonium bromide (CTAB)-SHNC mixed micellar system in the hydrophobe rich region. With dilution the microstructural transition occurs from spherical to rod-like to vesicles at a fixed weight ratio of hydrotrope to surfactant (85:15) [195]. The explanation for micelle to vesicle transition rests on the assumption that upon dilution, desorption of SHNC from CTAB–SHNC mixed micelles takes place, which in turn decreases the surface charge density on mixed micelles. Such observations have immense importance in the pharmaceutical industries and for thickening purposes. Flowable cleansing liquids has been formulated using high levels of anionic and nonionic surfactants and that show a substantial increase in viscosity upon dilution with water [196]. A local anaesthetic formulation comprising block copolymer micelles displays in situ gelation upon dilution with water due to the transition from an isotropic low viscosity fluid to a high viscosity hexagonal phase [197].

An investigation on the growth of decyltrimethylammonium bromide (DTAB) micelles in the presence of cationic hydrotrope SHNC with the dilution effect has been done. The aim of this study was to understand whether similar structural transition occurs in the surfactant rich side of DTAB–SHNC mixed micelles. As it is reported that the desorption of

hydrotrope owing to its low hydrophobicity is responsible for the structural transition, an exploration of the same has been done using DTAB as the surfactant which has low hydrophobicity and high CMC compared to other cationic surfactants in the homologous series. Thus, it is anticipated that such dilution induced changes can be found in the surfactant rich side, if the surfactants have low hydrophobicity as in the case of hydrotropes. The microstructural changes have been investigated using dynamic light scattering (DLS), Small angle neutron scattering (SANS), and cryo-TEM.

5.2 Dilution induced structural transition in DTAB-SHNC mixture

5.2.1 DLS studies

Firstly, changes in the microstructure of decyltrimethylammonium bromide (DTAB) micelles upon addition of sodium 3-hydroxynaphthalene 2-carboxylate (SHNC) have been probed by dynamic light scattering. The variation in the average diffusion coefficient of the micelles as measured by DLS experiments and the corresponding hydrodynamic diameter with the variation of molar ratio of SHNC to DTAB, c_{SHNC}, (at total surfactant concentration of 100 mM) is depicted in Figure 5.1. At low c_{SHNC}, D_a is consistent with the value that is expected for small globular micelles. However the equivalent sphere diameter of the micelles increases with an increase in c_{SHNC} and it reaches a value inconsistent with the alkyl chain length of the surfactant, suggesting growth of the globular micelles to form anisotropic aggregates. Earlier report on CTAB–SHNC mixed micelles, similar to the studied system, has shown a sphere to rod-like micellar transition [198]. Hence using Perrin's relation, the length of the micelles has been calculated from D_a and the length of the micelles shows an increase from few nanometers to about 60 nm, as c_{SHNC} varies from 0 to 0.33 (Figure 5.2).
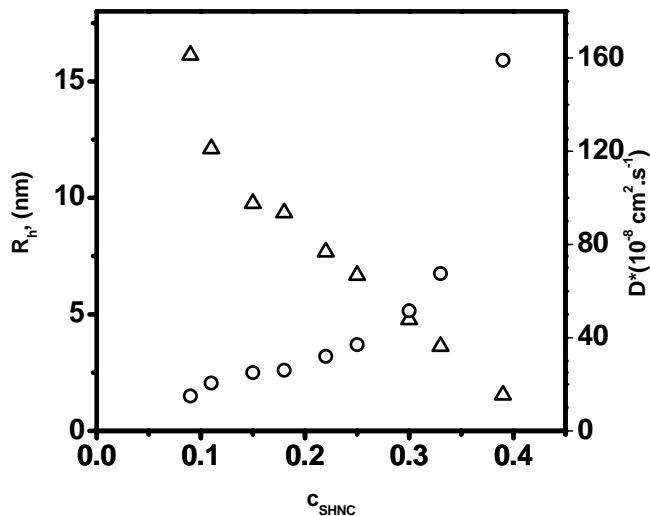
Figure 5.1 Apparent hydrodynamic radius and diffusion coefficient of DTAB–SHNC mixed micelles (C_T = 0.1 M) as a function of molar ratio of SHNC to DTAB (c_{SHNC}).
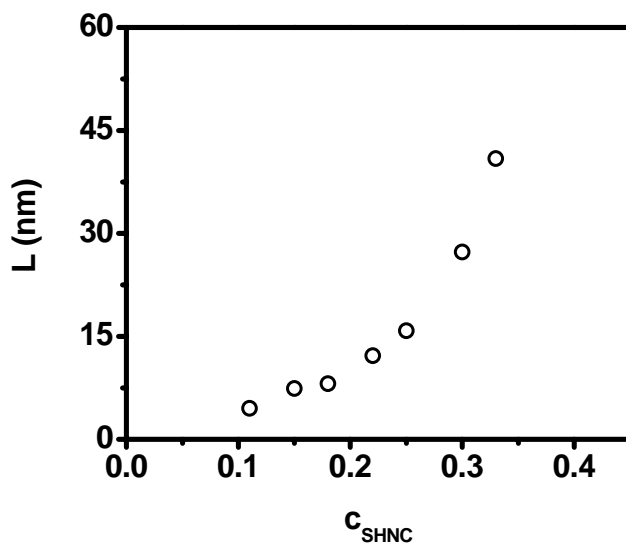
Figure 5.2 Average length (*L*) of DTAB–SHNC mixed micelles (C_T = 0.1 M) as a function of molar ratio of SHNC to DTAB.

With an aim to study the dilution effect on the microstructures of surfactant-hydrotrope micelles in the surfactant rich region, changes in the microstructure of DTAB–SHNC mixed micelles upon dilution have been probed by dynamic light scattering. The

134

variation in the apparent hydrodynamic radius of DTAB–SHNC micelles upon dilution for three fixed molar ratios of SHNC to DTAB (c_{SHNC} = 0.5, 0.4 and 0.3) is depicted in Figure 5.3. Dilution studies were performed on the surfactant rich side of the surfactant-hydrotrope system, starting with high concentration of surfactants. For all three fixed c_{SHNC}, the hydrodynamic radius of DTAB–SHNC micelles shows an increase with dilution indicating a microstructural transition in the micelles. Further dilution brings about a phase separation in
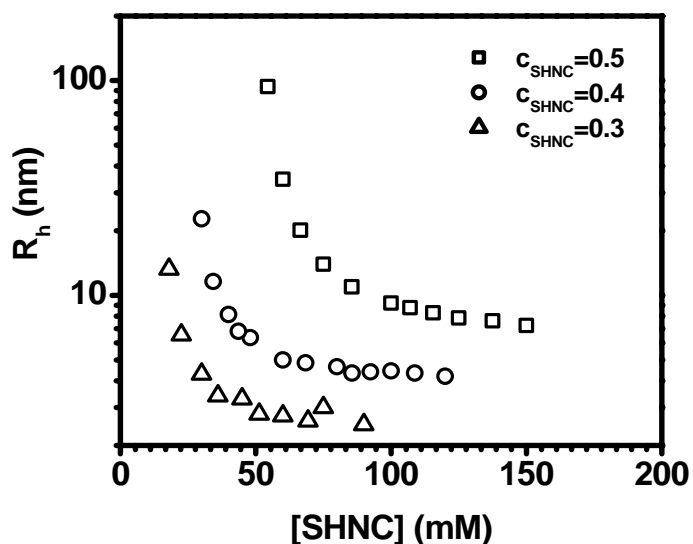
Figure 5.3 Apparent hydrodynamic radius of DTAB–SHNC mixed micelles as a function of SHNC concentration at three fixed c_{SHNC} = 0.5, 0.4 and 0.3.

the solution, suggesting micelles have grown to large structures. Figure 5.4 depicts the length of the mixed micelles upon dilution for three fixed c_{SHNC} using the Perrin's relationship as discussed in the previous section. Such an analysis suggests that the length of the micelles increases with dilution for a fixed c_{SHNC}. The length of the micelles has gone to very large
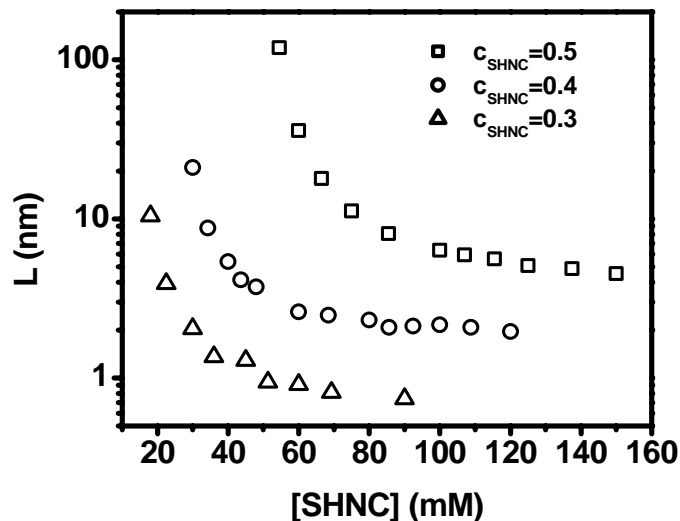
Figure 5.4 Average length (*L*) of DTAB–SHNC mixed micelles as a function of SHNC concentration at three fixed c_{SHNC} = 0.5, 0.4 and 0.3.

values with high dilutions. All the above observations confirm that there is a microstructural transition in the mixed micelles upon dilution, preferably from spherical to rod-like to vesicles. SANS studies were performed to further explain the microstructural transitions.

5.2.2 SANS studies

To understand the exact structure of the mixed micellar system in the dilute region as discussed above, small angle neutron scattering studies were performed. Figures 5.5, 5.6, and 5.7 depict the SANS spectra for DTAB–SHNC mixed micelles upon dilution at three fixed molar ratios of SHNC to DTAB, c_{SHNC} = 0.4, 0.3, and 0.2 respectively. It should be noted that SANS studies were performed for c_{SHNC} = 0.2, instead of c_{SHNC} = 0.5 as done for DLS studies. This is due to the reason that SANS technique gives better results for smaller structured particles, as compared to DLS. The SANS spectra shown in Figures 5.5 and 5.6, in the dilute regime, depict characteristic scattering pattern for rod-like objects. The scattering intensity, at small scattering vectors shows q $^{-1}$ behavior, characteristic of a rod-like structure. From Figure

5.7, it is evident that at high volume fraction of micelles, i.e. for the concentrated solution of $c_{SHNC} = 0.2$, SANS spectrum shows a correlation peak in the low q region indicating the presence of intermicellar interactions. Also the position of the correlation peak shifts to lower q values upon dilution i.e. with a decrease in the volume fraction of micelles. These features are characteristic of a structural transition from globular to rod-like micelles. Also the correlation peak in the spectrum shows a broadening upon dilution, suggesting a decrease in the electrostatic interactions between the micelles. To analyse the SANS data, firstly the model independent IFT method has been employed, to assesss the structural changes. The IFT method allows us to evaluate the pair distance distribution function (PDDF), p(r), of the micelles. The IFT procedure is carried out without considering any interparticle interaction. Variations in the p(r) function of the micelles upon dilution for three different molar ratios of SHNC to DTAB, $c_{SHNC} = 0.4$, 0.3 and 0.2, as obtained from the IFT analysis, are depicted in Figures 5.8, 5.9, and 5.10 respectively. It is observed that the PDDF of mixed micelles at the highest concentrations shows the influence of structure factor (though weak), as indicated by a weak oscillation in $p(r)$, but with dilution, this oscillation disappears, indicating a transformation to short rods with nearly constant cross-sectional dimension (as indicated by the maxima in the p(r) functions) and increasing average length. The p(r) functions indicate a transition of the micelles from spherical to rod-like micelles. Based on the structural information obtained from IFT analysis, the SANS data were fitted using a prolate ellipsoid model and by neglecting the interparticle interaction parameter S(q), as there is no correlation peak in the spectra. The scattering length density of the micelles is calculated by taking into account both DTAB and SHNC in the micelles at appropriate mole fractions. The length,
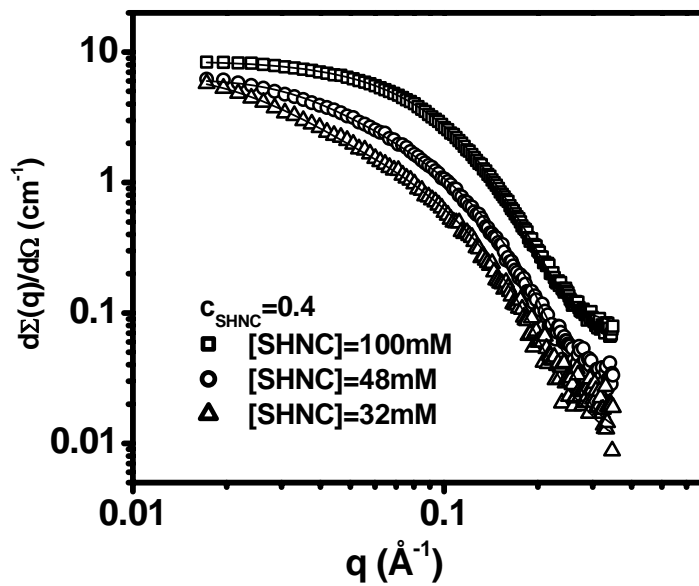
Figure 5.5 SANS spectra for DTAB–SHNC mixed micelles at different dilutions, keeping $c_{SHNC} = 0.4$.
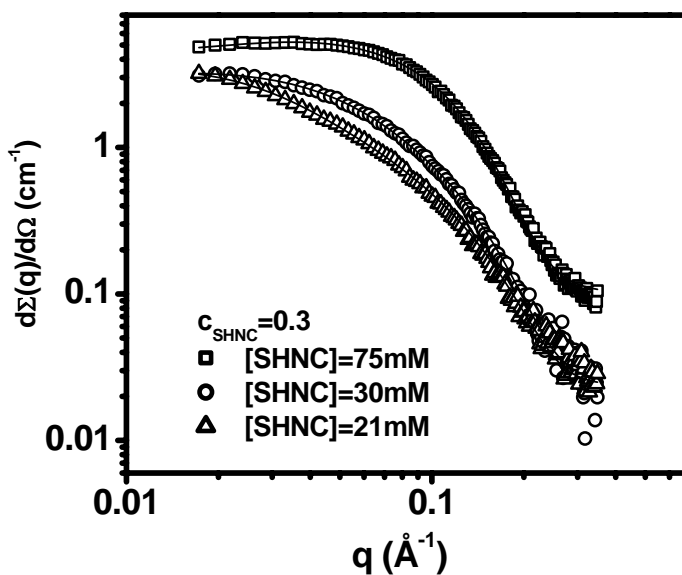
Figure 5.6 SANS spectra for DTAB–SHNC mixed micelles at different dilutions, keeping $c_{SHNC} = 0.3$.

radius, and the volume fraction of the cylinders were used as the fitting parameters. The results obtained by model fitting of SANS data are summarized in Tables 5.1, 5.2, and 5.3 are

in accordance with the one obtained by IFT analysis. For all mole fractions studied, the axial

ratio increases and the fractional charge decreases upon dilution.
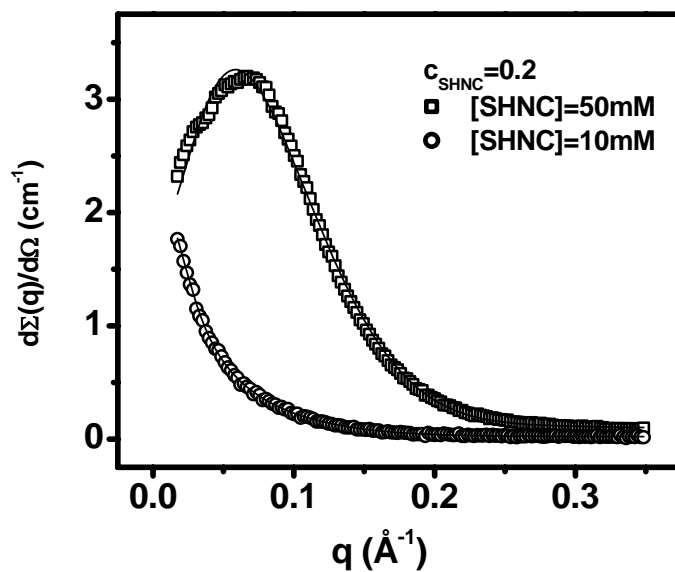
Figure 5.7 SANS spectra for DTAB–SHNC mixed micelles at different dilutions, keeping $c_{SHNC} = 0.2$.
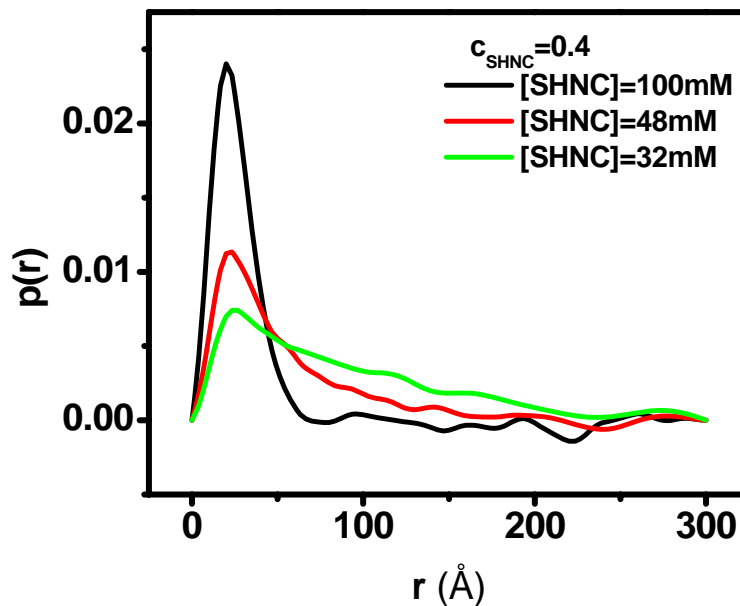
Figure 5.8 PDDFs (obtained from the IFT analysis of the SANS spectra) of DTAB–SHNC mixed micelles at different dilutions, keeping $c_{SHNC} = 0.4$.
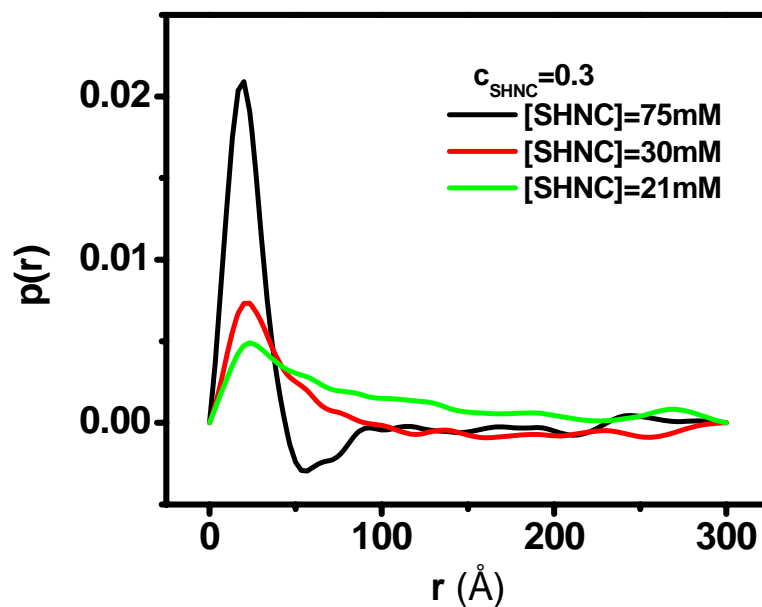
Figure 5.9 PDDFs (obtained from the IFT analysis of the SANS spectra) of DTAB–SHNC mixed micelles at different dilutions, keeping $c_{SHNC} = 0.3$.
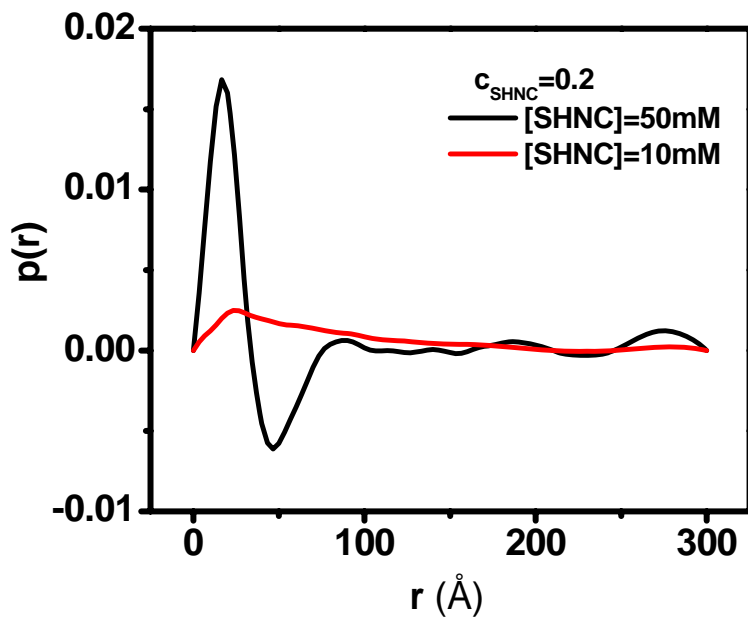
Figure 5.10 PDDFs (obtained from the IFT analysis of the SANS spectra) of DTAB–SHNC mixed micelles at different dilutions, keeping $c_{SHNC} = 0.2$.

Table 5.1 Micellar parameters obtained from the SANS analysis of DTAB-SHNC mixed micelles at different dilutions, keeping a fixed molar ratio of SHNC to DTAB (c_{SHNC}) of 0.4.

S.No.	[SHNC] in mM at fixed molar ratio of SHNC to DTAB, c_{SHNC}=0.4	Semiminor axis, b (Å)	Semimajor axis, a (Å)	Axial ratio
1	100	16.47	38.32	2.3
2	48	16.09	75.62	4.7
3	32	16.65	142.00	8.5

Table 5.2 Micellar parameters obtained from the SANS analysis of DTAB-SHNC mixed micelles at different dilutions, keeping $c_{SHNC} = 0.3$.

S.No.	[SHNC] at fixed molar ratio of SHNC to DTAB, c_{SHNC}=0.3	Semiminor axis, b (Å)	Semimajor axis, a (Å)	Axial ratio
1	75	16.46	28.59	1.7
2	30	15.76	54.63	3.5
3	21	15.17	100.37	6.6

Table 5.3 Micellar parameters obtained from the SANS analysis of DTAB-SHNC mixed micelles at different dilutions, keeping $c_{SHNC} = 0.2$.

S.No.	[SHNC] at fixed molar ratio of SHNC to DTAB, c_{SHNC}=0.2	Semiminor axis, b (Å)	Semimajor axis, a (Å)	Axial ratio
1	50	15.96	22.90	1.4
2	10	16.22	119.38	7.4

A comparison of DLS and SANS results show that the micellar length estimated from DLS is significantly larger than that is obtained from SANS. It is probable that at lower volume fraction of micelles upon dilution, the charge density of the micelles is low; the micelles are highly polydisperse with an exponential length distribution. Moreover, at very low volume fractions the mixtures phase separate to form large aggregates or coacervates as already discussed in the previous section. Thus, there is a possibility of forming mixtures of rod-like aggregates and large aggregates. Due to the limited q-range of SANS, the features are primarily from the small segments of the long micelles, or short rods; while DLS results will be skewed to longer micelles as well as other large structures, as it measures the z-average diffusion coefficient. Thus, by combining DLS and SANS results, it can be concluded that changes associated with dilution of surfactant-rich micelles arises from dilution induced growth of spherical to rod-like micelles.

Figure 5.11 shows the cryo-TEM images of DTAB-SHNC mixed micelles at a molar ratio of SHNC to DTAB of 0.4 (c_{SHNC}=0.4) and at a concentration of SHNC of 32 mM. It
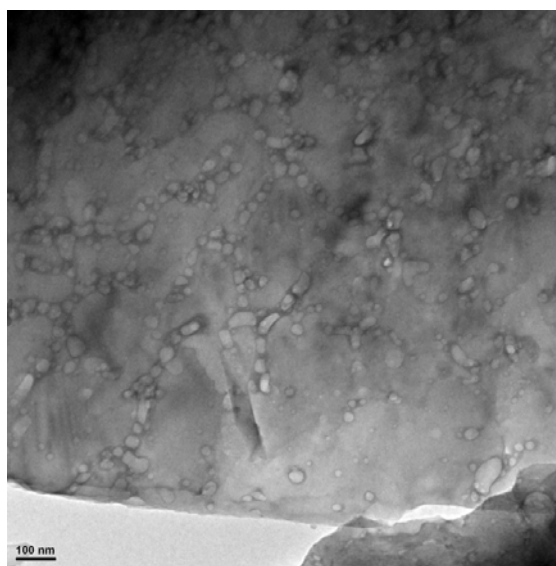
Figure 5.11 Cryo-TEM image of DTAB–SHNC mixed micelles at a molar ratio of SHNC to DTAB, $c_{SHNC} = 0.4$, at a concentration of SHNC of 32 mM.

shows the presence of large anisotropic globules, of the order of 100 nm, presumably arising from coacervates coexisting with micellar aggregates. Thus cryo-TEM studies confirm the presence of such large structures at very low concentration.

The dilution induced growth of DTAB-SHNC mixed micelles upon dilution has been explained on the basis of low critical micelle concentration or CMC of DTAB surfactant. As the study is on the surfactant rich side, upon dilution, the surfactant DTAB desorbs from the micellar aggregate as the solution equilibrates and hence the ratio of SHNC to DTAB increases in the micellar aggregate structures. The effective charge on the micellar aggregate will also decrease due to ion-pair neutralization. This results in the lowering of the spontaneous curvature of the DTAB-SHNC mixed micelles, giving rise to a microstructural transition from spherical to rod-like micelles. A similar mechanism has been proposed by Egelhaaf and Schurtenberger for explaining the dilution induced structural changes in bile salt–lecithin mixed micelles, where on dilution spherical to rod-like micelle and then to vesicle transition takes place [199]. This is attributed to the different solubilities, i.e. critical micelle concentration (cmc), of lecithin and bile salt. Upon dilution, bile salt to lecithin ratio in the aggregates decreases, lowering the average spontaneous curvature of the mixed micelles. Kaler and Lee [200] have also demonstrated the transformation of micelles to vesicles upon dilution in a system of lecithin–bile salt mixed micelles using DLS and SANS studies. Upon dilution, the bile salt molecules are extracted from the micelles that are composed of a mixture of surfactant and bile-salt to maintain the external monomer concentration, resulting in the growth of the micelles with dilution, and the overall composition of the micelle varies as the micelle length changes. A similar mechanism can be invoked in the present study.

Olsson and co-workers [201] have demonstrated the vesicle–micelle transition in the salt-free surfactant hexadecyltrimethylammonium octylsulfonate using SANS, light microscopy, cryo-TEM, and water self-diffusion NMR. The changes in microstructure at high dilution and high temperature could be understood from differences in the solubility, electrostatic interactions, and preferred aggregate curvature. The solubility of the octylsulfonate ion in water is higher than that of the hexadecyltrimethylammonium ion. Hence upon increasing the temperature, the ratio of free octylsulfonate ion relative to the neutral hexadecyltrimethylammonium octylsulfonate increases. As a result, the surface charge density of the aggregates increases and this ultimately induces a transition to higher curvature morphology (elongated micelles). A micelle to vesicle morphological transition has also been reported in block copolymer micelles of poly(styrene)-blockpoly(4-vinylpyridine)/perfluorodecanoic (PS-b-P4VP/PFDA) acid complexes in chloroform at a fixed molar ration of 1:1 upon dilution by different techniques such as DLS, optical microscopy, atomic force microscopy, and transmission electron microscopy [202]. The key factor in controlling the initial morphology is believed to be the competition between complexation and micellization. The initial spherical micelles results from the aggregation of insoluble P4VP/PFDA complexes in which only a part of the available 4VP units would have formed complex with PFDA molecules. Upon dilution of the system, partial resolubilization or swelling of the initially formed P4VP/PFDA complexes could occur, resulting in further complexation with remaining fluorinated surfactant molecules. The increased amount of fluorinated tails in these complexes leads to spheres-to-vesicles transition in the micellar system. It can be inferred from the present study that the difference in the critical aggregate

concentration of individual components in a mixed micellar formulation can trigger dilution induced microstructural transition.

5.3 Conclusion

In this work, dilution induced structural changes in a mixed micelle composition comprising cationic surfactant, DTAB and hydrophobic salt SHNC, at different molar ratios of SHNC to DTAB has been studied. DLS studies have indicated an increase in the size of the mixed micelles at a fixed molar ratio of SHNC to DTAB upon dilution. From SANS studies, the increase in the size was attributed to a structural transition of the mixed micelles from spherical to rod-like micelles upon dilution. Finally cryo-TEM has indicated the presence of anisotropic globules at low volume fraction of mixed micelles. This unusual behavior of surfactant-rich micelles is explained in terms of desorption of surfactant from mixed micelles with dilution. Desorption of surfactant is attributed to its high value of critical micelle concentration (CMC). Such studies have great importance in pharmaceutical industries, like in drug delivery studies.

CHAPTER 6

Polyaniline nanoparticle
synthesis in micelles and its
application in biosensors

6.1 Introduction

Conducting polymers has recently gained a lot of importance for new product concepts and for replacing conventional materials due to their unique combination of conductivity and optical and mechanical properties. There has been considerable interest in conducting polymers owing to their potential for applications in batteries [203-206], sensors [207-210], electrochromic display devices [211-213], and microelectronic devices [214]. Among conducting polymers such as polyaniline (PANI), polypyrrole, polythiophene, and polyacetylene, PANI has been extensively studied because of its tunable electrical properties, high environmental stability, and relatively low cost. By a suitable change in pH (protonation reaction), the electrical conductivity of these polymers can be altered to tune them up as an insulator, semiconductor, or conductor [215-217]. PANI exists in various forms depending on the oxidation states; such as leucoemeraldine, pernigraniline, and emeraldine or emeraldine salt.

Processability of PANI is difficult due to its very low solubility in different solvents, restricting its applications. Hence, doping of PANI with protonic acids such as camphorsulfonic acid (CSA) or dodecylbenzenesulfonic acid (DBSA) is known to increase the solubility of emeraldine salt form in solvents such as *m*-cresol, xylene, etc. [218, 219]. This is because the negatively charged sulfonate group of the dopant gets associated with the positively charged backbone of the emeraldine salt form of the polymer through Coulomb attraction thereby providing a hydrophobic side chain compatible with organic solvents.

Another method to improve processability of this material has been to prepare them as colloidal nanoparticles. Many different strategies have been employed for the preparation of PANI dispersions in colloidal form. Typically, they are produced by chemical polymerization

of aniline in the presence of various polymeric stabilizers such as poly(ethylene oxide), poly(vinyl alcohol), poly(vinyl methyl ether), poly(*N*-vinylpyrrolidone), hydroxypropyl cellulose, methyl cellulose, etc. [220-226]. The size, morphology, and stability of PANI particles were strongly dependent on the choice of stabilizers, oxidant, and reaction conditions [227].

Microemulsions, inverted emulsions, and other template-free methods have also been used for the successful generation of PANI nanostructures [228-233]. Recently, micellar solutions of sodium dodecylsulfate (SDS) and sodium dodecylbenzenesulfonate (SDBS) were used to produce colloidal polymeric particles dispersible in water [234-239]. Previous reports mainly focused on the effect of monomer and surfactant concentration on composition, morphology, crystalline nature, and conductivity of PANI. Attempts have also been made to understand conformation of CSA-doped polyaniline in organic solvents such as *N*-methylpyrrolidinone (NMP) or *m*-cresol using dynamic light scattering, and the results suggest that in dilute solutions the polymer exists as a true molecular solution and the behavior is similar to that of polyelectrolytes [217, 240].

PANI has also been employed in the development of immunosensors /biosensors [241]. Biosensor is considered a synergic combination of analytical biochemistry and microelectronics. In general, a biosensor consists of biological component in intimate contact with a suitable transducer coupled through immobilization and the biological component gives rise to signal as a result of the biochemical reaction of the analyte which is detected by transducer to give an electrical signal (Figure 6.1). Hence the produced electrical signal can be used with or without amplification for the estimation of the concentration of the analyte in a given sample. Also, the specific interaction between an antigen and antibody (biological

macromolecules) can be made use of in the selective estimation of various proteins. Traditionally, estimation of protein by antigen-antibody interaction has been done using enzyme linked immunosorbant assay (ELIA), radio-immuno-assay (RIA), and western blot in
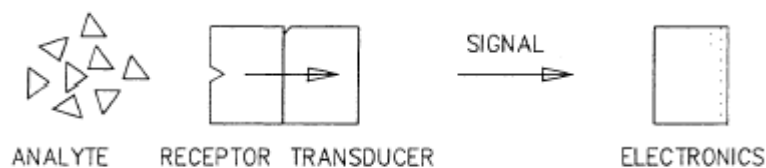
Figure 6.1 Schematic of biosensors

plasma of various fish species [242]. However, these traditional immunoassay techniques are complicated multistage processes, tedious, and expensive whereas the electroanalytical technique is much more sensitive, versatile, and inexpensive. The electronically conducting polymer possess numerous features, which allow them to act as excellent materials for immobilization of biomolecules and rapid electron transfer for fabrication of efficient biosensors (Figure 6.2).
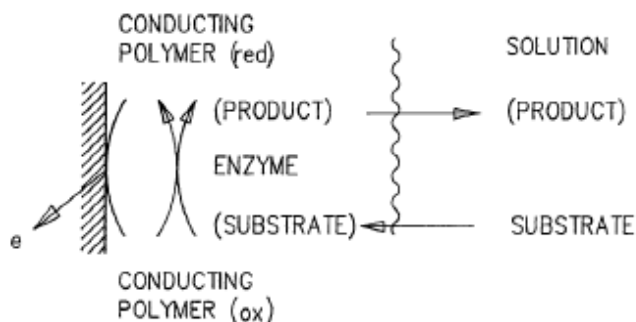
Figure 6.2 Suggested pathways for electron transfer in conducting polymer based biosensor.

With a view to investigate the above effect, polymerization of aniline was carried out at different ratios of monomer to surfactant and a correlation between the size of PANI

particles with the size of the micelles was obtained. Further interaction of protein BSA with PANI nanoparticles has been studied. Addition of the monomer aniline in acidic medium to anionic micelles of SDS changes the microstructure of micelles from nearly spherical aggregates to rod like micelles. The effect of micelle structure on size of colloidal polymeric particles was investigated using dynamic light scattering (DLS). By proper control of the micelle size and concentration, PANI colloidal suspensions with varying hydrodynamic diameter can be prepared in SDS micelles.

6.2 Preparation of PANI nanoparticles in micelles

Mixture of anionic surfactant and cationic hydrophobic salt forms various microsturctures with varying ratio of surfactant to hydrophobe. Using this as the basis for the synthesis of nanoparticle of various sizes, polymerization of anilinium hydrochloride salt adsorbed on the surface of anionic micelles sodium dodecylsulphate (SDS) was carried out chemically using oxidizing agent potassium peroxodisulphate (KPS) under different morpholgy of micelles. In the presence of SDS, PANI is already protonated even at neutral pH 7 while in the absence of SDS a pH of 4 is required for protonation [243]. The existence of PANI in the emeraldine salt form at a higher pH of 7 in the presence of SDS can be explained in terms of the formation of a stable complex between the dodecylsulfate anion and the cationic emeraldine salt form of the polymer. For polymerization studies, SDS concentration has been fixed at 50 mM and the ratio of anilinium salt to surfactant i.e. [AHC]/[SDS], c_{AHC} is varied from 0.4 to 0.8. Preliminary studies indicated that the size of the polymer particles depends also on the molar ratio of KPS to aniline, and thus, this ratio is kept constant (equal to 1) for all the sample preparations. Previous reports also show that the amount of oxidizing agent has an influence on the molecular weight of the polymer [244].

The polymerization of aniline progressed quickly after a small induction period of 10-15 min and a bluish green color developed in the solution with time. Surfactant stabilized colloidal suspensions of polyaniline nanoparticles were formed in all the reaction mixtures. Dynamic light scattering (DLS) measurements were carried out on surfactant stabilized PANI particles during the course of the polymerization process (after 3 hours of the mixing of reagents) to assess the average apparent hydrodynamic diameter (using Stokes Einstein equation) of the particles. For DLS measurements, an aliquot of the sample is diluted enough to very low surfactant concentration, to reduce additional errors in the measurement due to the thermal lensing and consequent coning of the laser beam, as PANI nanoparticles has strong absorption property and the absorbance is small at the wavelength of DLS measurement with dilution. All samples were characterized as prepared after diluting with deionized water so that polyaniline exists in the emeraldine salt form for which the absorbance shows a minimum at the wavelength of measurement.

Figure 6.3 depicts the variation in the apparent size of PANI particles with changes in AHC concentration. With increasing ratio of anilinium salt to surfactant i.e. [AHC]/[SDS] (c_{AHC}), an increase in the apparent hydrodynamic diameter (size) of the PANI particles was observed. It can be concluded that PANI particles of various sizes can be prepared as a water-dispersible colloid using SDS micelles of controlled size.

Anionic surfactants can influence the formation of PANI colloids in many different ways. They can act as a dopant thereby stabilizing the emeraldine salt form of the PANI polymer. Doping with surfactants is known to improve the solubility of the polymer in organic solvents. Owing to the hydrophobic nature of aniline molecule, these monomers can preferentially get partitioned into the micellar phase thereby increasing its local concentration

in the reaction medium. Due to the positive charge on anilinium ion in AHC, it further facilitates the adsorption of this molecule on the surface of anionic micelles through electrostatic interactions.
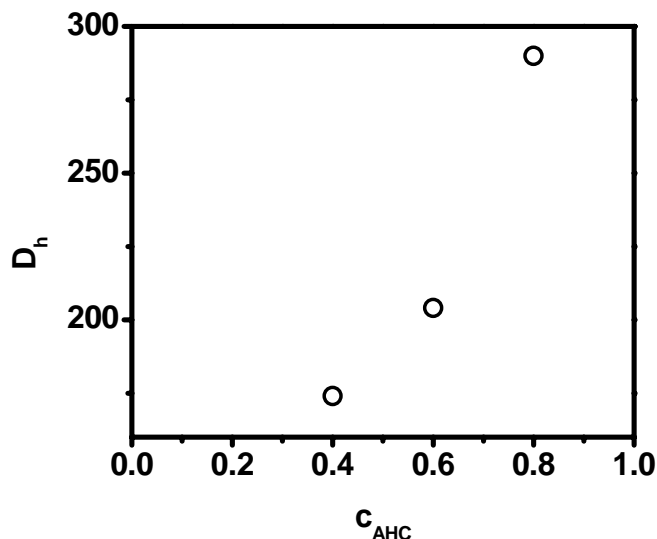
Figure 6.3 Variation of the average hydrodynamic diameter (D_h) of polyaniline particles prepared in 50 mM SDS micelles with different molar ratios of AHC to SDS (c_{AHC}), after 3 hours of the reaction.

PANI prepared at $c_{AHC=}$ 0.4 has been used for interaction studies of a model protein Bovine serum albumin (BSA) with PANI nanoparticles. Figure 6.4 depicts the apparent hydrodynamic diameter and scattering intensity of PANI nanoparticles prepared at x_{AHC} 0.4 at different dilutions. DLS data clearly shows that the scattering intensity follows a linear graph with a constant value of apparent hydrodynamic diameter of 175 nm, confirming that the effect of interparticle interactions is negligible in the studied concentration range. The particles are stable even after dilution shows that the stability of surfactant stabilized PANI nanoparticles is good.
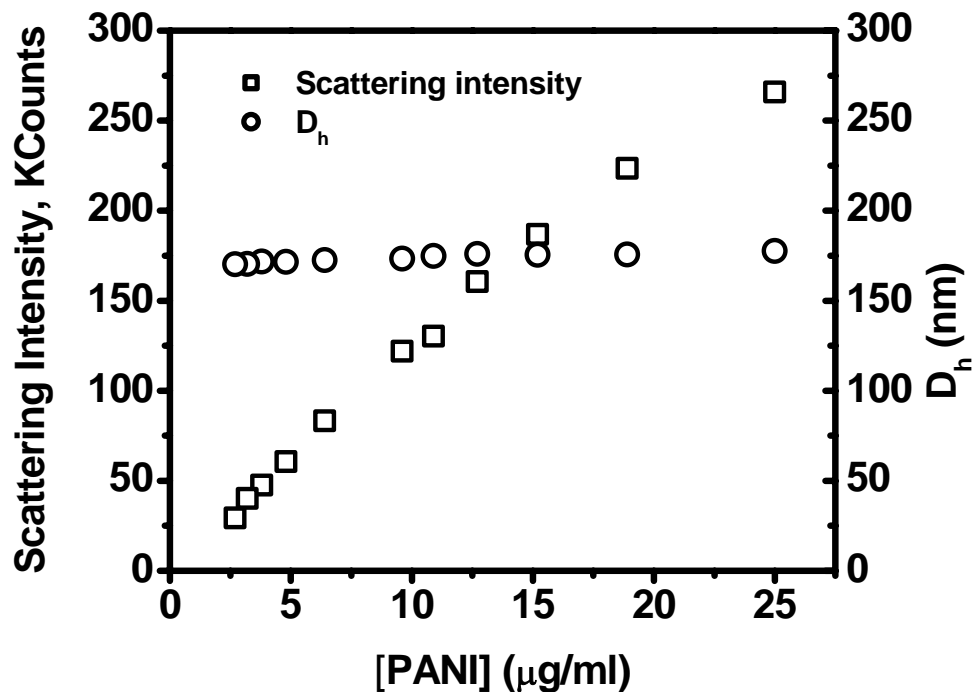
Figure 6.4 Variation of apparent hydrodynamic diameter (D_h) and scattering intensity of PANI particles at different dilutions, prepared at $c_{AHC} = 0.4$.

The electric field correlation function of scattered light and the size distribution of the PANI nanoparticles, as obtained by monomodal (cumulants) analysis of the DLS data are depicted in Figures 6.5 and 6.6 respectively. The polydispersity index of the colloidal suspension, as measured by the ratio of variance to the square of the mean diameter, is found to be 0.26. To monitor the interaction of PANI with other biomolecules, for sensor application, BSA is chosen as the model protein which in general is a standard protein for biomedical studies, as it is a non- specific protein. As the above prepared PANI particles are stabilized by SDS surfactant, which in turn can change the conformation of proteins, hence the surfactants were removed by washing with methanol.
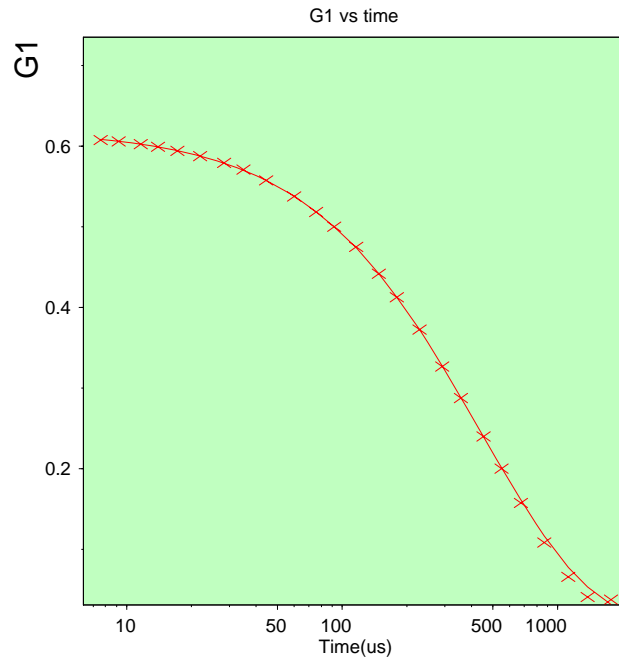
Figure 6.5 Correlation function of PANI particles, prepared at $c_{AHC} = 0.4$.
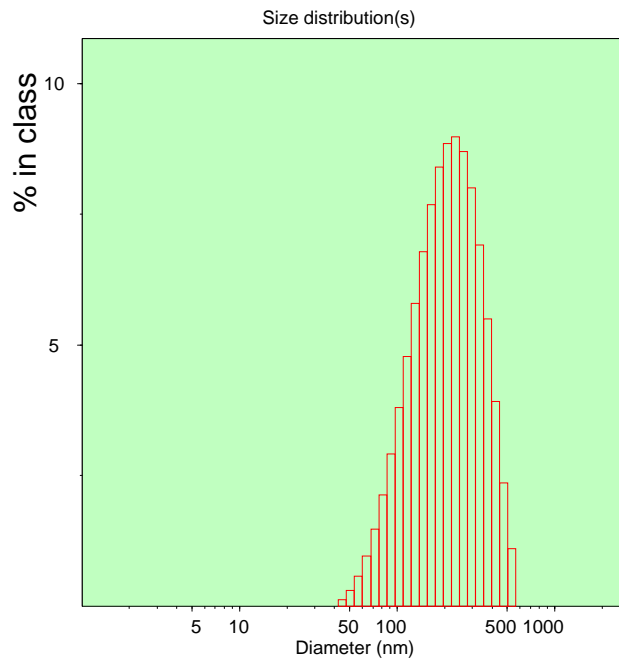
Figure 6.6 Size distribution data of PANI nanoparticles, prepared at $c_{AHC} = 0.4$.

After 3 hours of polymerization at c_{AHC} equals 0.4, solvent methanol is added into the reaction mixture for arresting the reaction. Addition of methanol leads to precipitation of the colloid and the precipitated colloid is filtered and washed with aqueous methanol. This ensures removal of surfactants. The surfactant free colloid is redispersed in water and light scattering studies were carried out. Figure 6.7 depicts the apparent hydrodynamic diameter of 15 μg/ml PANI particles with the addition of protein BSA. In the absence of protein the apparent diameter is found to be much larger than that is observed for SDS stabilized particles. With the addition of BSA protein, the size of PANI nanoparticles decreases and becomes constant at high concentration of (0.006 wt%) BSA, showing the same D_h value as
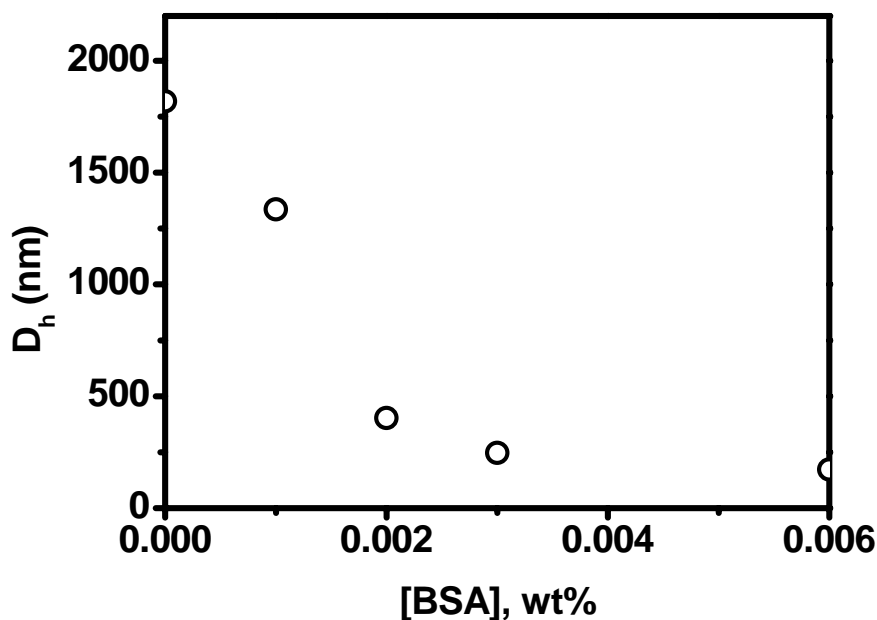
Figure 6.7 Variation of apparent hydrodynamic diameter (D_h) of PANI particles as a function of added BSA concentration.

the SDS stabilized PANI nanoparticles. The large size of PANI particles in the absence of BSA is due to the agglomeration of PANI nanoparticles in the absence of surfactant. With the addition of BSA, BSA interacts with PANI particles, redisperse the agglomerates and

154

stabilizes it. This suggests that the there is an interaction between PANI nanoparticles and BSA protein. This is further confirmed from the optical absorption spectra of PANI nanoparticles at different additions of protein BSA.

Also as indicated in Figure 6.8, with the addition of BSA protein, the absorption spectrum shifts to higher wavelengths. Such shift in the spectrum can be attributed to emeraldine salt form of PANI in the presence of BSA.
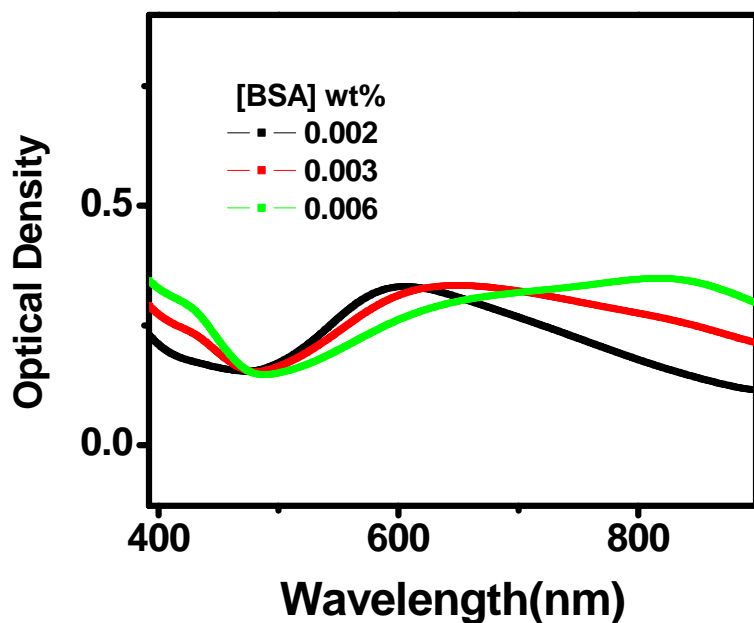
Figure 6.8 Optical absorption spectra for PANI nanoparticles at different concentrations of added protein BSA.

From all the above studies, it is inferred that protein BSA interact with PANI nanoparticles, gets adsorbed to it and stabilizes the emeraldine salt form of PANI nanoparticles. Such changes in the nature of PANI form can significantly alter the conductivity of the polymer. Based on these preliminary studies done on PANI nanoparticles, formulation of an electrical immunosensor for progesterone based on polyaniline has been attempted.

6.3 PANI for biosensor application of progesterone

Progesterone, the major naturally occurring C-21 steroid hormone (belongs to a class of hormones called progestogens) is involved in the female menstrual cycle, pregnancy and embryogenesis of humans and other species. Recently, Brann [245] reviewed the effects of progesterone, especially its role in regulating the sequence of the ovulatory cycle by controlling other hormones. In women, progesterone levels are low (< 2 ng/ml) during the preovulatory phase of the menstrual cycle and it rises after ovulation (> 5 ng/ml). Thus progesterone concentration in blood samples can be utilized to determine ovarian function i.e. as an indication of endocrinopathy and virilism for which a rapid and accurate detection of progesterone at very low levels is desirable in the human body.

To date various immunoassay methods have been applied to measure the progesterone level. Recently a commercial monoclonal antibody to progesterone derivative was incorporated into immunoassay for the detection of progesterone in bovine milk. The detection is based on the fluorescence of labelled antibody by total internal reflectance fluorescence (TIRF) which achieved a detection limit of 1 ng mL^{-1} for a fully automated sensor. Forster *et al.* described a method for progesterone detection and measurement in whole blood samples by a surface sensitive biosensor used in conjunction with an integrated optical grating coupler [246]. A candidate reference measurement procedure for progesterone in human serum involving isotope dilution coupled with liquid chromatography/tandem mass spectrometry (LC/MS) has been developed and critically evaluated [247]. Amine/imine functional groups of polyaniline modified surfaces have shown improved binding of triiodothyronine(T_3) antibodies on polystyrene surface that can be used as a substrate for the detection of human thyroid hormone in ng/ml level using radioimmunoassay (RIA) [248]. The

percentage of rabbit IgG coated on polyaniline modified tubes, as estimated using IgG-^{125}I, was found to be 90 ± 1.8 % as compared to 42 ± 5 % in unmodified tubes. The percentage binding of T$_3$-^{125}I to antibody coated on polyaniline modified polystyrene tubes through physical adsorption was found to be 36 ± 2 % as compared to 28 ± 4 % that was observed for unmodified tubes. The role of functionalized surfaces using polyaniline in immunoassays is many fold, nanoparticulate adsorption enhances the surface roughness leading to enhanced surface area, electrostatic binding of antibodies due to the charged nature of the surface that varies with the pH of deposition, and covalent or non-covalent binding of antibodies through coupling of amino group. However label free detection with comparable sensitivities is much more desirable owing to low cost and rapid detection. In this regard, the electrochemical immunosensors which can detect the immunological reaction directly, without using an additional label and compromising high sensitivity has gained lot of importance.

6.3.1 Optimization studies

6.3.1.1 Formation of PANI film on Glass

Synthesis of PANI film was achieved by in situ chemical polymerization of anilinium hydrochloride in presence of sodium hexametaphosphate (HMP) using potassium peroxodisulfate (KPS) as the oxidant at room temperature of 25 ^{0}C. The conditions for formation of thin uniform film of polyaniline on glass substrate were optimized by varying the concentration of monomer, HMP, and oxidant for obtaining thin uniform film of PANI, as thin PANI film is needed for registering any change in the electrical signal when interacting with the biomolecules. The results are tabulated below (Table 6.1). Looking at the results, it can be inferred that equimolar solutions of AHC, HMP, and KPS were mixed in the volume

ratio of 5:1:5 respectively for preparing a thin uniform film of polyaniline in the conducting PANI form, i.e. the emeraldine salt form.

Table 6.1 Optimization of reactant concentrations for polymerization of thin uniform film of PANI on glass substrate.

Sr. No.	0.1M aniline in 0.5 M HCl	0.1 M HMP in Water	0.1 M $K_2S_2O_8$ in Water	Water	Time taken	Comments
1	2 ml	2 ml		2 ml	overnight	Bad coating
2	2 ml	2 ml	2 ml	2 ml	2 hr. 20 min	Thick, not good coating
3	2 ml	2 ml	2 ml		1 hr	Uniform coating
4	1 ml	1 ml	2 ml		45 min	Thin uniform coating
5	**5 ml**	**1ml**	**5 ml**		**1 hr**	**Thin uniform coating**

6.3.1.2 Formation of PANI film on IDA

Chemical polymerization of anilinium hydrochloride in the presence of HMP using potassium peroxodisulfate (KPS) led to the deposition of the polyaniline film on the surface of silver Interdigitated array (IDA) microelectrodes. Line thickness and pitch of silver screen printed IDA is around 300 micron and connector pitch is 2.5 mm (PCB connector). The dispersion polymerization of polyaniline is carried out in an aqueous mixture containing aniline monomers and oxidants in the presence of a suitable stabilizer. Sodium hexametaphosphate (HMP) acts as a steric stabilizer and as a dopant due to its anionic nature. The presence of HMP can affect the rate of polymerization by changing the local pH microenvironment for the formation of the polymer. HMP, due to its anionic nature attracts H+ ions and therefore the surface of HMP (or the microenvironment of PANI) is at lower pH

even though the bulk pH is 6.8. This lower pH allows PANI to be in the conducting state. The onset of polymerization and subsequent deposition of polyaniline onto IDA could be identified from the visual observation of green color in the solution. The strong adhesion of polyaniline to the electrode and the substrate was evident from the fact that the green color of the film was retained on the surface of IDA even after removing from the reaction mixture and successive washings as shown in Figure 6.9.
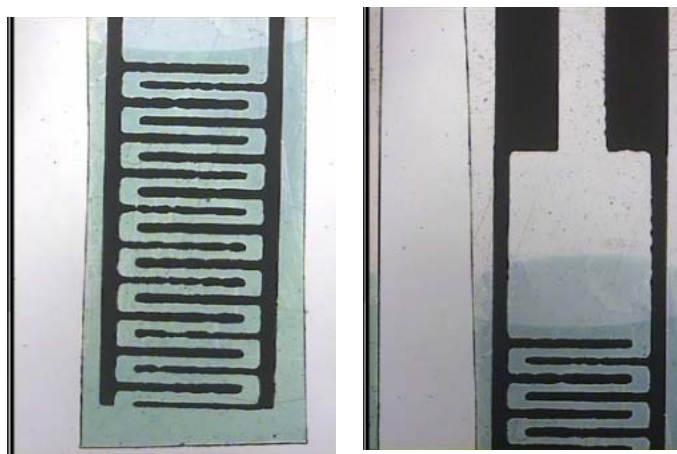
Figure 6.9 Micrograph images of polyaniline coated silver screen printed Interdigitated array (IDA) microelectrodes a) sensor end b) connector end.

With an increase in polymerization time, it was observed that the thickness of the polyaniline film formed on the surface has increased. This has been checked using glass slide as the substrate for polyaniline deposition. Figures 6.10 and 6.11 depict the optical absorption spectrum and optical density (O.D.) at 745 nm, of polyaniline film respectively, with an increase in polymerization time. As the absorption spectrum is showing peak at 745 nm wavelength of UV-Vis spectrum, indicates that the PANI film is in the emeraldine form, also indicated by the green color of the film. Also the O.D. is increasing with the polymerization time, suggesting that the film thickness is increasing with the time of polymerization. Hence it

can be concluded that polymerization time plays an important role in forming PANI films of particular thickness, in the present study the thin film.
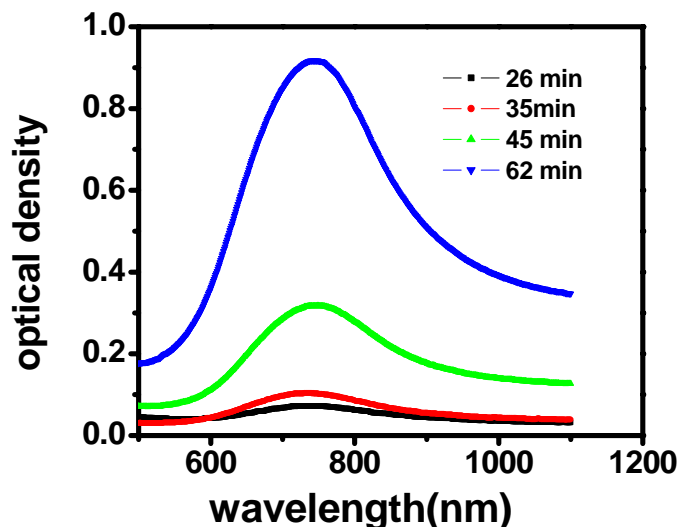
Figure 6.10 Optical absorption spectrum of polyaniline film at different polymerization reaction time.
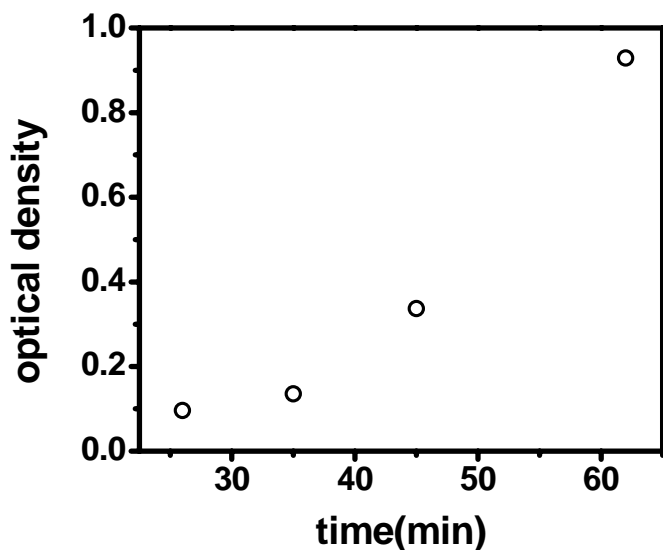
Figure 6.11 Optical absorption density of polyaniline film as a function of polymerization reaction time at a wavelength of 745 nm.

6.3.1.3 Factors affecting conductivity of polyaniline

The effect of various experimental parameters on the conductivity of the polymer film has been investigated in detail. Parameters such as pH of the solution and drying time were optimized for further sensing purpose.

(a) pH

At low pH i.e. in acidic medium the conductivity of the film is high and it decreases with an increase in pH. The change in the conductivity of films is due to the change in the form of PANI. PANI exists in various oxidation states ranging from fully reduced leucoemeraldine form to fully oxidized pernigraniline form. However, among various forms of PANI, only the emeraldine salt is in the conducting form [216]. The leucoemeraldine form has a band gap of nearly 4 eV, whereas the emeraldine base and fully oxidized pernigraniline forms have a band gap of the order of 2 eV (Figure 6.12) [217].

Figure 6.12 Different forms of polyaniline (PANI) in various oxidation states.

(b) Drying time

Figure 6.13 depicts the current as a function of voltage i.e. the I-V plot for PANI film with drying time and Figure 6.14 shows the corresponding current versus drying time plot.

There is a decrease in the conductivity with drying time, as indicated by a decrease in the slope of I-V plot with drying time, and reaches a saturation value after 60 minutes of drying the film.
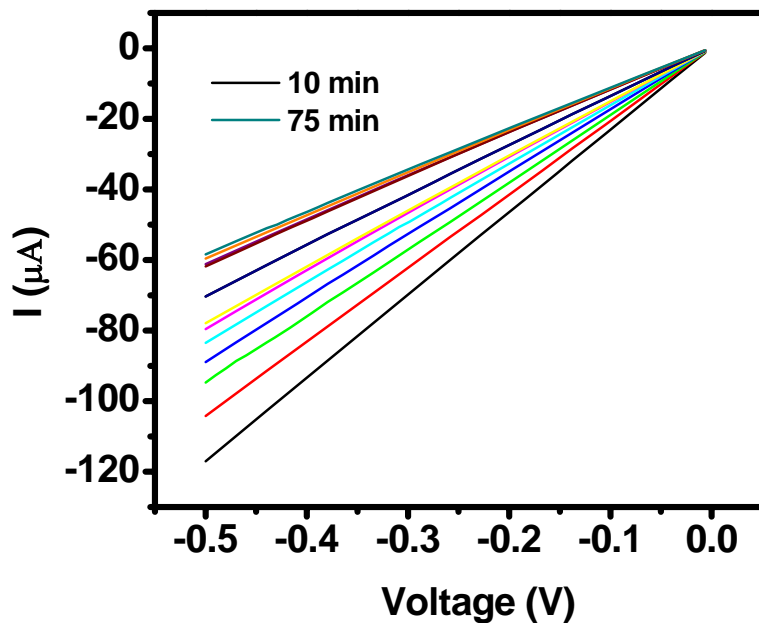
Figure 6.13 Voltammetric response (I-V plot) showing change in conductivity with time of drying.
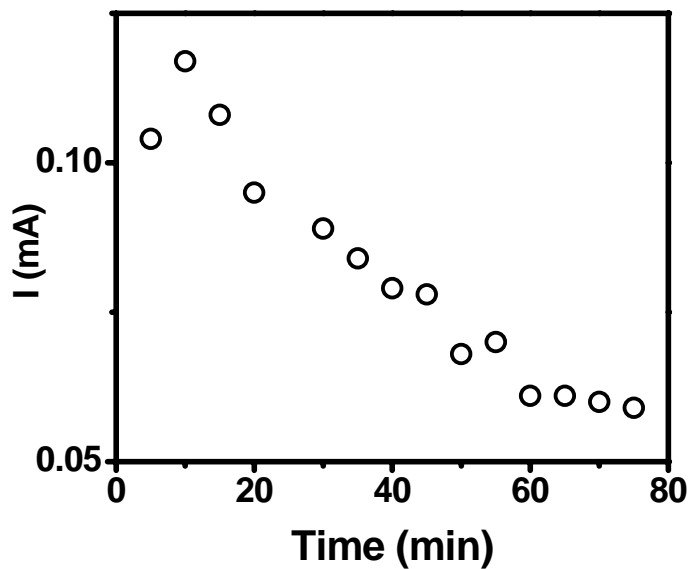
Figure 6.14 Current vs drying time plot for PANI film.

Hence, an optimum drying time of 60 minutes is required to reach saturation resistance value.

6.3.2 Immobilization of progesterone antibodies and antigen

Standard solution of progesterone antibody was prepared by dissolving 1 µg of progesterone antibody in 1.0 ml of deionised water to get the concentration of 1000 ng/ml. PANI coated IDA was then immersed into a solution of 1:15 (v/v) antibody ion solution: PBS buffer (pH 6.8) for 2 hours at room temperature for the adsorption of antibodies on the electrode surface, time sufficient for equilibration and adsorption of antibody. After this, the IDA was washed with fresh PBS buffer (pH 6.8) to remove any unbound antibodies from the electrode surface. The IDA microelectrodes were further incubated in 1% BSA in PBS for 1 hour to block the free sites that may unspecifically adsorb the antigen, followed by washing it with deionized water and air drying. The stock solution of progesterone antigen of 500 ng/ml concentration was prepared by dissolving 1 µg in 2.0 ml of PBS. The antibody coated electrodes were evaluated for its immunological response with progesterone antigen in the concentration range of 1.0-10.0 ng/ml. For each addition of progesterone standard, the antibody-coated immunoelectrode was incubated for 60 minutes in the solution. The electrodes were washed with deionised water and air dried before measurement.

6.3.3 Amperometric detection of progesterone

The immobilization of progesterone antibodies were carried out in a buffer solution with a pH 6.8 to ensure incorporation of the biological components into the polymer film in an active state. PANI exists in the conducting emeraldine salt form even at the electrolyte pH of 6.8 as discussed earlier. The amperometric measurements were performed on a dry device prepared by incubating the antibody coated microelectrode with buffer solution containing the

antigen of appropriate concentration followed by washing it with deionised water and air drying. Figure 6.15 shows the current-voltage response (I-V) of the electrode after antibody immobilization and after subsequent additions of different antigen concentrations. The I- V
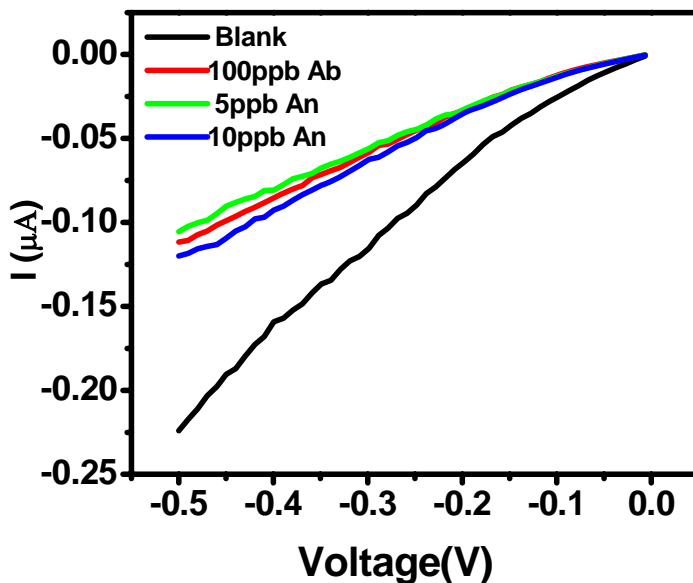
Figure 6.15 Voltammetric response of PANI coated IDA, after antibody immobilization and subsequent additions of antigen.

plots reflect changes in the conductivity of the microelectrode after antibody immobilization i.e. there is a significant decrease in the conductivity after antibody immobilization , but when antigen is added, there is no significant change in the conductivity. Hence it can be concluded that the film is not sensing the antigen. To further confirm the results, pulsed amperometric measurements were performed in situ.

Pulsed amperometric response of the electrode with time using five successive pulses of -0.1 V amplitude and 2 s dwell time was applied to assess the stability of the electrode and intra assay precision. Amount of antibody needed for the saturation of the PANI coated IDA can be determined using in situ addition of progesterone antibody in small aliquots. Figure

6.16 depicts the pulsed amperometric response of PANI coated microelectrode with the addition of progesterone antibody and Figure 6.17 shows current versus concentration of progesterone antibody graph. It has been observed that the conductivity of the
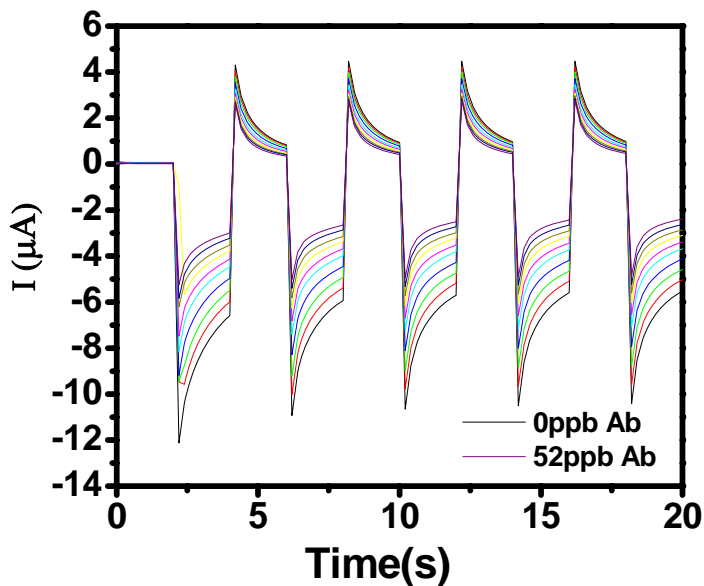
Figure 6.16 Chronoamperometric plot showing the change in conductivity with the addition of progesterone antibody (Ab) in small aliquots of around 5 ppb.
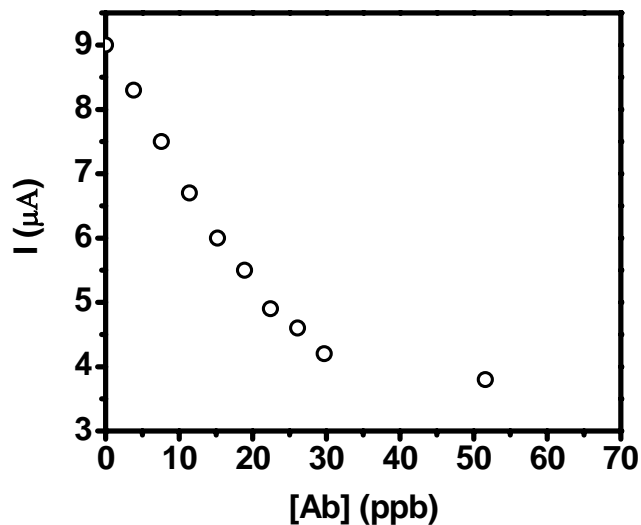
Figure 6.17 Current as a function of the concentration of added progesterone antibody (Ab).

165

immunoelectrode decreased with the addition of progesterone antibody which is in agreement with the voltammetric plots and reaches a saturation value at about 52 ppb of antibody. Hence around 60 ppb of antibody immobilized on PANI coated IDA is more than sufficient for further studies

Figure 6.18 depicts the pulsed amperometric response of PANI coated microelectrode with the addition of progesterone antigen after immobilizing with progesterone antibody and treating with BSA. It can be noted that there is no significant change in the response of PANI coated electrode with antigen addition.
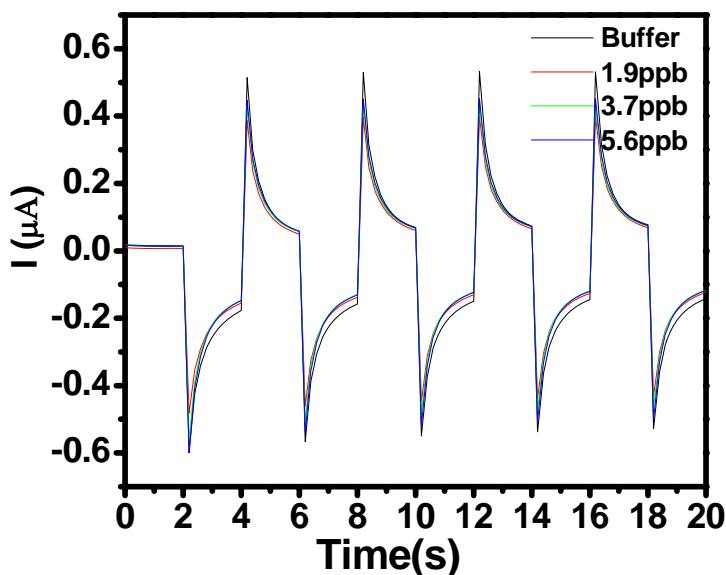
Figure 6.18 Pulsed amperometric response of PANI coated IDA with the addition of progesterone after the treatment of antibody and BSA.

The above studies suggest that the interaction of PANI film with progesterone antibody leads to a decrease in the conductivity of the polymer. However, with further addition of antigen, the change in conductivity is not significant. This could probably arise from the fact that the antibodies come directly in contact with the polymer film while the antigen interacts with the antibody. Thus, any effect of antigen interaction should transmit to

the polymer through the antibody. This could hinder the sensitivity of the polymer film towards antigen binding.

6.4 Conclusion

In summary, the use of self-assembled systems to prepare PANI nanoparticles is demonstrated using SDS micelles of varying dimensions. Surfactant stabilized PANI particles of different dimensions could be prepared by controlling the molar ratio of hydrotropic salt to anionic surfactant i.e. AHC to SDS ratio. Bare PANI particles, after removal of surfactant, show ability to bind with a model protein, BSA. The optical absorption spectra of PANI after binding with BSA indicate changes in the form of PANI and hence its conductivity. Thin films of the polymer on silver interdigitated electrodes show decrease in conductivity upon binding with progesterone antibody while no significant change in conductivity is observed upon further treatment with antigen.

CHAPTER 7

Summary and Conclusion

Chapter 7: Summary and Conclusion

The main objective of the present study is to get an insight in to the mechanism by which the structure of amphiphilic aggregates can be controlled by the structural properties of the constituent surfactant entities. Mixtures of cationic and anionic surfactants often display a rich variety of microstructures in aqueous solutions, governed by the molar ratio of the two components. This has stimulated extensive research interest among experimentalists as well as theoreticians. Oppositely charged cationic-anionic and surfactant-additive pairs are found to impart controllable and useful viscous and elastic properties in aqueous solutions without the addition of any particulates or polymers. This rheology control of aqueous solutions finds application in various fields such as drag reduction, cosmetics, water based paints, etc. Thus an understanding of the factors that govern the structure of aggregates is beneficial to prescribe a formulation having desired properties. Also such surfactant self assemblies have gained a lot of importance for the preparation of nanoparticles that can be used for various pharmaceutical applications. A brief summary and conclusions of the present investigation can be summarized as follows.

Natural fatty acid salts such as sodium laurate (SL), which is sparingly soluble in water at room temperature due to its high Kraft point, can undergo cooperative self-assembly in the presence of tetralkylammonium surfactants and make them attractive candidates for potential applications. Hence alkyltrimethylammonium salts like CTAB and TTAB have been used to decrease the Kraft point of sodium laurate by forming self-assembled microstructures when mixed together in various compositions. With the help of SANS, the axial and equatorial growth of CTAB/TTAB micelles induced by the addition of SL, have been investigated. It has been observed that both CTAB and TTAB micelles undergo elongation to form rod-like assemblies by the addition of SL. The axial growth is more pronounced in

Chapter 7: Summary and Conclusion

CTAB micelles as compared to TTAB. However, TTAB micelles undergo both equatorial swelling and elongation by the addition of SL. Difference in the growth behavior of TTAB and CTAB micelles can be attributed to the asymmetry in the chain lengths of cationic-anionic pairs. More the asymmetry, more favorable is the axial growth and as the asymmetry decreases, equatorial swelling occurs at the expense of axial growth. The effective interfacial area occupied by the cationic-anionic pair as well as the excess cationic surfactant in a mixture of CTAB and SL has been estimated. The effective head group area per molecule of dimer is sensitive to the dimer fraction in the aggregate, reflecting enhanced steric repulsion between ion-pairs. On the other hand, the equilibrium area per molecule of unimer is sensitive to the electrolyte concentration. From the ionic strength dependence of the equilibrium area per monomer, the contributions from steric and electrostatic effects can be separated. The variation in the equilibrium area of surfactant molecule with electrolyte concentration is consistent with the model predicted by Nagarajan. The effective area occupied by the surfactant molecule arises from a combination of electrostatic and steric contributions. In cationic-anionic mixtures, the formation of an ion-pair leads to decrease in the electrostatic contribution to the head group area due to charge neutralization. However, the steric contribution from the close packing of hydrocarbon tails increases with increasing fraction of ion-pairs. In the presence of the electrolyte, micellar growth is more pronounced due to its screening effect. Rheological studies confirm the formation of rod-like aggregates in CTAB/TTAB─SL mixture with an increase in the mole fraction of sodium laurate. When the axial ratio of the micelles is small, catanionic mixture behaves as a Newtonian fluid but at higher axial ratios, shear thinning behavior is observed. Dynamic rheology of the entangled micelles is similar to Maxwell fluids, which is the basic model for a viscoelastic fluid.

Chapter 7: Summary and Conclusion

Comparing the position of maxima in the zero shear viscosity versus concentration of C_nTAB-SL mixtures suggests that axial growth is more for surfactant with longer hydrocarbon chain, similar to the SANS results.

The rheological behavior of CTAB-NaOL mixed micelles over a wide concentration range exhibiting both linear and branched micelles has been studied using linear and dynamic rheology. According to Cates *et al.*, the rheological behavior of non ionic worm-like micelles follows simple scaling laws. The concentration dependence study of CTAB/NaOL mixed micelles at a fixed mole fraction of sodium oleate (x_{NaOL}=0.23), has shown that the exponents in the scaling laws change when the structural transition occurs from linear to branched micelles. The slope in the graph of plateau modulus vs volume fraction of the CTAB-NaOL micelles changes from 3.78 to 2.32 when the structural transition occurs from linear to branched micelles, different from Cates prediction. Also slope of the plot of entanglement length vs volume fraction of the micelles shows an abrupt change in the linear to branched micelle regime. This rheological behavior of the mixed micelles is analogous to the polymer melts, as previous studies report that a comparison of the rheological behavior of linear and branched polymers suggests that the hyperbranched polymers show a lower plateau modulus as compared to linear polymers. Also, a detailed phase behavior study of CTAB-NaOL mixed micellar system has shown various interesting phases including a birefringent phase and two vesicular phases at two different regions of the phase diagram. DLS, SANS, and Zeta potential has been used for characterizing the vesicular phases and found out they are stable vesicles of opposite surface charges.

Dilution induced structural and rheological changes in a mixed micelles composition comprising cationic surfactant, DTAB and hydrophobic salt SHNC, at different molar ratios

of SHNC to DTAB has been studied. DLS studies have indicated an increase in the size of the mixed micelles at a fixed molar ratio of SHNC to DTAB upon dilution and from the SANS studies, the increase in the size was attributed to the structural transition of the mixed micelles from spherical to rod-like micelles upon dilution. Finally cryo-TEM has confirmed the presence of rod-like micelles at low volume fraction of mixed micelles. This unusual behavior of surfactant-rich mixed micelles is explained in terms of desorption of surfactant from mixed micelles upon dilution, as the critical micelle concentration (CMC) for the surfactant DTAB is high due to its short hydrocarbon chain.

The use of self-assembled systems to prepare PANI nanoparticles is demonstrated using SDS micelles of varying dimensions, as AHC, the monomer for polymerization reaction is also a hydrotrope. Surfactant stabilized PANI nanoparticles of different dimensions could be prepared by controlling the molar ratio of hydrotropic salt to anionic surfactant i.e. AHC to SDS ratio. Bare PANI nanoparticles, after removal of surfactant, show ability to bind with a model protein, BSA, as shown by DLS results. The optical absorption spectra of PANI after binding with BSA indicate changes in the form of PANI. Thin films of the polymer on interdigitated electrodes show decrease in conductivity upon binding with progesterone antibody while no significant change in conductivity is observed upon further treatment with antigen.

REFERENCES

[1]   L. I. Osipow, *Surface Chemistry: Theory and Industrial Applications*, New York, Chapman and Hall 1962.

[2]   K. Shinoda, T. Nakagawa, B. Tamamushi and T. Isemura, *Colloidal surfactants*, New York, Academic 1963.

[3]   H. Wennerstrom and B. Lindman, *Phys. Rep.,* 1979**, 52**, 1.

[4]   B. Lindman, H. Wennerstrom, In *Topics in Current Chemistry*, Springer-Verlag, Berlin, 1980, **87**, 1.

[5]   D. J. Shaw, *Introduction to Colloid and Surface Chemistry*, London, Butterworths 1970.

[6]   J. Clint, *Surfactant Aggregation*, London, Blackie 1991.

[7]   Drew Myers, *Surfaces, Interfaces and Colloids: Principles and Applications*, New York, VCH 1991.

[8]   H. C. Hamaker, *Physica*, 1937, **4**, 1058.

[9]   E. J. W. Verwey and J. Th. G. Overbeek, *Theory of Stability of Lyophobic Colloids*, Elsevier, Amsterdam, 1948.

[10] J. B. Hayter and M. Zulauf, *Colloid. Polym. Sci.*, 1982, **260**, 1023.

[11] D.J. Mitchell, G. J. T. Tiddy, L. Waring, T. Bostock, M. P. McDonald, *J. Chem. Soc. Fraday. Trans.* I, 1983, **79**, 975.

[12]   J. H. Clint, In *Surfactant Aggregation*, Blackie and Son Ltd, Glasgow, 1992, 165.

[13] E. W. Kaler, A. K. Murthy, B. Rodriguez and J. A. N. Zasadzinski, *Science* 1989, **245**,1371.

[14] C. Tanford, In *The Hydrophobic Effect: Formation of Micelles and Biological Membranes*, 2nd Ed. John Wiley and Sons, New York, 1980, 3.

REFERENCES

[15] J. N. Israelachvili, D. J. Mitchell and B. W. Ninham, *J. Chem. Soc. Faraday, Trans*.I, 1970, **72**, 1525.

[16] W. Z. Helfrich, *Naturforsch.*, 1973, **28c**, 693.

[17] W. Helfrich, *J. Phys.(Paris),* 1985, **46**,1263.

[18] S. R. Raghavan, C. Fritz and E. W. Kaler, *Langmuir*, 2002, **18**, 3797.

[19] B. K. Mishra, S. D. Samant, P. Pradhan, S. B. Mishra and C. Manohar, *Langmuir,* 1993, **9**,894.

[20] H. Hoffmann, G. Platz, H. Rehage, W. Schorr and W. Ulbricht, *Ber. Bunsenges. Phys. Chem.*, 1981, **85**, 255.

[21] P. A. Hassan, Shilpa N. Sawant, Nitin C. Bagkar, and J. V. Yakhmi, *Langmuir*, 2004**, 20**, 4874.

[22] Y. Wan and D. Zhao, *Chem. Rev*., 2007, **107**, 2821.

[23] C. Ni, P. A. Hassan and E. W. Kaler, *Langmuir*, 2005, **21,** 3334.

[24] C. Pichot, *Curr Opin Colloid Interface Sci,*2004, **9,** 213.

[25] S. E. Kakabakos, E. Livaniou, G. P. Evangelatos and D. S. Ithakissios, *Clin. Chem.*, 1990, **36,** 492.

[26] R. Pecora, In *"The Scattering of Light and Other Electromagnetic Radiation",*Academic Press, New York, 1969, 482.

[27] J. C. Brown, P. N. Pusey and R. Dietz, *J. Chem. Phys.*, 1975, **62**, 1136.

[28] S. W. Lovesey, *Theory of Neutron Scattering from Condensed Matter*, Oxford University Press, Oxford, 1984.

[29] G. L. Squires, *Thermal Neutron Scattering*, Cambridge University Press, Cambridge, 1978.

REFERENCES

[30] K. Skold and D. L. Price, *Methods of Experimantal Physics, Neutron Scattering*, Academic Press, London, 1986, **23**.

[31] L. A. Feigin and D. I. Svergun, *Structure Analysis by Small-Angle Neutron X-ray and Neutron Scattering*, Plenum Press, New York, 1987.

[32] P. Linder and T. Zemb, *Neutron, X-Ray and Light Scattering*, North Holland, Amsterdam, 1991.

[33] S. H. Chen and T. L. Lin, in *Methods of Experimental Physics*, Academic Press, New York, 1987.

[34] A. Guinier and G. Fournet, *Small-Angle Scattering of X-Rays*, Wiley Interscience, New York, 1955.

[35] O. Glatter and O. Kratky, *Small-Angle X-Ray Scattering*, Academic Press, London, 1982.

[36] G. Porod, Z. Kolloid, 1951, **124**, 83.

[37] P. A. Egelstaff, *An Introduction to Liquid State Physics*, Academic Press, London, 1967.

[38] J. P. Hansen and I. R. Mc Donald, *Theory of Simple Liquids*, Academic Press, London, 1986.

[39] H. A. Barnes, J. F. Hutton, K. Walters, In "*An Introduction to rheology*", Elsevier, Amsterdam, 1989.

[40] J. D. Ferry, In"*Viscoelastic Properties of Polymers*", John Wiley, New York, 1980.

[41] M. Li, H. Schnablegger, S. Mann, *Nature*, 1999, **402**, 393.

[42] K. K. Rohatgi-Mukerjee, *Fundamentals of Photochemistry*, Wiley, New Delhi, 1978.

[43] R. A. Alberty, *Physical Chemistry*, Wiley Eastern, New Delhi, 1991, 462.

[44] J. Bessett, R. C. Denney, G. H. Jeffery and J. Mendham, *Vogel's Textbook of Quantative Inorganic Analysis*, Bungay, ELBS, 1978, 696.

REFERENCES

[45] A. J. Bard and L. R. Faulkner, In *Electrochemical Methods: Fundamentals and Applications*, Wiley India, New Delhi, 2004.

[46] E. J. W. Verway, J. Th. G. Overbeek, *Theory of the Stability of Lyophobic Colloids*, Elsevier, Amsterdam, 1948.

[47] R. J. Hunter, *Zeta Potential in Colloid Science:Principles and Applications*, Academic Press, UK, 1988.

[48] D. J. Shaw, *Introduction to Colloid and Surface Chemistry*, Butterworth Heinemann, UK, 1992.

[49] D. Carriere, L. Belloni, B. Deme, M. Dubois, C. Vautrin, A. Meister and T. Zemb, *Soft Matter*, 2009, **5**, 4983.

[50] X. Cui, Y. Jiang, C. Yang, X. Lu, H. Chen, S. Mao, M. Liu, H. Yuan, P. Luo and Y. Du, *J. Phys. Chem. B*, 2010, **114**, 7808.

[51] P. A. Hassan, T. K. Hodgdon, M. Sagasaki, G. F. Popouski and E. W. Kaler*, C. R. Chimie*, 2009, **12**, 18.

[52] J. N. Israelachvili, D. J. Mitchell and B. W. Ninham, *J Chem Soc Faraday Trans* II, 1976, **72**, 1525.

[53] J. D. Mitchell and B. W. Ninham, *J Chem Soc Faraday Trans* II, 1981, **77**, 601.

[54] E. W. Kaler, K. L. Herrington, A. K. Murthy and J. A. N. Zasadzinski, *J. Phys. Chem.,* 1992, **96**, 6698.

[55] M. Bergstrm and J. S. Pedersen, *Langmuir*, 1998, **14**, 3754.

[56] R. D. Koehler, S. R. Raghavan and E. W. Kaler, *J. Phys. Chem. B*, 2000, **104**, 11035.

[57] H. T. Jung, B. Coldren, J. A. Zasadzinski, D. J. Iampietro and E. W. Kaler, *Proc. Natl. Acad. Sci.*, U.S.A., 2001, **98**, 1353.

[58] H. Fan, Y. Yan, Z. Li, L. Xu, B. Zhang and J. Huang, *J. Colloid Interface Sci.,* 2010, **348**, 491.

[59] U. Olsson, J. Borjesson, R. Angelico, A. Ceglie and G. Palazzo, *Soft Matter*, 2010, **6**, 1769.

[60] V. Croce, T. Cosgrove, C. A. Dreiss, G. Maitland, T. Hughes and G. Karlsson, *Langmuir*, 2004, **20**, 7984.

[61] S. R. Raghavan, *Langmuir*, 2001, **17**, 300.

[62] E. Cappelaere and R. Cressely, *Colloid Polym. Sci.,* 1998, **276**, 1050.

[63] M. E. Cates and S. J. Candau, *J. Phys. Condens. Matter*, 1990, **2**, 6869.

[64] M. E. Cates, *Macromolecules*, 1987, **20**, 2289.

[65] C. A. Dreiss, *Soft Matter*, 2007, **3**, 956.

[66] S. Ezrahi, E. Tuval and A. Aserin, *Adv. Colloid Interface Sci.*, 2006, **128-130**, 77.

[67] Z. Yuan, W. Lu, W. Liu and J. Hao, *Soft Matter*, 2008, **4**, 1639.

[68] B. Lin, A. V. McCormick, H. T. Davis and R. Strey, *J. Colloid Interface Sci.*, 2005, **291**, 543.

[69] N. Dew, T. Bramer and K. Edsman, *J. Colloid Interface Sci.*, 2008, **323**, 386.

[70] S. Lieberman, G. M. Enig and G. H. Preuss, *Alt. Compl. Ther.*, 2006, **12**, 310.

[71] P. Rayan, D. Stenzel and P. A. McDonnell, *Parasitol. Res.*, 2005, **97**, 191.

[72] J. Eastoe, P. Rogueda, D. Shariatmadari and R. Heenan, *Colloids Surf. A*, 1996, **117**, 215.

[73] R. Nagarajan, *Langmuir*, 2002, **18**, 31.

[74] P. S. Russo, F. E. Karasz, K. H. Langley, *J. Chem. Phys.*, **1984**,*80*, 5312.

[75] A. Isihara, *J. Chem. Phys.*, 1950, **18**, 1446.

[76] J. M. Peterson, *J. Chem. Phys.*, 1964, **40**, 2680.

REFERENCES

[77] D. Lehner, H. Lindner, O. Glatter, *Langmuir,* 2000, **16**, 1689.

[78] M. M. Tirado,C. L. Martinez, J. G. de La Torre, *J. Chem. Phys.,* 1984, **81**, 2047.

[79] A. M. Smith, M. C. Holmes, A. Pitt, W. Harrison, G. J. T. Tiddy, *Langmuir,* 1995, **11**, 4202.

[80] O. Regev, M. S. Leaver, R. Zhou, S. Puntambekar, *Langmuir*, 2001, **17**, 5141.

[81] Z. J. Yu, R. Neuman, *Langmuir*, 1994, **10**, 377.

[82] S. Kumar, V. K. Aswal, D. Sharma, P. S. Goyal, Kabir-ud-Din *J. Chem. Soc., Faraday Trans.*, 1998, **94**, 761.

[83] S. Kumar, D. Sharma, Kabir-ud-Din, *Langmuir*, 2000, **16**, 6821.

[84] S. Kumar, V. K. Aswal, A. Z. Naqvi, P. S. Goyal, Kabir-ud-Din, *Langmuir*, 2001, **17**, 2549.

[85] S. Kumar, D. Sharma, A. Z. Khan, Kabir-ud-Din, *Langmuir*, 2002, **18**, 4205.

[86] M. Benrraou, B. L. Bales, R. Zana, *J. Phys. Chem. B*, 2004, **108**, 18195.

[87] W. Y. Wen, S. Saito, *J. Phys. Chem.*, 1964, **68**, 2639.

[88] M. J. Blandamer, M. J. Foster, N. J. Hidden, M. C. R. Symons, *Trans. Faraday Soc.*, 1968, **64**, 3247.

[89] H. E. Wirth, A. LoSurdo, *J. Phys. Chem.*, 1968, **72**, 751.

[90] H. E. Wirth, A. LoSurdo, *J. Phys. Chem.*, 1972, **76**, 130.

[91] K. Tamaki, *Bull. Chem. Soc. Jpn.*, 1974, **47**, 2764.

[92] V. K. Aswal and P. S. Goyal, *Physica B*, 1998, **245**, 73.

[93] J. B. Hayter and P. Penfold, *Colloid Polym. Sci.*, 1983, **261**, 1022.

[94] W. R. Chen, P. D. Butler and L. J. Magid, *Langmuir*, 2006, **22**, 6539.

[95] M. Schmidt, G. Paradossi and W. Burchard, *Makromol. Chem., Rapid Commun.*, 1985, **6**, 767.

[96] M. Bergstrm and J. S. Pedersen, *Langmuir*, 1999, **15**, 2250.

[97] H. Yin, M. Mao, J. Huang and H. Fu, *Langmuir*, 2002, **18**, 9198.

[98] P. A. Hassan, S. R. Raghavan, E. W. Kaler, *Langmuir*, 2002, **18**, 2543.

[99] P. A. Hassan, J. V. Yakhmi, *Langmuir*, 2000, **16**, 7187.

[100] F. Lequeux, *Europhys. Lett.*, 1992, **19**, 675.

[101] R. Zana, E. W. Kaler, *Giant micelles: Properties and applications*; **140**, CRC press: New York, 2007**.**

[102] N. Vlachy, C. Merle, D. Tourand, J. Schmidt, Y. Talmon, J. Heilmann, W. Kunz, *Langmuir*, 2008, **24**, 9983.

[103] T. Bramer, N. Dew, K. Edsman, *Journal of Pharmaceutical Science*, 2006, **95**, 769.

[104] H. Yin, M. Mao, J. Huang, H. Fu, *Langmuir*, 2002, **18**, 9198.

[105] W. Jiang, J. Hao, *Langmuir*, 2008, **24**, 3150.

[106] H. Wennerstrom, B. Lindman, *Top. Curr. Chem.*, 1980, **87**, 1.

[107] V. Degiorgio, M. Corti, *Physics of Amphiphiles: Micelles, Vesicles and Microemulsion*, North-Holland, Amsterdam, 1985.

[108] S. H. Chen, *Annu. Rev. Phys. Chem.*, 1986, **37**, 351.

[109] D. I. Svergun, *Mathematical methods in small-angle scattering data analysis. J. Appl. Cryst.*, 1991, **24**, 485.

[110] N. Vlachy, M. Drechsler, D. Tourand and W. Kunz, *C. R. Chimie*, 2009, **12**, 30.

[111] S. Prevost and M. Gradzielski, *J. Colloid Interface Sci.*, 2009, **337**, 472.

REFERENCES

[112] S. Amin, T. W. Kermis, R. M. V. Zanten, S. J. Dees, J. H. V. Zanten, *Langmuir*, 2001, **17**, 8055.

[113] T. C. B. McLeish, *Advances in physics*, 2002, **51**, 1379.

[114] B. A. Schubert, E. W. Kaler, N. J. Wagner, *Langmuir*, 2003, **19**, 4079.

[115] A. Khatory, F. Lequeux, F. Kern, S. J. Candau, *Langmuir*, 1993, **9**, 1456.

[116] S. J. Candau, A. Khatory, F. Lequeux, F. Kern, *J. Phys. IV*, 1993, **3**, 197.

[117] C. Oelschlaeger, P. Suwita, N. Willenbacher, *Langmuir*, 2010, **26(10)**, 7045.

[118] R. Graneck, M. E. Cates, *J. Chem. Phys.*, 1992, **96**, 4758.

[119] M. S. Turner, M. E. Cates, *J. Phys. II France*, 1992, **2**, 503.

[120] H. Rehage, H. Hoffmann, *J. Phys. Chem.*, 1988, **92**, 4712.

[121] T. Shikata, H. Hirata, T. Kataka, *Langmuir* 1989, **5**, 398.

[122] T. M. Clausen, P. K. Vinson, J. R. Minter, H. T. Davis, Y. Talmon, W. G. Miller, *J. Phys. Chem.*, 1992, **96**, 474.

[123] J. Appell, G. Porte, A. Khatory, F. Kern, S. J. Candau, *J. Phys. II France*, 1992, **2**, 1045.

[124] S. Hayashi, S. Ikeda, *J. Phys. Chem.*, 1980, **84**, 744.

[125] F. A. L. Anet, *J. Am. Chem. Soc.*, 1986, **108**, 7102.

[126] J. F. A. Soltero, J. E. Puig, O. Manero, P. C. Schulz, *Langmuir*, 1995, **11**, 3337.

[127] E. W. Kaler, K. L. Herrington, A. K. Murthy, J. A. Zasadzinski, S. Chiruvolu, *J. Phys. Chem.*, 1993, **97**, 13792.

[128] L. L. Brasher, K. L. Herrington, E. W. Kaler, *Langmuir*, 1995, **11**, 4267.

[129] M. T. Yatcilla, K. L. Herrington, L. L. Brasher, E. W. Kaler, J. A. Zasadzinski, *J. Phys. Chem.*, 1996, **100**, 5874.

REFERENCES

[130] P. A. Hassan, K. Bhattacharya, S. K. Kulshreshtha, and S. R. Raghavan, *J. Phys. Chem.*, 2005, **109**, 8744.

[131] H. Cui, T. K. Hodgdon, E. W. Kaler, L. Abezgauz, D. Danino, M. Lubovsky, Y. Talmon, D. Pochan, 2007, **3**, 945.

[132] M. E. Cates, M. S. Turner, *Europhys. Lett.*, 1990, **11(7)**, 681.

[133] P. A. Hassan, S. J. Candau, F. Kern and C. Manohar, *Langmuir*, 1998, **14**, 6025.

[134] J. F. Berret, J. Appell, G. Porte, *Langmuir*, 1993, **9**, 2851.

[135] M. Doi, S. F. Edwards, *The theory of polymer dynamics;* Clarendon Press: Oxford, 1986.

[136] P. G. De Gennes, In *"Scaling Concepts in Polymer Physics"* Cornell University Press Ithaca, New York 1979.

[137] Des Cloizeaux, *J. Phys. (Paris)*, 1975, **36**, 381.

[138] J. Park, K. An, Y. Hwang, J. G. Park, H. J. Noh, J. K. Kim, J. H. Park, N. M. Hwang, T. Hyeon, *Nat. Mater.*, 2004, **3**, 891.

[139] V. Croce, T. Cosgrove, C. Flood, C. A. Dreiss, G. Karlsson, *Langmuir*, 2005, **21**, 7646.

[140] N. El-Kadi, F. Martins, D. Clausse, P. C. Schulz, *Colloid Polym. Sci.*, 2003, **281**, 353.

[141] M. Chellamuthu, J. P. Rothstein, *J. Rheol.*, 2008, **52(3)**, 865.

[142] S. Unal, I. Yilgor, E. Yilgor, J. P. Sheth, G. L. Wilkes, T. E. Long, *Macromolecules*, 2004, **37**, 7081.

[143] G. C. Kalur, S. R. Raghavan, *J. Phys. Chem. B*, 2005, **109**, 8599.

[144] L. J. Magid, Z. Han, Z. Li, *J. Phys. Chem. B*, 2000, **104**, 6717.

[145] E. W. Kaler, A. K. Murthy, J. A. N. Zasadzinski, *Science*, 1989, **245**, 1371.

[146] O. Regev, A. Khan, *J. Colloid Interface Sci.*, 1996, **182,** 95.

[147] O. S. Derman, K.L. Herrington, E.W. Kaler, D.D. Miller, 1997, 13, 5531.

REFERENCES

[148] E.F. Marques, O. Regev, A. Khan, M.G. Miguel, B. Lindman, *J. Phys. Chem. B*, 1998, **102**, 6746.

[149] E.F.Marques, O. Regev, A. Khan, M.G. Miguel, B. Lindman, *J. Phys. Chem. B*, 1999, **103,** 8353.

[150] M. Bergstrom, J.S. Pedersen, P. Schurtenberger, S.U. Egelhaaf, *J. Phys. Chem.*, 1999, **103,** 9888.

[151] H. Sakai, A. Matsumura, S. Yokoyama, T. Saji, M. Abe, *J. Phys. Chem. B*, 1999, **103,** 10737.

[152] E.W. Kaler, K.L. Herrington, D.J. Iampietro, B.A. Coldren, H. T. Jung, J.A. Zasadzinski, *Mixed Surfactant Systems,* **124**, Marcel Dekker, New York, 2005, 289.

[153] C. Letizia, P. Andreozzi, A. Scipioni, C. La Mesa, A. Bonincontro, E. Spigone, *J. Phys. Chem. B*, 2007, **111**, 898.

[154] A. Fischer, M. Hebrant, C. Tondre, *J. Colloid Interface Sci.*, 2002, **248**, 163.

[155] E.J. Danoff, X. Wang, S. H. Tung, N. A. Sinkov, A. M. Kemme, S.R. Raghavan, D.S. English, *Langmuir*, 2007, **23**, 8965.

[156] H. P. Hentze, S.R. Raghavan, C.A. McKelvey, E.W. Kaler, *Langmuir*, 2003, **19,** 1069.

[157] D.H.W. Hubert, M. Jung, L.A. German, *Adv. Mater.*, 2000, **12**, 1291.

[158] D. Lootens, C. Vautrin, H. Van Damme, T. Zemb, *J. Mater. Chem.*, 2003, **13,** 2072.

[159] C. Caillet, M. Hebrant, C. Tondre, *Langmuir*, 2000, **16**, 9099.

[160] A. Fischer, M. Hebrant, C. Tondre, *J. Colloid Interface Sci.*, 2002, **248**, 163.

[161] E. J. Danoff, X. Wang, S. H. Tung, N. A. Sinkov, A. M. Kemme, S. R. Raghavan, D. S. English, *Langmuir*, 2007, **23**, 8965.

[162] R. S. Dias, B. Lindman, M. G. Miguel, *J. Phys. Chem. B*, 2002, **106**, 12600.

[163] N. Berclaz, M. M_ller, P. Walde, P. L. Luisi, *J. Phys. Chem. B*, 2001, **105**, 1056

[164] N. Berclaz, E. Blçchliger, M. M_ller, P. L. Luisi, *J. Phys. Chem. B*, 2001, **105**, 1065.

[165] A. Shome, T. Kar, and P. K. Das, *ChemPhysChem*, 2011, **12**, 369.

[166] W. Z. Helfrich, *Naturforsch.*, 1973, **28 C**, 693.

[167] R. Lipowsky, *Nature*, 1991, **349**, 475.

[168] S. A. Safran, P. Pincus, A. Andelman, F. C. Mackintosh, *Phys.Rev.*, 1991, **43**, 1071.

[169] B. D. Simons, M. E. Cates, *J. Phys. II France*, 1992, 1439.

[170] E. Sackman, *FEBS Lett.*, 1994, **346**, 3.

[171] J. N. Israelachvili, D. J. Mitchell, B. W. Ninham, *J. Chem. Soc.,Faraday Trans. 2*, 1976, **72**, 1525.

[172] J. N. Israelachvili, *Intermolecular and Surface Forces*, Academic Press, San Diego, CA, 1992.

[173] A. I. Rusanov, *Colloids Surf. A*, 1993, **76**, 7.

[174] P. K. Yuet, D. Blankschtein, *Langmuir*, 1996, **12**, 3802.

[175] B. Putlitz, K. Landfester, S. Forster and M. Antonietti, *Langmuir*, 2000, **16**, 7.

[176] L. L. Brasher and E. W. Kaler, *Langmuir*, 1996, **12***, 6270

[177] M. B. Dowling, J. Lee and S. R. Raghavan, *Langmuir*, 2009, **25(15)**, 8519.

[178] J.L. Zakin, H.W. Bewersdorff, *Rev. Chem. Eng.*, 1998, **14,** 253.

[179] G.C. Maitland, *Curr. Opin. Colloid Interface Sci.*, 2000, **5,** 301.

[180] J. Yang, *Curr. Opin. Colloid Interface Sci.*, 2002, **7**, 276.

[181] Y.J. Song, R.M. Garcia, R.M. Dorin, H.R. Wang, Y. Qiu, E.N. Coker, W.A. Steen, J.E. Miller, J.A. Shelnutt, *Nano Lett.*, 2007, **7**, 3650.

[182] H. Rehage, H. Hoffmann, *Mol. Phys.*, 1991, **74,** 933.

REFERENCES

[183] L.J. Magid, *J. Phys. Chem.*, 1998, **102**, 4064.

[184] G. Porte, J. Appell, Y. Poggi, *J. Phys. Chem.*, 1980, **84**, 3105.

[185] H. Rahege, H. Hoffmann, I. Wunderlich, *Ber. Bunsen-Ges. Phys. Chem.*, 1986, **90**, 1071.

[186] C. Manohar, U. R. K. Rao, B. S. Valaulikar, R. M. Iyer, *J. Chem. Soc., Chem. Commun.*, 1986, 379.

[187] J. Ulmius, H. Wennerstrom, L. B. Johannson, G. Lindblom, S. Gravsholt, *J. Phys. Chem.*, 1979, **83**, 2232.

[188] H. Hoffmann, U. Kramer, H. Thurn, *J. Phys. Chem.*, 1990, **94**, 2027.

[189] H. Hoffmann, J. Kalus, H. Thurn, K. Ibel, *Ber. Bunsen-Ges. Phys. Chem.*, 1983, **87**, 1120.

[190] X. I. Wu, C. Yeung, M. W. Kim, J. S. Huang, D. Ou-Yang, *Phys. Rev. Lett.*, 1992, **68**, 1426.

[191] T. Wolff, C. S. Emming, G. Von Bunau, K. Zierold, *Colloid Polym. Sci.*, 1992, **270**, 822.

[192] D. Danino, Y. Talmon, H. Levy, G. Beinert, R. Zana, *Science*, 1995, **269**, 1420.

[193] R. Oda, Janaky Narayanan, P. A. Hassan, C. Manohar, R. A. Salkar, F. Kern and S. J. Candau, *Langmuir*, 1998**, 14**, 4364.

[194] L. Li, Y. Yang, J. Dong, X. Li, *J. Colloid Interface Sci.,* 2010, **343**, 504.

[195] Gunjan Verma, V.K. Aswal, Gerhard Fritz-Popovski , C.P. Shah, Manmohan Kumar, P.A. Hassan, *J. Colloid Interface Sci.*, 2011, **359**, 163.

[196] Y. Chen, United States Patent 6617293.

[197] M. Scherlund, K. Welin-Berger, A. Brodin, M. Malmstenb, *Eur. J. Pharm. Sci.*, 2001, **14**, 53.

[198] P. A. Hassan and J. V. Yakhmi, *Langmuir*, 2000, **16**, 18.

REFERENCES

[199] S.U. Egelhaaf, P. Schurtenberger, *Phys. Rev. Lett.*, 1999, **82**, 2804.

[200] M.A. Long, E.W. Kaler, S.P. Lee, *Biophys. J.*, 1994, **67**, 1733.

[201] B.F.B. Silva, E.F. Marques, U. Olsson, *Langmuir*, 2008, **24**, 10746.

[202] Z. Hu, A.M. Jonas, S.K. Varshney, J.F. Gohy, *J. Am. Chem. Soc.*, 2005, **127**, 6527.

[203] N. Oyama, T. Tatsuma, T. Sato, T. Sotomura, *Nature*, 1995, **373**, 598.

[204] S. Groth, W. Graupner, *Synth. Met.*, 1993, **55**, 3623.

[205] B. Scrosati, *Prog. Solid State Chem.*, 1988, **18**, 1.

[206] E. Genies, P. Hany, C. Santier, *J. Appl. Electrochem.*, 1988, **18**, 751.

[207] A. Boyle, E. Genies, M. Lapkowski, *Synth. Met.*, 1989, **28**, C769.

[208] U. Lange, N. V. Roznyatovskaya, V. M. Mirsky, Analytica Chimica Acta, 2008, **614**, 1.

[209] Y. Ikarijiama, W. R. Heineman, *Anal. Chem.*, 1986, **56**, 1803.

[210] M. E. G. Lyons, C. H. Lyons, C. Fitzgerald, P. N. Bartlett, *J. Electroanal. Chem.*, 1994, **365**, 29.

[211] P. M. S. Monk, R. J. Mortimer, D. R. Rosseinsky, *Electrochromism: Fundamentals and Applications*, VCH, Wienheim, 1995, Chap. 6.

[212] A. Malinauskas, R. Holze, *Synth. Met.*, 1998, **97**, 31.

[213] M. C. Bernard, A. Hugot Le Goff, *J. Electrochem. Soc.*, 1994, **141**, 2682.

[214] M. S. Wrighton, *Science*, 1986, **231**, 32.

[215] A. Heeger, *J. Curr. Appl. Phys.*, 2001, **1**, 247.

[216] S. Tawde, D. Mukesh, J. V. Yakhmi, *Synth. Met.*, 2002, **125**, 401.

[217] C. L. Gettinger, A. J. Heeger, D. J. Pine, Y. Cao, *Synth. Met.*, 1995, **74**, 81.

[218] Y. Cao, P. Smith, A. Heeger, *J. Synth. Met.*, 1992, **48**, 91.

[219] Y. Cao, G. Treacy, P. Smith, A. Heeger, *J. Appl. Phys. lett.*, 1992, **60**, 2711.

REFERENCES

[220] B. Vincent, J. Waterson, *Chem. Commun.*, 1990, 683.

[221] J. Stejskal, P. Kratochvil, M. Helmstedt, *Langmuir*, 1996, **12**, 3389.

[222] S. P. Armes, M. Aldissi, S. F. Agnew, S. Gottesfeld, *Langmuir*, 1990, **6**, 1745.

[223] P. Banerjee, S. N. Bhattacharyya, B. M. Mandal, *Langmuir*, 1995, **11**, 2414.

[224] D. Chattopadhyay, S. Banerjee, D. Chakravorty, B. M. Mandal, *Langmuir*, 1998, **14**, 1544.

[225] D. Chattopadhyay, B. M. Mandal, *Langmuir*, 1996, **12**, 1585.

[226] N. Gospodinova, P. Mokreva, L. Terlemezyan, *Chem.Commun.*, 1992, 923.

[227] J. Stejskal, M. Spirkova, A. Riede, M. Helmstedt, P. Mokreva, J. Prokes, *Polymer*, 1999, **40**, 2487.

[228] L. M. Gan, C. H. Chew, S. O. Hardy, L. Ma, *Polym. Bull.*, 1993, **31**, 347.

[229] S. T. Selvan, A. Mani, K. Athinarayanasamy, K. L. Phani, S. Pitchumani, *Mater. Res. Bull.*, 1995, **30**, 699.

[230] E. Marie, R. Rothe, M. Antonietti, K. Landfester, *Macromolecules*, 2003, **36**, 3967.

[231] Z. M. Zhang, Z. X. Wei, M. X. Wan, *Macromolecules*, 2002, **35**, 5937.

[232] P. S. Rao, D. N. Sathyanarayana, S. Palaniappan, *Macromolecules*, 2002, **35**, 4988.

[233] D. Kim, J. Choi, J. Y. Kim, Y. K. Han, D. Sohn, *Macromolecules*, 2002, **35**, 5314.

[234] N. Kuramoto, E. M. Genies, *Synth. Met.*, 1995, **68**, 191.

[235] N. Kuramoto, A. Tomita, *Polymer*, 1997, **38**, 3055.

[236] N. Gospodinova, P. Mokreva, T. Tsanov, L. Terlemezyan, *Polymer*, 1997, **38**, 743.

[237] B. J. Kim, S. G. Oh, M. G. Han, S. S. Im, *Langmuir*, 2000, **16**, 5841.

[238] B. J. Kim, S. G. Oh, M. G. Han, S. S. Im, *Synth. Met.*, 2001, **122**, 297.

[239] M. G. Han, K. C. Seok, S. G. Oh, S. S. Im, *Synth. Met.*, 2002, **126**, 53.

REFERENCES

[240] A. Sehgal, T. A. P. Seery, *Macromolecules*, 1999, **32**, 7807.

[241] M. Gerard, A. Chaubey, B. D. Malhotra, *Biosensors & Bioelectronics*, 2002, **17**, 345.

[242] M. Solé, C. Porte, D. Barceló, *Trends Anal. chem.*, 2001, **20 (9)**, 518.

[243] A. Kiriy, G. Gorodyska, S. Minko, W. Jaeger, P. Stepanek, M. Stamm, *J. Am. Chem. Soc.*, 2002, **124**, 13454.

[244] E. Marie, R. Rothe, M. Antonietti, K. Landfester, *Macromolecules*, 2003, **36**, 3967.

[245] D. W. Brann, *Progesterone: the forgotten hormone? Perspect. Biol. Med.*, 1993, **36**, 642.

[246] J. Tschmelak, N. Kappel, G. Gauglitz, *Anal Bioanal Chem*, 2005, 382, 1895.

[247] S. C. T. Susan, X. Bei, J. W. Michael, *Anal. Chem.*, 2006, **78**, 6628.

[248] T. Karir, P. A. Hassan, S. K. Kulshreshtha, G. Samuel, N. Sivaprasad, M. Venkatesh, *Anal. Chem.*, 2006, **78**, 3577.

Publications

List of Publications

1. Viscoelastic Fluids Originated from Enhanced Solubility of Sodium Laurate in Cetyl Trimethyl Ammonium Bromide Micelles through Cooperative Self-Assembly

    Prasuna Koshy, Gunjan Verma, V. K. Aswal, Meera Venkatesh and P. A. Hassan
    J. Phys. Chem. B, 2010, **114**, 10462-10470.

2. Swelling and Elongation of Tetradecyltrimethylammonium Bromide Micelles Induced by Anionic Sodium Laurate

    Prasuna Koshy, V. K. Aswal, Meera Venkatesh and P. A. Hassan
    Soft Matter, 2011, **7**, 4778-4786.

3. Unusual Scaling in the Rheology of Branched Wormlike Micelles Formed by Cetyltrimethylammonium Bromide and Sodium Oleate

    Prasuna Koshy, V. K. Aswal, Meera Venkatesh and P. A. Hassan
    J. Phys. Chem. B, 2011, **115**, 10817-10825.

4. Dilution Induced Structural Transition in DTAB/SHNC Mixed Surfactant System

    Prasuna Koshy, V. K. Aswal, Janaky Narayanan, Jayesh Bellare, Meera Venkatesh and P. A. Hassan
    (Manuscript under preparation)

5. Vesicle Formation in Mixtures of CTAB and Sodium Oleate: Phase behavior and scattering studies.

    Prasuna Koshy, V. K. Aswal, Meera Venkatesh and P. A. Hassan
    (Manuscript under preparation)